Simulation Studies for the Collimation System in the TESLA Beam Delivery System

A thesis submitted to the University of Manchester for the degree of Doctor of Philosophy in the Faculty of Science and Engineering

2004

Adriana Bungau

THE UNIVERSITY of MANCHESTER

Particle Physics Group

Department of Physics and Astronomy

Contents

List of Figures

List of Tables

Abstract

Beam collimation and machine protection are problems faced by all the linear collider designs. Large amplitude particles can generate backgrounds in the detector if they impact at small apertures in the elements close to the detector or generate synchrotron radiation in the quadrupoles which impacts further downstream. Obviously, this would be one of the worst scenarios for the particle physics experiments. Worldwide linear collider working groups are investigating several collimation concepts but no completely satisfactory solution has been found so far.

The effect on a beam of offsets in position, angle and energy on the beam delivery system components is presented here. The particle deposition on the spoilers is analysed and the temperature rise is calculated. The collimation depth in the absence of scattering is compared with the case when the scattering is included in the simulation code. A possible position of the absorbers is determined.

Declaration

No portion of the work referred to in this thesis has been submitted in support of an application for another degree or qualification of this or any other university or other institute of learning.

The Author

The author was educated at the University of Bucharest, Romania, before joining the Department of Physics and Astronomy at the University of Manchester. The work presented here was undertaken at Manchester and Daresbury Laboratory.

To the memory of my father

Acknowledgements

During my PhD, I had the opportunity to work with many people and I wish to take this opportunity to thank all those who explained me the basic ideas in both particle physics and accelerator physics and guided me. I wished I could mention them individually and apologize for not doing so.

My thanks goes firstly to my supervisor *Prof Roger Barlow* for his help, encouragement and advice over the last three years. Having learned greatly from these interactions, I wish to thank him for he answered all my questions and pointed me in the right direction. For his help and ability in dealing with all administrative and financial problems that a PhD student can encounter and also for his friendliness and humor, I would like to thank my adviser *Dr Fred Loebinger*. My sincere thanks goes also to the system administrator *Stuart Wild* for dealing promptly and efficiently with all my computer related problems.

My thanks goes also to *Dr Hywel Owen* from Daresbury Laboratory for providing guidance on accelerator physics aspects of the work and for valuable opinion throughout the production of this thesis. Thanks are also due to *Dr Nick Walker* from DESY for his help with the simulation code and for several useful discussions.

I also want to acknowledge USPAS school for providing a high level training in accelerator physics, fundings and a wonderful atmosphere were I made many friends.

My sincere thanks goes to mum, Florin, my brother Sebastian and my parents-in-law for help and support. In particular, my husband *Cristian* deserves a special mention for many clarifying discussions we had on physics issues and also for his patience and his tremendous moral support.

Finally, I wish to devote my last words to my dad, whose wit and wisdom I've

always treasured and thanks to whom I became a physicist. Thanks dad, I will always remember you!

Chapter 1

The Impact of a Linear Collider on Particle Physics

The last century has been an amazing period of experimental discoveries and surprises and it is stunning how our understanding of physics has changed in the last hundred years. The great insights were of course Quantum Mechanics and Relativity Theory which were later fused in Quantum Field Theory. Based on the Quantum Field Theory framework, theoretical physicists have been able to construct the Standard Model of particle physics, which puts under one roof most of what we know about fundamental physics. At the present time, all experimental observations in particle physics are consistent with this model [1]. The Standard Model asserts that the matter in the universe is made up of two types of elementary particles, quarks and leptons, both fermions, interacting through fields of which they are the sources. The properties of these particles are presented in Tables 1.1 and 1.2. The particles associated with the interaction fields are bosons. The types of interaction that have been distinguished are: electromagnetic interactions mediated by *photons*, strong interactions mediated by *gluons*, weak interactions mediated by W^+, W^-, and Z^0. On the scales of particle physics, gravitational forces are insignificant and the Standard Model excludes from consideration the gravitational field. Undoubtedly, the Standard Model is an impressive consistent theory which answers many questions: what are the ultimate constituents of matter, how are they categorised, how do

leptons	mass (MeV/c^2)	mean life (s)	electric charge
e^-	0.5110	∞	-e
ν_e	$< 15 \cdot 10^{-6}$	∞ ?	0
μ^-	105.658	$2.197 \cdot 10^{-6}$	-e
ν_μ	< 0.17	∞ ?	0
τ^-	1777	$(291.0 \pm 1.5) \cdot 10^{-15}$	-e
ν_τ	< 24	∞ ?	0

Table 1.1: Properties of leptons (adapted from [2]).

quarks	electric charge (e)	mass
u	2/3	2-8 MeV
d	-1/3	5-15 MeV
c	2/3	1-1.6 GeV
s	-1/3	100-300 MeV
t	2/3	168-192 GeV
b	-1/3	4.1-4.5 GeV

Table 1.2: Properties of quarks (adapted from [2]).

they interact with each other. But despite the success of the

Standard Model, there are many gaps in our understanding, like why are there three generations of fermions and what is the dark matter that constitutes the majority of the material in the universe? It is still not known what is the origin of particle masses and what determines their masses and other properties. Many other puzzles remain to be solved. The unification between the theory of the two interactions, strong and electroweak, is not realized and gravity can not be understood at

the quantum level. The questions that we can ask today are as exciting as any in the past and the progress in our understanding of physics must be the result of the interplay between theory and experiment.

1.1 Physics at the TeV Energy Scale

It could be argued that particle physics stands at the threshold of a new era in which we will move from measuring the properties of the Standard Model to understanding what determines these properties. It is expected that this new physics will become apparent at energy scales of a few hundred GeV and some physics scenarios beyond the Standard Model have been developed as energies are increased. The physics programme at the TeV energy scale has been developed through numerous theoretical analyses and the essential elements are summarised here.

1.1.1 Higgs Field

The Standard Model cannot predict the mass of the particles but it provides a mechanism whereby they can acquire mass. This was done by adding to the theory a hypothetical Higgs field that interacts with all the particles that have mass. The Higgs mechanism breaks the electroweak symmetry and generates the masses of the gauge bosons and fermions. The quantum of the Higgs field is the Higgs boson and supersymmetry predicts that at least five types of Higgs boson exists [3].
The most direct way to test the Higgs physics is to produce and detect the Higgs boson in an experiment. Finding the Higgs boson is challenging but difficult, as the Higgs boson decays quickly and only its decay products can be detected.The LEP [1] experiments at CERN [2], Geneva, have reported a tantalising hint of a Higgs signal at $M_h \approx 115$ GeV but the 95 % confidence level limit on the mass is just above 200 GeV [3].

[1]Large Electron-Positron Collider

[2]Conseil Européen pour la Recherche Nucléaire - European Organisation for Nuclear Research

1.1.2 Supersymmetry

Supersymmetry is the framework in which theoretical physicists have sought to answer some questions left open by the Standard Model. It is a generalisation of the space-time symmetries of quantum field theory that transforms fermions into bosons and vice versa. As a consequence, for every particle there must be a "superpartner" which differs in spin by half a unit. None of these superpartners has been observed so far. All the superpartners are expected to be unstable particles which decay into lighter superpartners, except for the lightest superpartner (LSP) which is stable [1]. The LSP and the neutrinos are forms of matter in the Universe which can feel the weak and gravitational forces but not the other two forces. They do not participate in forming stars and they are treated as "dark matter" whose existence is predicted by supersymmetry.

If supersymmetry exists, it is expected to obtain evidence of it at experiments with a linear collider. Recognizing the presence of superpartners may not be easy. Although the supersymmetry is a powerful theory, there is a variety of assumptions about the masses. Once the masses are known, the decay patterns can be predicted and everything else is determined.

1.2 A Linear Collider or a Bigger Storage Ring?

The physics programme described previously could not be achieved without inputs from the accelerator builders and there is broad agreement in the High Energy Physics community that a linear collider is of fundamental importance for whatever will be discovered.

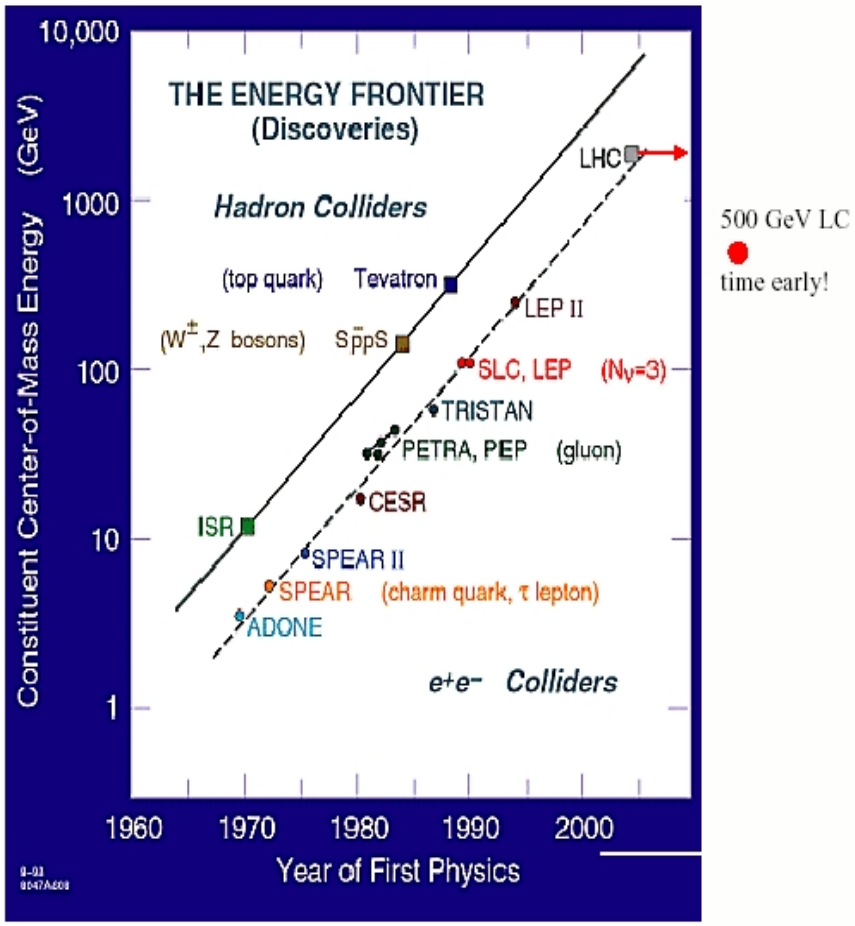

Figure 1.1: The energy frontier for lepton and hadron colliders worldwide (adapted from [5]).

In the past, lepton colliders and hadron colliders have been complementary, and figure 1.1 shows the centre of mass energy limit reached in colliders worldwide. Except for the Stanford Linear Collider (SLC) [4], lepton and hadron colliders have so far been built as storage rings. In a storage ring, the particles are accelerated many times through the same accelerating cavities, and dipole magnets located between these cavities are used to bend the trajectory of the particles. The particles gain a higher energy by adjusting the accelerating field at each turn and as the particles gain more energy at each acceleration, a higher magnetic field is required to bend the particles through the same trajectory.

LEP, the largest e^+e^- storage ring built so far, was closed down in November 2000

although CERN considered extending the life of LEP for another one year to confirm the possible observation of the Higgs boson. However, a postponement of the dismantling of LEP would have delayed for a few months the start of operations of the Large Hadron Collider (LHC), proposed to be built in the same tunnel that once housed LEP [6]. LEP represented an energy limit beyond which energy losses due to synchrotron radiation necessitate moving to linear colliders, thereby raising new challenges for accelerator builders [7]. A general consensus has emerged that the LHC running at a centre of mass energy of 14 TeV, now under construction, should be supplemented by a lepton collider in the TeV range.

The principle of a linear collider is more basic. It consists of two linear accelerators pointed at each other in 180-degree opposition. The beam from each linac is not recirculated and after collision it is dumped away. Thus, the basic, continuous process in each linac is beam generation, beam acceleration, collision and beam disposal, with the repetition of the same as frequently as possible [7]. This is the process used for the first time at SLC, but only one linac was used instead of a pair for economy. The linac accelerated both electrons and positrons, the latter being produced by electron bombardment of a target. The layout of the SLC is presented in figure 1.2.

The concept of a linear collider was first proposed by Maury Tigner in 1965 [9] as the storage ring concept was limited in its energy reach due to synchrotron radiation effects. Synchrotron radiation is the electromagnetic radiation emitted from relativistic charged particles, especially electrons, as they are accelerated [10]. The average power radiated by a single electron (or positron) of energy E for a ring with an average bend field B and a radius R is [11]:

$$P_\gamma = \frac{2}{3}\frac{r_e c}{(mc^2)^3} E^2 F_\perp^2 \tag{1.1}$$

where the transverse force is:

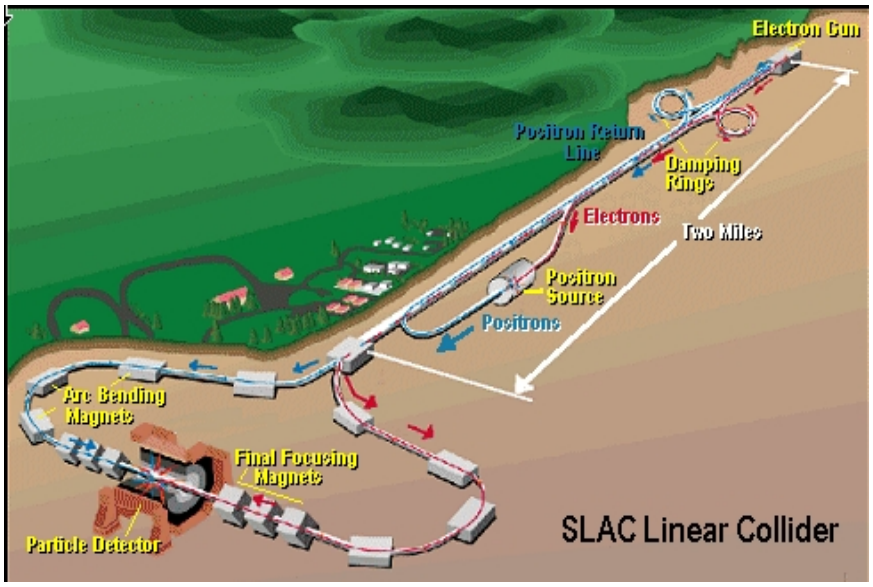

Figure 1.2: The layout of the first linear collider - Stanford Linear Collider (adapted from [8]).

$$F_{\perp} = \frac{e}{c}vB \approx eB = \frac{cp}{R} \approx \frac{E}{R} \tag{1.2}$$

The energy loss per turn in a circular accelerator is:

$$\Delta E_{\gamma} = P_{\gamma}T_{rev} = P_{\gamma}\frac{2\pi R}{c} = C_{\gamma}\frac{E^4}{R} \tag{1.3}$$

where $C_{\gamma} = 8.85 \cdot 10^{-5}$ m$/GeV^3$.

The energy loss per turn has to be replaced by the RF system of the ring, which is a major cost for the collider. It can be seen that the cost of the RF system is proportional to the fourth power of the energy and inversely proportional to the radius of the ring. The main problem is the E^4 dependence of the radiated power as the electrons are forced to go around the ring and this can lead quickly to an energy limitation when the energy loss per turn becomes equal to the energy gain. Therefore, the answer seems to be to keep the particles on a straight line instead of

bending their trajectory and this is exactly the concept of a linear collider.

Although the higher energies are more easily achieved with hadron colliders, (in a storage ring the energy loss due to synchrotron radiation are 10^{13} times lower for hadrons than for electrons [6]), there are two features that make the electron colliders more suitable candidates.
The first feature is the well-defined initial energy state. In the collision electrons and their antiparticles, the positrons, annihilate each other and the resulting energy is converted back into new particles. Both the electron and the positron carry a defined initial energy and provide an accurate knowledge of the reaction under study. This is not the case with hadron collisions where the initial energy of the hadrons is distributed to the component quarks involved in the reaction.
Another feature is the cleanliness of the reaction. The electron and positron being fundamental particles, the resulting states after collision are well-defined. For hadrons, there are an enormous number of final states as the component quarks which interact through the exchange bosons, produce many jets of quarks and gluons. Therefore it is harder to reconstruct the primary event in the case of hadron collisions compared to lepton collisions.

1.3 Key Parameters

There are two critical and key parameters for a high-energy physics collider: centre of mass energy and luminosity.

1.3.1 Centre of Mass Energy

The centre of mass energy E_{cm} represents the energy available for high-energy reactions and depends on the kinematic parameters of the colliding particles. It is defined by the following expression:

$$E_{cm}^2 = (\sum_i E_i)^2 - (\sum_i cp_i)^2 \tag{1.4}$$

With $E_i = \gamma_i m_i c^2$ and $p_i = \gamma_i m_i \beta_i c$, the above relation can be written as:

$$E_{cm}^2 = (\sum_i \gamma_i m_i c^2)^2 - c^2(\sum_i \gamma_i m_i \beta_i c)^2 \tag{1.5}$$

For head on collisions of two equal particles having the same energy and mass ($m_1 = m_2 = m$, $\gamma_1 = \gamma_2 = \gamma$ and $\beta_1 = -\beta_2 = \beta$), the centre of mass energy is simply twice the energy of each of the particles:

$$E_{cm} = 2\gamma mc^2 = 2E \tag{1.6}$$

1.3.2 Luminosity

Assuming that the particle bunches have a Gaussian distribution in both horizontal and vertical plane, the luminosity L of an e^+e^- collider is given by [12]:

$$L = \frac{n_b N_b^2 f_{rep}}{4\pi\sigma_x^*\sigma_y^*} H_D \tag{1.7}$$

where n_b is the number of bunches collided at a repetition rate f_{rep}, N_b is the number of particles per bunch (assumed equal in both beams), $\sigma_{x,y}^*$ are the RMS transverse beam sizes at the interaction point IP (assumed equal for both beams), and H_D is the pinch enhancement factor resulting from the interaction of two oppositely charged bunches (for TESLA, H_D has the typical value of ~ 2 [12]).

1.4 Linear Collider Projects Worldwide

Over the past decades, several groups worldwide have been pursuing different linear collider design concepts. Already in 1971 a group at the Institute of Nuclear

Physics in Novosibirsk started design work for a linear collider of several hundred GeV. Several years later, groups at the Stanford Linear Accelerator Center (SLAC) in California, the Japanese National Laboratory for High Energy Physics (KEK) in Tsukuba and CERN (Geneva) began work on linear collider designs (NLC [13], JLC [14], CLIC [15]). All these concepts are based on normal conducting copper cavities. The main parameters for these linear accelerators for E_{cm}=500 GeV are listed in Table 1.3.

Parameter	unit	TESLA	NLC	CLIC	JLC
Accelerating gradient E_{acc}	[MV/m]	23.4	50	172	49.8
Repetition rate f_{rep}	[Hz]	5	120	200	150
No. of bunches per pulse n_b		2820	192	154	192
Bunch spacing Δt_b	[ns]	337	1.4	0.67	1.4
Charge per bunch N_e	$[10^{10}]$	2	0.7	0.4	0.75
Beam size at IP $\sigma_{x,y}$	[nm]	553, 5	320,3.2	202,1.2	243,3.0
Bunch length at IP σ_z	[um]	400	100	35	110
Luminosity $L_{e^+e^-}$	$[10^{34}cm^{-2}s^{-1}]$	3.4	2	2.1	2.5

Table 1.3: The main parameters for linear collider projects (adapted from [14], [15], [16], [19], [17]).

In contrast, the Deutsches Elektronen Synchrotron (DESY) proposed to build a linear collider called TESLA (TeV Superconducting Linear Accelerator). The TESLA approach differs from the other designs by the choice of superconducting accelerating structures as its basic technology. The TESLA linear collider based on superconducting accelerating structures is ideally suited to meet the requirements needed for a large collision rate, namely very small beam sizes and high beam power (Table 1.3). This is translated into a high luminosity [$10^{34}cm^{-2}s^{-1}$]. TESLA reaches a centre-of-mass energy of 500 GeV, which can be extended to about 800 GeV without

increasing the length of the machine.
A prototype superconducting linear accelerator was built as part of the TESLA Test Facility (TTF) [18] in order to gain long term operating experience and it has been operated successfully.

In conclusion, the journey of discovery is not nearing an end, and it is expected that what follows is a period of more exciting discoveries and surprises rivalling those of the last century. In particle physics, the experiments depend on the performance of the particle accelerators and the most ambitious machine likely to be built in the immediate future is a linear collider.

The simulation work that I performed for the TESLA linear collider is presented in this thesis. The general layout of the accelerator with emphasis on the beam delivery system and technical details is presented in chapter 2. A discussion of beam dynamics, in particular production, acceleration and transport of the beam are discussed in chapter 3. Chapter 4 describes how the beam lattice and beam dynamics were modelled in a computer simulation program called "MERLIN". The collimation system and notions about machine protection system are presented in detail in chapter 5 and special attention is given to the collimators. Chapter 6 shows the results obtained with the simulation code for beam offsets and calculation of temperature rise on the spoilers, while chapter 7 presents the results obtained after particle scattering was added in the simulation code. Chapter 8 contains a data analysis and presents the conclusions.

Chapter 2

The TESLA Linear Collider

From its onset in 1992, the TESLA project[1] was developed at DESY by a large international collaboration of scientists, engineers and technicians from more than 40 institutes in 9 countries. A complete description of the machine including estimates of project cost and construction schedule is given in the design report published in spring 2001 [19]. Due to its ability to conserve a high beam quality during acceleration, the TESLA linac is also an excellent driver for an X-ray Free Electron Laser (FEL) and such a laboratory is proposed to be built as an integral part of the TESLA project.

The linear collider design is made up of several sub-systems each of which accomplishes a different task: injection systems which generate electrons and positrons, damping rings to decrease the beam emittance (the volume occupied by the bunch in phase space[2]), bunch compressors to decrease the damping ring bunch length to something matched to the main linac, main linacs to accelerate the beam to the desired energy without diluting the beam emittance and beam delivery systems which lead and properly focus the beams to the IP. An overview of each of these sections is given in this chapter and a schematic of TESLA is shown in figure 2.1.

[1] The TESLA Technical Design Report (TDR) [19] was used extensively throughout this chapter.

[2] see section 3.3.1

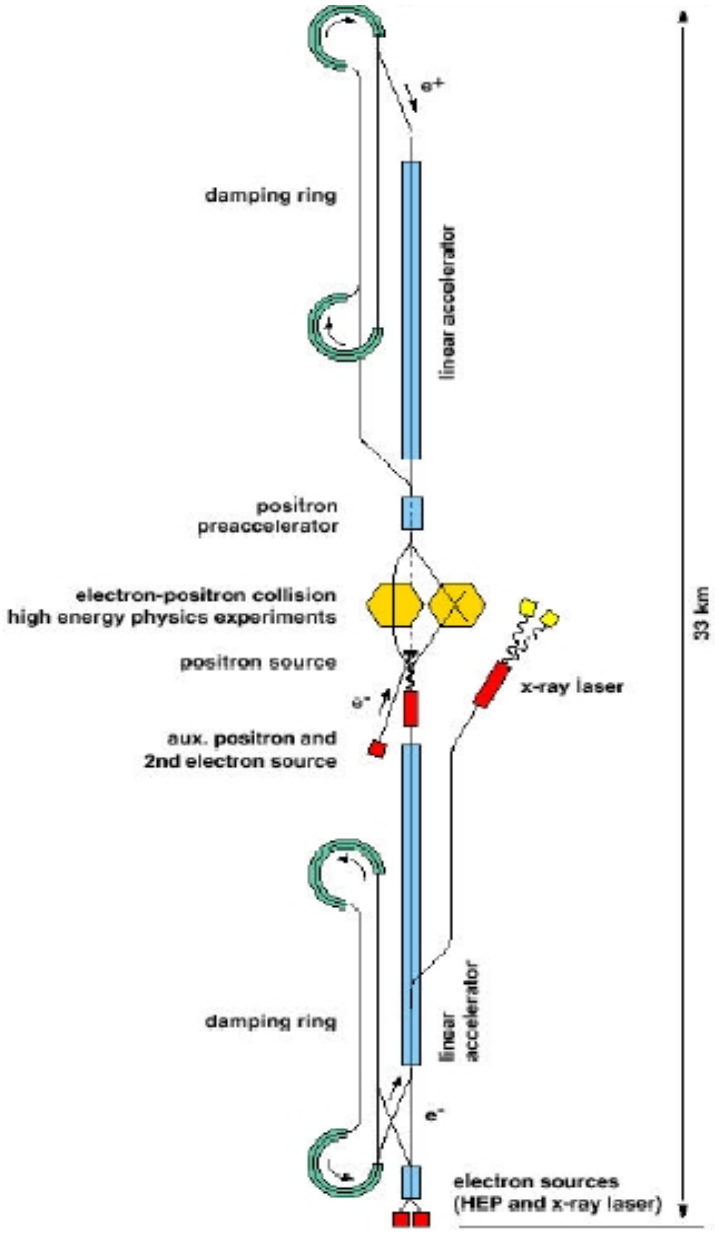

Figure 2.1: Overall layout of TESLA (adapted from [19]).

2.1 Injection Systems

The injection system is required to produce long bunch trains of electrons and positrons with a high charge (few nC per bunch [19]) and small emittance, and also with spin polarisation for physics experiments.

2.1.1 Electron production

Electrons are easy to produce experimentally by thermionic and photoelectric emission processes. For TESLA, the electrons are provided by three separate injectors: a polarised electron gun for the collider, a non-polarised laser driven radio frequency (RF) gun for the collider and a laser driven RF gun for the FEL. The polarized injector is intended as the primary source for the collider because polarized beams can aid physics analysis greatly. The RF gun can be used both for commissioning and as a backup to the polarised source.

The concept of a polarised laser-driven photo-injector is shown in figure 2.2. The GaAs cathode produces polarised electrons when it is illuminated with a laser light of 840 nm wavelength and this source is capable of producing over 90% polarisation. The emittance produced by such a gun is dominated by space-charge effects and is typically of the order of 10^{-5} m rad (a factor of 10 too big for emittance in the horizontal plane, and a factor of 500 too big in the vertical). Unfortunately, the GaAs cathodes are extremely sensitive and requires very high vacuum (the pressure is less than 10^{-11} mbar)[12]. Because the gun is effectively DC (direct current), the polarised source requires a bunching section and the operating principles of a buncher will be discussed in the next chapter.
The three electron sources share a common superconducting electron injection linac for acceleration from 500 MeV to the damping ring energy of 5 GeV.

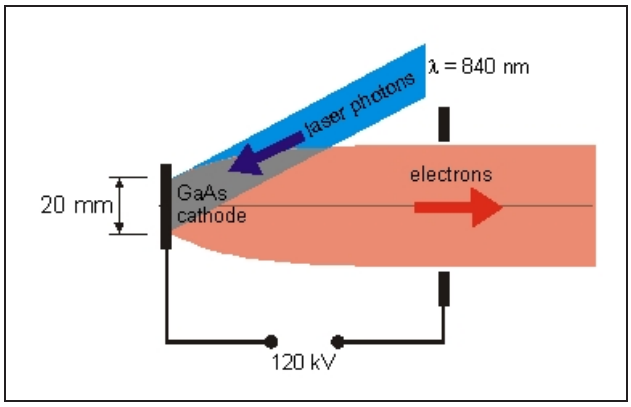

Figure 2.2: Conceptual layout of the laser-driven photo-injector for electron production (adapted from [12]).

2.1.2 Positron production

The positron injection system has to provide a total charge of about $5 \cdot 10^{13}\, e^+$ per beam pulse, and this is not realistically feasible with a conventional (electron on thick target of $\sim$ 4 radiation lengths [12]) source. In a conventional source, electrons generate photons via bremsstrahlung and the photons convert within the same target into e^+e^- pairs. The electrons are highly energetic (>GeV) and the target should survive both the single pulse heating and the average heating. The average heating is handled by cooling and rotating the target so pulses strike different areas, but the single pulse heating must be handled by reducing the cross-sectional density of the incoming electron beam - this limits the number of positrons that can be produced.

For this reason TESLA has adopted a different approach where high-energy photons are directed onto the target rather than electrons - this reduces one stage of the shower production and allows the use of a thin target with a much lower energy deposition [20]. The photons are generated by sending the high energy electron beam (150-250 GeV) through a long planar undulator magnet placed upstream of the collider interaction point (figure 2.3). The photons are then converted into e^+e^- pairs in a thin rotating target ($\sim$ 0.4 radiation lengths). This scheme has the ad-

vantage of a low energy deposition in the target itself ($\sim$ 5 kW as opposed to 22 kW for a conventional source [12]) and a relatively high capture efficiency. The generated positron beam has a smaller longitudinal and transverse emittance due to less Coulomb scattering in the target (roughly a factor of two over a conventional source [12]).

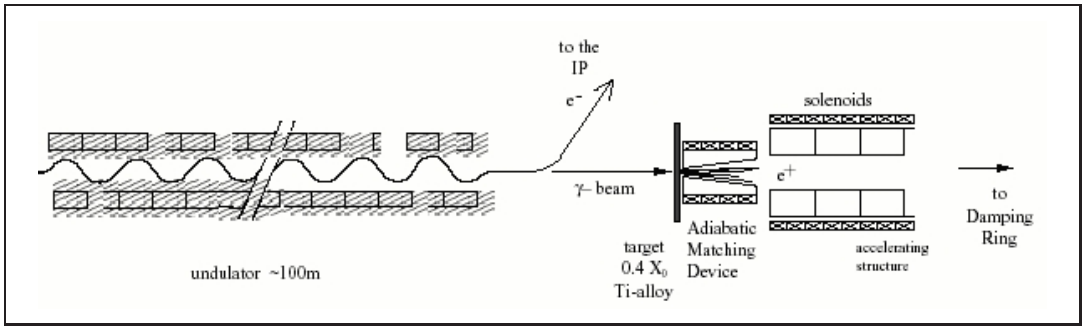

Figure 2.3: The long planar undulator (adapted from [19]).

Unfortunately, the undulator source has two disadvantages. Firstly, it requires a high energy electron beam which is then transported to the IP or further accelerated, depending on the location of the positron source. This introduces a fundamental coupling between the electron and positron linacs, the former being required before the later can operate fully. Secondly, the undulator source has never been realised, and due to the high electron beam energy required, it is unlikely to be tested before the linear collider is built [12]. However, in order to test the performance of the superconducting linac, the TESLA collaboration has built a 13.5 m long prototype undulator for a FEL at TTF [21].

The positrons are then sent through the normal conducting pre-accelerator where they are separated from the electrons and the photon beam, and accelerated up to an energy of 250 MeV. After acceleration in copper cavities (they withstand the relatively high particle losses expected in the region), the positron beam is sent to a long transfer line which guides the positrons below the experimental hall to the

other side of the IP. The beam is then further accelerated in a superconducting linac to an energy of 5 GeV before being injected into the damping ring.

2.2 Damping Rings

The emittances produced by the sources are too large by several orders of magnitude, therefore a damping ring is necessary to reduce the emittances to the small values required for high luminosity at the IP (see section 1.3.2). The challenges for the ring are: to have sufficiently large dynamic apertures to capture the incoming beams, to damp the beams sufficiently fast and to generate the very small emittances desired at the IP. Emittance reduction is achieved via the process of radiation damping, i.e. the combination of synchrotron radiation in bending fields with energy gain in RF cavities.

The final extracted transverse emittance ϵ_f is given by [12]:

$$\epsilon_f = \epsilon_i \; exp\left(-\frac{2T}{\tau_D}\right) \; + \; \epsilon_{eq}\left[1 - exp\left(-\frac{2T}{\tau_D}\right)\right] \tag{2.1}$$

where ϵ_i is the initial (injected) emitance and ϵ_{eq} is the equilibrium emittance ($\epsilon_{eq} \sim E^2/\rho$, where ρ is the radius of the damping ring); T represents the storage time given by the ratio of the number of bunch trains stored at one time N_s and the repetition rate of the machine f_{rep}, $T = N_s/f_{rep}$, and τ_D is the damping time defined as twice the time required for an electron to radiate all its initial energy [12] ($\tau_D = 2E/P_\gamma$ where E is the damping ring energy and P_γ, the average radiated power per electron). The initial normalised positron emittance is 0.01 m rad, and ∼7 damping times (28 ms) are required to achieve the final design normalised emittance of $2 \cdot 10^{-8}$ m rad. The injected electron beam, having been produced by a photoinjector as opposed to a target, has a much better beam quality ($\epsilon_i \approx 10^{-5}$

m rad), and only requires 4 damping times [19].

The quantum nature of photon emission gives a horizontal emittance $\epsilon_x \neq 0$. The photons are emitted in a narrow cone approximately collinear with the direction of travel of the particle and with a typical angle of γ^{-1} (~ 250 μr for 2 GeV) and these random angle kicks add emittance to the beam. Therefore, the minimum achievable vertical emittance is limited by the following effects [12]:

- intra-beam scattering, which begins to become important as the charge density increases during damping [10];
- instabilities, such as fast ion (places constraints on the vacuum system)[22] and electron cloud (sensitive to the surface properties of the vacuum chamber) [23], [24], [25];
- magnet misalignments, which cause close orbit deviations leading to cross-plane coupling and spurious vertical dispersion [10].

All these effects are important and can cause serious degradation of the emittance if not corrected.

One of the main design criteria for the damping ring comes from the long beam pulse: a 1 ms pulse containing 2820 bunches. Because bunches in TESLA are spaced far apart (337 ns), storing the uncompressed TESLA bunch train would require a ring circumference of ~300 km. To keep the damping ring length reasonable, the bunch train has to be stored in a compressed mode with a much smaller bunch spacing than in the rest of the accelerator. Even with this compression a large ring circumference is still required as the circumference is given by:

$$C = cN_s n_b t_b \tag{2.2}$$

where c is the velocity of light, N_s is the number of bunch trains stored at one time, n_b is the number of bunches in a bunch train and t_b is the bunch spacing.

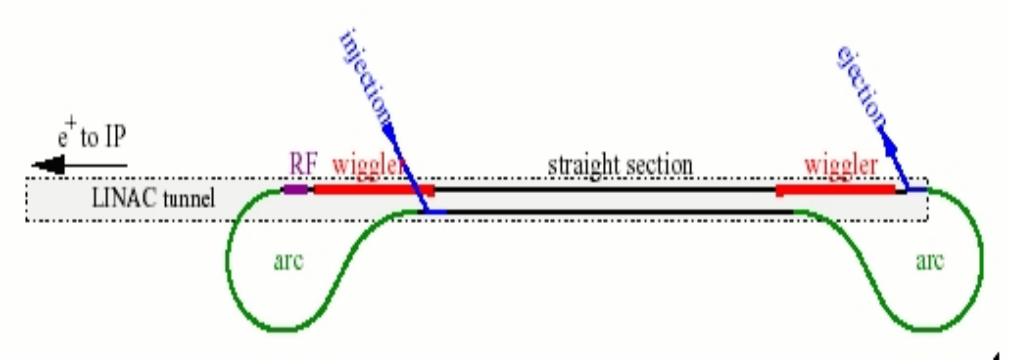

Figure 2.4: Conceptual layout of the positron damping ring (adapted from [19]).

To avoid building an additional large ring tunnel, a so-called "dog-bone" design is used (figure 2.4) which places most of the damping ring in the same tunnel as the main linac [26]. The layout has two 8 km straight sections placed entirely in the linac tunnel, additional tunnels are only required for the 1 km circumference loops at either end. The damping ring lattice can be divided into three separate parts: the arcs, the wiggler sections and the long straight sections in the linac tunnel. The design of low emittance arcs with sufficiently high bending fields to provide enough damping becomes increasingly difficult at higher energies: thus the majority of the damping (95%) is supplied by long damping wigglers (series of equal dipole magnets with alternating magnet field direction [11]). By introducing extra bending, the wiggler has the effect of reducing the damping time and it is desirable to be placed in a section where the dispersion is zero (the offset of the reference trajectory from the ideal path) as the wiggler itself generates some self-dispersion through bending the beam [27]. Fast kickers are required for compression and decompression of the bunch train at injection and extraction respectively. They are very rapidly pulsed magnets with a pulse duration of 1 μs which deflects the beam out of the machine at the end of the accelerating cycle [28].
A summary of the main parameters of the positron and electron damping rings is given in Table 2.1 [19].

Because the damping rings produce beams of length about 6 mm, too long by an

TESLA-500	
Energy	5 GeV
Circumference C	17 Km
Hor. extracted emittance $\gamma\epsilon_x$	8×10^{-6} m rad
Ver. extracted emittance $\gamma\epsilon_y$	0.02×10^{-6} m rad
Injected emittance $\gamma\epsilon_{x,(y)}$	0.01 (10^{-5}) m rad
Number of damping times n_τ	7.2 (4.0)
Cycle time T_c	0.2 s
Damping time τ_d	28 ms (50 ms)
Bunch spacing $\Delta\tau_b$	20×10^{-9} s
No. of bunches n_b	2820
No. of particles per bunch N_e	2.0×10^{10}
Current	160 mA
Energy loss/turn	21 MeV (12 MeV)
Total radiated power	3.2 MW (1.8 MW)
Tunes Q_x, Q_y	72.28, 44.18
Chromaticities $\xi_x, \xi y$	-125, -68
Momentum compaction α_c	0.12×10^{-3}
Equilibrium bunch length σ_z	6 mm
Equilibrium momentum spread σ_p/P_0	0.13% (0.1%)
Transverse acceptance $A_{x\|y}$	0.05 m (0.012 m)
Momentum acceptance A_p	1% (0.5%)

Table 2.1: Parameters for the TESLA positron damping ring. Where different, values for the electron damping ring are given in parentheses (adapted from [19]).

order of magnitude for optimum collider performance (σ_z =0.3 mm), the beams are then sent to the bunch compressors to be shortened.

2.3 Bunch Compressors

The bunch compressors are the sections located after the damping rings and before the main linacs where the bunches are compressed longitudinally by a factor of ∼20 before being accelerated in cavities. The bunches are shortened for two reasons: to prevent large energy spread in the linac due to the curvature of the RF and to reduce the transverse wakefield emittance dilutions.

Compression is achieved by introducing an energy-position correlation along the bunch length using a RF section, followed by a dispersive beamline with an energy dependent path length [29]. Figure 2.5 outlines the concept. Only the longitudinal phase space is considered when the bunch passes through an RF cavity on the zero crossing of the voltage (i.e. no mean acceleration). The RF cavity has no effect on the longitudinal position of a particle with respect to the bunch center, but changes the energy deviation by an amount depending on its position [12]. The bunch is then transported through a dispersive section constructed from a dipole chicane (

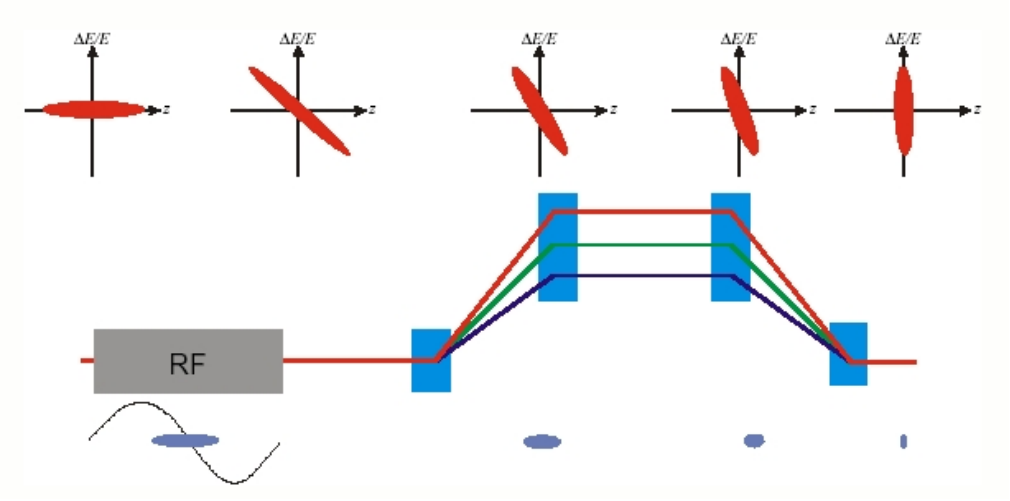

Figure 2.5: Bunch compression by a $\pi/2$ longitudinal phase space rotation (adapted from [12]).

four dipole magnets make up a chicane that compresses the bunch). At this stage, the particles at the tail of the bunch are increased in energy, so they take a longer path (the bending radius is larger), and thus move towards the head of the bunch. Particles at the head of the bunch are decreased in energy, so they take a shorter path and move towards the tail of the bunch. In this way, the bunch is compressed longitudinally, or more precisely, the bunch is rotated in phase space.

From the conservation of longitudinal emittance, the final relative (rms) energy spread is $\delta \equiv \sigma_{\delta_i} \frac{\sigma_{z_i}}{\sigma_{z_f}}$, where σ_{z_i} is the initial (damping ring) bunch length, σ_{z_f} the final (compressed) bunch length, and σ_{δ_i} the initial (damping ring) rms relative energy spread. From the relation above it can be seen that the bunch length is reduced at the expense of increasing the energy spread. The large rms energy spread of $\sim$3% [19] in the compression section means that the non-linear terms in the path length are significant. The main parameters for the beam before and after bunch compressors are given in Table 2.2. It is worth mentioning that the bunch length is preserved during acceleration in the main linac which is the next section of the accelerator.

TESLA-500	
horizontal emittance $\gamma\epsilon_x$	8×10^{-6} m rad
vertical emittance $\gamma\epsilon_y$	0.02×10^{-6}m rad
initial bunch length σ_z	6 mm
initial energy spread σ_{δ_i}	0.13%
beam energy E_0	5 GeV
final bunch length σ_{z_f}	0.3 mm
final energy spread σ_{δ_f}	2.7%
compression ratio	20

Table 2.2: Beam parameters before and after the TESLA bunch compressor (adapted from [19]).

2.4 The Linacs

The linac is the major component of a linear collider where the electron and positron bunches are accelerated in cavities from the damping ring energy of 5 GeV up to the desired IP energy of 250 GeV. The electron and positron linacs have a total length of 14.4 km each, including a $\sim 2\%$ overhead for energy management in case of klystron failures (klystrons are the vacuum tubes which generate microwaves to accelerate particles). The RF system consists of 286 10MW klystrons per linac (including overhead), which are installed in the tunnel and connected to the pulsed power supplies (modulators) in external service halls by high voltage cables. Table 2.3 lists some important linac parameters relevant to beam dynamics issues for both the HEP and FEL beams.

A fundamental design goal for a LC is to minimise the active acceleration length in the machine and thereby to reduce the cost of the RF system. It is desirable to use accelerating structures with as many cells as possible both to increase the filling time (the time required for the cavity to reach the required voltage) and to reduce the number of power couplers used to pump power into the structure. However, the number of cells per cavity is limited by the condition of field homogeneity as the sensitivity of the field pattern to small perturbations grows quadratically with the number of cells [19]. A 9-cell structure is close to the optimum. Therefore, TESLA cavities are 9-cell standing wave structures of about 1 m length made from solid niobium and bath-cooled by superfluid helium at 2 K (figure 2.6). The cell length is determined by the condition that the electric field has to be inverted in the time a relativistic particle needs to travel from one cell to the next. The cells have a spherical contour near the equator and a large iris radius to reduce wakefield effects (wakefield is electromagnetic radiation given off by fast moving charged particles as a result of their interaction with the surroundings [11]). Each cavity is equipped with a helium tank, a tuning system, two higher-order mode HOM couplers, a RF power coupler and a pickup probe (figure 2.6).

The cavities are similar in layout to the 5-cell 1.5 GHz cavities of the electron accelerator CEBAF, which were developed at Cornell University [31]. The CEBAF cavity manufacturing methods were adopted for TESLA and improved quality control of the superconducting material and of the fabrication methods combined with an extremely careful handling of the cavities were necessary. This has led to accelerating fields which exceed the original TESLA-500 design goal of 25 MV/m [19]. The design centre of mass energy of 500 GeV corresponds to a gradient of 23.4 MV/m. The energy upgrade to 800 GeV requires use of the so-called "superstructure", where the effective acceleration length is increased by combining together several multicell cavities with reduced inter-cavity spacing. The accelerating field gradient required is then 35 MV/m, which represents a significant increase compared to the performance achieved so far.

The accelerator modules (cryomodules) consist of twelve 9-cell cavities, a quadrupole, steering coils and a beam position monitor (BPM). The helium distribution system needed to operate the superconducting cavities and magnets at 2 K is also integrated into the module.

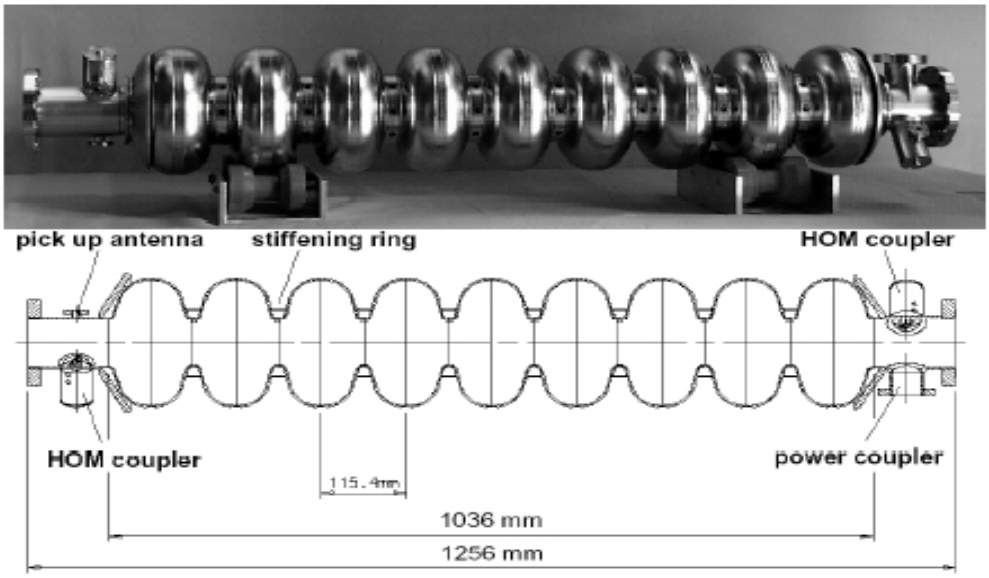

Figure 2.6: Side view of the 9-cell cavity (adapted from [30]).

Tesla - 500 GeV		
	Collider	FEL
Accelerating gradient ϵ_{acc} [MV/m]	23.4	9.2-23
Injection energy E_i [GeV]	5	2.5
Bunch charge N_e [10^{10}]	2.0	0.63
Bunch spacing Δt_b [ns]	337	93
Bunch length σ_z [μm]	300	25-50
Norm. design emittance $\epsilon_{x,y}$ [$10^{-6} m$]	10,0.03 (IP)	1.5(undulator)
Norm. emittance at injection $\epsilon_{x,y}$ [$10^{-6} m$]	8, 0.2	0.9
Beam size at injection $\sigma_{x,i}$ $\sigma_{y,i}$ [μm]	320, 16	150
Beam size at linac exit $\sigma_{x,f}$ $\sigma_{y,f}$ [μm]	60, 3	35-60
Beta function β_{max} [m]	127 at 5-125 GeV 167 at 125-250 GeV	
Initial uncorr. energy spread $\sigma_{E,i}/E$ [%]	2.5	0.1
Correlated energy spread δ_{cor} [10^{-4}]	3	10-1
Total spread $\sigma_{E,f}/E$ at linac exit [10^{-4}]	6	10-1.5

Table 2.3: Beam parameters in the main linac (adapted from [19]).

Cost economy in a long linac calls for a small cavity design and consequently a frequency well above the 350 to 500 MHz used in storage rings. The frequency can not be made arbitrary high, however, because of the f^2 dependence of the surface resistance and of the f^2 and f^3 dependence of the wakefields $W_{\parallel}$ and $W_{\perp}$, which at 3 GHz already limits the attainable gradient to ≈30 MV/m [32] . The optimum frequency is in the 1.5 GHz regime and the choice for 1.3 GHz was motivated by the availability of high power klystrons.

2.5 Beam Delivery Systems

The Beam Delivery System (BDS) transports the beams from the exit of the linacs to the interaction point, where they are brought into collision, and then safely extracted and dumped in high-power beam dumps. The BDS is 3436 m in length (linac to linac) with the e^- and e^+ delivery systems being 1759 m and 1677 m in length respectively. The slight asymmetry is due to the undulator-based e^+ source at the exit of the e^- linac. From the first bend magnet in the switch-yard (see section 2.5.1) both lattices are identical. The IP itself sits slightly off-center.

The current version of the beam delivery system for the TESLA linear collider reflects several major modifications with respect to the reference design given in [33]. The BDS system is required to perform the following functions [34]:

- strong demagnification of the beam to the final focus, resulting in the 550nm and 5nm beam spots at the IP;
- maintain the beams in collision using active stabilization (feedback);
- cleanly extract the strongly disrupted beams after the IP, and transport them to high-power dumps;
- a high level of machine (and detector) protection, in the event of a linac fault resulting in a beam with a large energy error or a large orbit deviation or both;
- collimation of large amplitude particles (the so-called beam halo) coming out of the linac, which would cause significant background in the physics detector;
- diagnostics for the linac (an emittance measurement station is included in the collimation section β-COLL);
- inclusion of a switch-yard to separate the beamline serving the (optional) second interaction region (IR).
- incorporation of the e^+ source at the e^- exit of the linac;

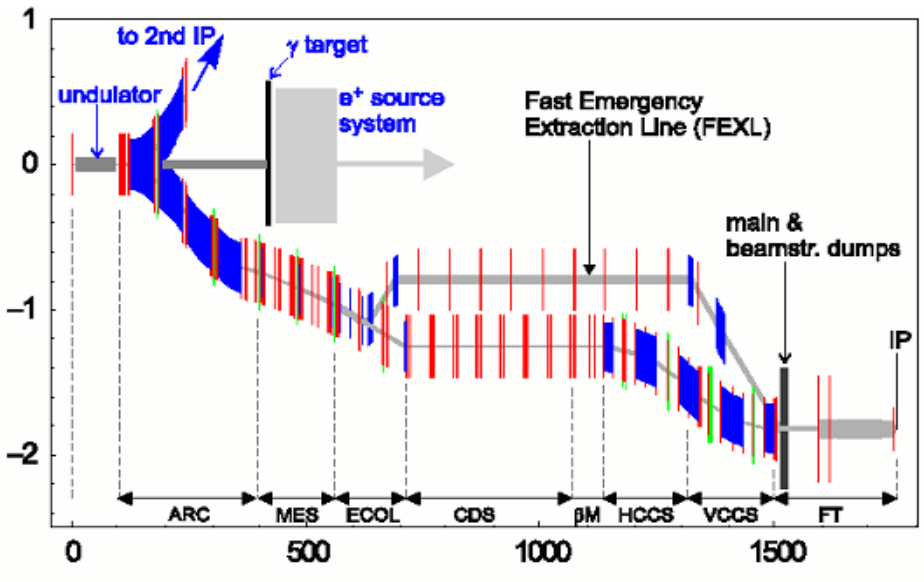

Figure 2.7: Geometry of the primary e^- BDS from linac to IP (adapted from [19]).

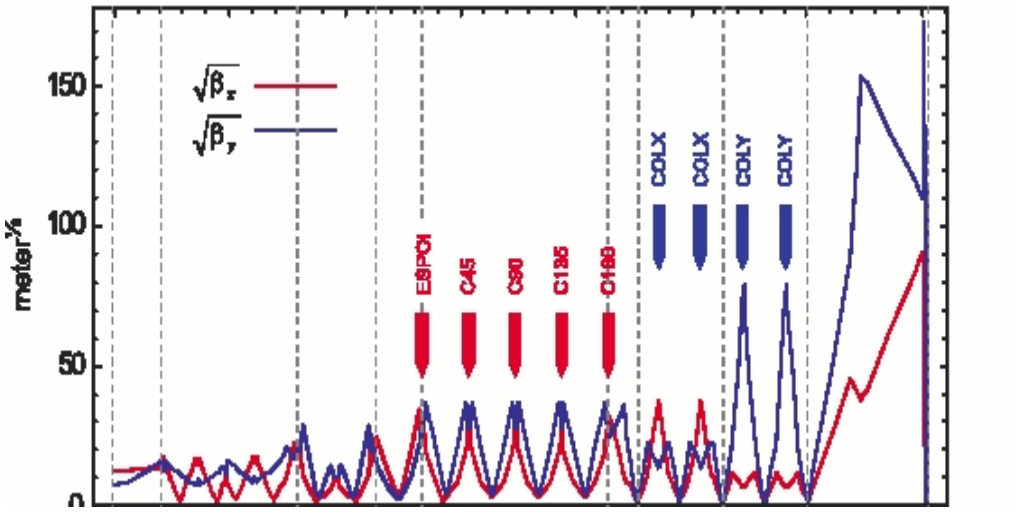

Figure 2.8: Optics functions for the TESLA BDS (e^-) (adapted from [35]).

The various modules in the BDS which separate out these functionalities are shown

in figure 2.7. The optics functions[3] for the BDS are presented in figure 2.8.
Firstly, there is the e^+ source undulator which contains space for the e^+ source undulator and the switch-yard arc (ARC), a double bend achromat arc which acts as a switch to a second IR and allows enough clearance for the e^+ source photon target. The switch-yard is followed by the collimation and diagnostics system (CDS) which comprises three modules [34]: a magnetic energy spoiler (MES) which is a dispersive section containing non-linear elements which expand the beam at the downstream energy collimator (ECOL) in the event of a large energy error. Then there is the betatron collimation and diagnostics section (BCDS) which is a repeating lattice where a series of collimators are used to collimate the beam halo; this area will be also used to support the primary emittance measurement station.
The β-Match section (βM) is responsibile for matching the beam optics from the CDS to the entrance of the final focus system (FFS).
The final focus system is composed of three components - the horizontal chromatic correction system (HCCS), the vertical chromatic correction system (VCCS) and the final telescope (FT) which is a second-order achromatic telescope system which focuses the beam to the IP.

The figure also shows the Fast Emergency Extraction Line (FEXL) and an indication of the location of the positron source system. The IP has a transverse offset with respect to the linac of 1.82 m, and the net bending angle from linac to IP is zero.

2.5.1 Positron Source Undulator and Beam Switchyard

A) The Undulator

After the linac exit, the high energy electron beam passes through a 100 m long wiggler where photons are produced. These photons are then converted into electron and positron pairs on a target located 300 m from the wiggler exit [36]. The

[3] see section 3.3.2

electron beam is switched after the wiggler and transported towards either one of the two collision points. In the case of the e^- BDS, the undulator for the e^+ source is installed directly after the linac. It is ∼100 m in length and its gap size (in terms of nominal electron beam size) must be larger than the apertures defined by the downstream halo collimation system in the beam delivery system ($13\sigma_x \times 80\sigma_y$). With an elliptical vacuum chamber of half-gap 5 mm horizontally and 1.5 mm vertically, the normalised aperture is ($79\sigma_x \times 350\sigma_y$), significantly larger than the collimation aperture. The undulator increases the relative energy spread in the beam to about 0.15%, as compared to $\leq 0.05\%$ coming out of the linac.

B) The Beam Switchyard

Immediately after the undulator, the beam switchyard may be set to steer the e^- beam to either of the interaction points as the option of a second interaction region was integrated in the layout of the TESLA facility. This second interaction region has a crossing angle of ∼34 mrad (the primary interaction region has zero crossing angle) and is suitable for $e\gamma$ and $\gamma\gamma$ collisions [36].
On the positron side, the switchyard will be symmetric to the electron one.

The design of the beam switchyard is driven by the following constraints:

- it must bend the electron beam horizontally away from the straight photon beam strongly enough to avoid and make room for the positron target system;
- the horizontal emittance growth due to synchrotron radiation should be kept to an acceptable minimum;
- it must operate at 250 GeV and 400 GeV beam energies.

Two designs for the beam switchyard optics were proposed: one based on a FODO transport system (a lattice composed of focusing and defocusing quadrupoles) and one based on a double bend achromat system used in modern light sources to significantly reduce the horizontal emittance growth from synchrotron radiation effects. The first one gives an emittance growth about 20% of the nominal 10^{-11} mrad

as the quadrupoles cannot be tuned to minimize the emittance growth. The second one can achieve a minimum emittance growth of 8% of the nominal emittance by realizing a waist of the horizontal β_x function[4] at 1/3 of the arc dipole length [36].

The second design was chosen for TESLA. A first bending of 8 mrad over a 90 m long arc deviates the electron main trajectory by 0.6 m transverse distance from the positron target. Towards the main e^+e^- interaction point, it is followed by a second arc with a net bending of about the same magnitude but opposite in sign such that, when added to rest of the beam line, the net bend angle is zero at the IP. The positive and negative arcs are realised with twelve 1.5 m long dipoles. For simplicity, the dipoles are identical in each arc, with slightly different field settings.

On both sides of the arcs, beam matching from the upstream wiggler exit to the downstream entrance of the collimation section is provided by matching sections with four quadrupoles.

2.5.2 The Collimation and Diagnostics System

At the TESLA beam parameters (E=250 GeV, N=$2{\cdot}10^{10}$ particles per bunch with 2820 bunches per pulse) the loss of a small fraction of the beam along the beam line affects strongly the background conditions in the detector and causes irradiation and heating of the collider components. Large amplitude particles cause synchrotron radiation incident on the final doublet if not removed, so a collimation system is necessary. It is also necessary for safety reasons, to protect the beamline and detector from destruction with a mis-steered beam.

The collimation system is intended to localize the beam loss in a specially equipped short part of the beam line to prevent particle loss in other parts of the collider.

[4] see section 3.3.2

The philosophy of the TESLA beam collimation system is to use large aperture quadrupoles and only collimate the beam at as large as possible amplitudes in order to minimize background produced by the collimators.

In addition to removing the large amplitude or off-energy halo particles, the collimation system for TESLA-BDS fulfills several other functions, namely:

- it protects the downstream beamline components against mis-steered beams in case of a subsystem failure;
- the collimation should be sufficiently far away from the collision point to allow for a suppression of the number of muons generated by the collimation;
- it provides emittance measurement (diagnostics) for the linac, using profile monitors close to each collimator (spoiler) location [37].

In the original reference design [33], the collimation system and the diagnostics section (emittance measurement station) were two separate systems. In order to save tunnel length, these two separate systems have been merged into one collimation and diagnostics section [34].

A) Magnetic Energy Spoiler

The magnetic energy spoiler is the first component of the collimation and diagnostics system. The system is characterized by having a double peaked dispersion function. The first peak is at the so-called magnetic energy spoiler, which forms part of the machine protection system. It is primarily intended to protect the downstream (mechanical) energy spoiler from being damaged by a direct hit from an off-energy beam. In the event of a beam energy error at $> 2\%$, the MES serves two related MP functions:

- a BPM placed at the high dispersion peak is used to send a signal to the downstream fast kicker system of the FEXL, causing the remainder of the bunch train to be safely extracted to the main dump;

- the non-linear magnets in the system significantly increase the vertical beam size on the face of the downstream energy spoiler, allowing the collimator to survive a few bunches from the train.

B) Energy Collimator

Downstream of the MES is the energy collimator[5] which must be protected by the first one. The current philosophy is to protect the collimators from energy errors, since these are the most likely (frequent) type of error we can expect from the linac. Large orbit (pure betatron) oscillations of sufficient amplitude to strike a collimator are probably rare events by comparison: the typical scenarios tend to be magnet failures, which occur relatively slowly with time scales ($\sim 100\mu$s), and can be detected and controlled by monitoring.

C) Betatron Collimation and Diagnostics Section

The betatron collimation system is the last component of the CDS. Betatron collimation is performed at four betatron collimators at intervals of 45° phase advance[6] , at locations of relatively large beam size ($\sigma_x = 127\mu$m, $\sigma_y = 7\mu$m at 250 GeV). Such a design also provides for an efficient emittance measurement station. For the monitors themselves, both flying carbon-wire monitors and laser-wires are envisaged, the latter being used during normal luminosity operation.

2.5.3 Final Focus System

Once the bunch has been compressed longitudinally and accelerated, one must focus the beams and collide them at the IP. The final focus system performs the demagnification of the beams down to the small sizes required for high luminosity ($\sigma_x =$ 550 nm and $\sigma_y = 5$ nm) and uses sextupoles in a dispersive region to cancel the

[5] see section 5.2.1

[6] see section 5.2.2

large chromaticity (deviation of particle energy from the ideal design energy [11]) of the demagnifying final lenses. It comprises a chromatic correction system and a final telescope.

A) Chromatic Correction System

The Chromatic Correction System consists of two dispersive sections respectively performing horizontal and vertical chromatic correction, where pairs of strong sextupoles are used to correct the strong chromaticity induced by the final doublet. The final doublet provides a strong focusing of the beam and requires magnets with very high quadrupole gradients, typically hundreds of Tesla per meter [12].

B) Final Telescope

The demagnification is performed by a point-to-point telescope system situated downstream of the chromatic correction systems. In order to allow a clear extraction path for the beamstrahlung from the IP to the main dump hall ($\sim$ 200 m from the IP), the length of the telescope has been significantly increased beyond that which would naturally be required. In order to re-establish the correct optics, an additional weak doublet is therefore required approximately 130 m upstream of the final doublet. The length of the FFS system is approximately 700 m long, compared to $\sim$ 500 m for the system described in [33].

2.5.4 Interaction Region

The layout of the interaction region is shown in figure 2.9. The most important regions are:

- the instrumented mask constructed from high Z material to absorb most of the e^+ e^- pairs and their secondaries;
- the cryostat housing the final super-conducting quadrupole doublet.

In the beam direction, the aperture limitations are set by the forward cylindrical mask of 24 mm diameter housing the pair luminosity monitor, and by the super-conducting quadrupole doublet itself, consisting of a 1.7 m and a 1.0 m long quadrupole with an inner diameter of 48 mm.

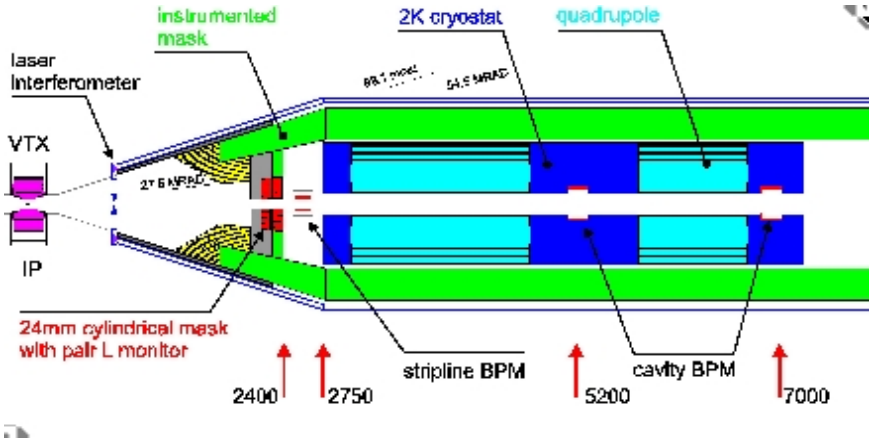

Figure 2.9: Interaction region (adapted from [19]).

The figure also shows the instrumentation required for beam tuning: one stripline and two BPMs, which are primarily used by the inter-bunch fast feedback system, a laser interferometer for single beam profile measurement at 0.8 m from the IP, and one luminosity monitor (pair counter) on each side of the IP located at the lowest aperture radius of 1.2 cm on the inner mask. Finally, a slower luminosity monitor, integrating the bremsstrahlung signal over about 10 bunch crossings, is foreseen around the beam pipe at 8.5 m from the IP (not shown).

Chapter 3

Beam Dynamics

Having given this brief picture of the TESLA linear collider, it is worth pausing for a short diversion into the physics of particle accelerators since it is essential to any further work which is conducted, and leads also to an understanding of the main issues presented in this thesis. There exists a wealth of technical literature (ie. [39], [40], [11] etc.) in which the full, mathematical treatment of beam dynamics is covered. This chapter gives only a qualitative review of the basic terminology and kinematic equations with simple explanations outlined for each of them.

When studying the fate of the beam in an accelerator from the time it is made until it is used, several steps are involved. The production of the beam is the first step, then the energy of the beam must be increased so there has to be a mechanism for acceleration. Next, the beam must be transported to the IP where it is used in experiments.

3.1 Production of the Beam

The particle sources are also called injectors and are used to generate the desired type of particles. The electrons are generated either from a heated cathode or from a photo cathode. The heated cathode, also called a thermionic gun, is covered on

the surface by specific alkali oxides with a low work function to emit electrons at technically practical temperatures. A small fraction of the electrons will achieve energies high enough to overcome the potential step that is necessary to leave the metal. Once outside the metal, they can be pulled away further by the application of strong electric fields. This method usually leads to high currents. But because the area where the particles leave the metal is large and they do so with a variety of different momenta, the emittances are usually rather large [38].
The electrons can be produced also by sending a strong laser pulse to the surface of a photo cathode. If the cathode is inserted directly into an accelerating RF field, the system is called an RF gun.

The positrons are created by sending a high energy electron beam to a target where photons are generated via bremsstrahlung and then converted into e^+e^- pairs.

3.2 Acceleration of the Beam

The energy of a beam created by the source is almost never sufficient for the purpose it is to be used for. Electromagnetic fields (described by Maxwell's equations) are used for acceleration, for which the Lorentz force is used to describe particle dynamics under the influence of these fields:

$$\vec{F} = q\vec{E} + \frac{q}{c}(\vec{v} \times \vec{B}) \tag{3.1}$$

Since $\vec{v} \times \vec{B}$ is perpendicular to the velocity $\vec{v}$, it is apparent that constant magnetic fields cannot be used for purposes of acceleration which requires forces in the direction of the particle. Thus any acceleration has to be provided by electric fields while magnetic fields are used only for bending the particles' trajectory [38].

3.2.1 RF Field

TESLA cavities (which are similar in principle to the cavities used in almost all particle accelerators) are standing wave structures, so particles see a time varying electric field expressed by the following relation [12]:

$$E_z \;=\; E_0\, sin(kz + \phi)\, sin(kz) \tag{3.2}$$

Large field strengths can be obtained by using RF oscillating electric fields, where only one half of the cycle can be used for acceleration. If particles enter continuously in an accelerating structure, obviously a fraction of these particles will see the axial field E_z at the wrong time (or wrong phase) due to the sinusoidal time variation. A particle P which arrives in a structure in advance as compared to M1 (figure 3.1), will get less energy and its velocity increase will be smaller so that it will take more time to travel through the structure. A particle P' will get more energy and will reduce its delay time as compared to M1. Points M1, M2 are stable points for the acceleration since particles slightly away from them will experience forces that will reduce their deviation. Points N1, N2 are unstable points in the sense that particles slightly away from them will shift even more in the structures [39]. Particles that arrive much later can receive a negative acceleration and can be forced back into the bunch behind. For this reason, the length of the accelerating structure is chosen in

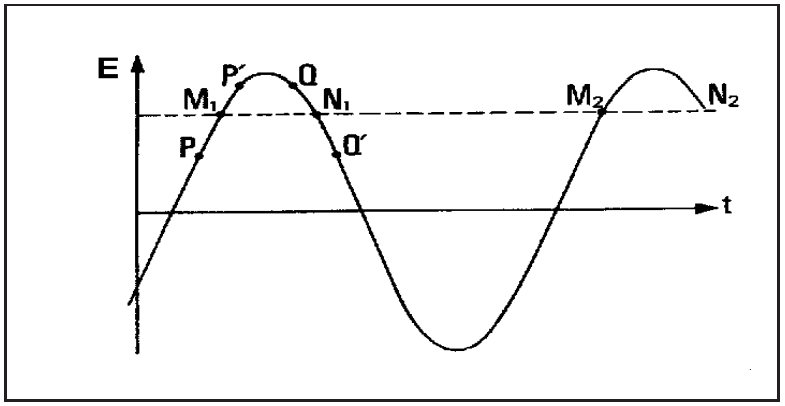

Figure 3.1: Particle phases relative to the RF field (adapted from [39]).

such a way that the time the particles require to fly through them is less than one half of the RF period, so that the particles never "see" an electric field of the wrong sign.

In order to maintain acceleration of all particles, it is important that the particles are injected into the linac with the right phase and no particles should enter during the time the field points in opposite direction. The incoming beam therefore has to consist of a uniformly arranged sequence of bunches produced in a buncher. This is an RF structure which accelerates the particles of a continuous beam differently depending on the time at which the particles enter. Here early particles within a bunch are decelerated and late particles accelerated [38] (figure 3.2).

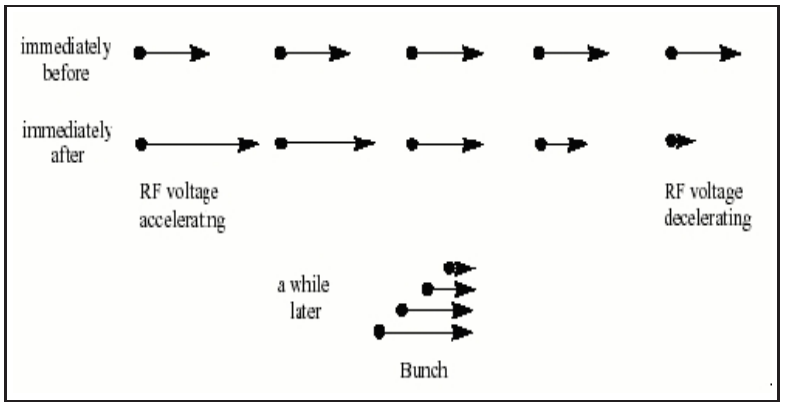

Figure 3.2: Schematic of a buncher (adapted from [38]).

3.2.2 Cavity Parameters

The next important concepts to summarize are the cavity parameters. One cavity parameter is the shunt impedance per unit length (r_s) which represents the power needed to feed a structure to maintain a specified field. Ideally, the shunt impedance must be made as high as possible to reduce the amount of power needed to maintain the field [12]. Mathematically, the power loss per unit meter in a structure is:

$$\frac{dP}{dz} = -\frac{E_z^2}{r_s} - i_b E_z \tag{3.3}$$

where i_b is the peak beam current. The first term of the right hand side of this equation represents the power lost to the cavity walls and the second term is the power removed by the beam (beam loading). While for warm (conventional) RF the wall power dominates, for superconducting RF the beam loading term dominates almost completely. This has two important consequences. Firstly, since all the power goes into the beam, a long RF pulse can be used with many bunches, 2820 for TESLA, corresponding to a large bunch separation of 337 ns. On these time scales, fast feedback can be used to adjust the cavity voltage during the pulse itself. Secondly, since $r_s \sim f^{1/2}$ for normal conducting cavities, RF must be pushed to higher frequencies while for superconducting cavities $r_s \sim f^{-1}$ and lower frequencies are more efficient (see Table 1.3) [12].

Another important parameter is the Q of the cavity defined as the ratio of stored energy in the cavity to power lost in the walls. If w_s is the stored energy per unit length of a structure, then Q is expressed as in equation 3.4. The quantity r_s/Q is independent of the geometry of the structure and of material and surface properties.

$$Q = -\frac{w\, w_s}{dP/dz} \tag{3.4}$$

Finally, the filling time t_f represents the time necessary for the cavity to reach the required voltage.

$$t_f = \frac{2Q}{w} \tag{3.5}$$

For a standing wave cavity, the filling time is defined as the time for the field to charge up to $1/e$ of its final value [12].

3.3 Transport of the Beam

Having described the method of acceleration and presented the most important cavity parameters, this brief review is now focused on the transport of the bunch

from an initial point to a final one along a collection of bending and focusing magnets called a lattice.

3.3.1 The Phase Space Variables

At the most basic level, it will have been made clear by the previous discussion that an insight into the physical significance of parameters which characterize the particle bunch will be of great help. A bunch can be visualised as composed of a large number of particles which follow closely a predescribed path along a desired beam transport line called the ideal orbit. Because all particles are close together, it is often useful to pick one that is somewhere "in the middle", and describe the motion relative to this so-called reference or ideal particle. This is very useful when dealing with simulation codes as will be shown in the next chapter.

Because the beam of particles enters the machine as a bundle of trajectories spread about the ideal orbit, at any instant a particle may be displaced horizontally by x and vertically by y from the reference particle and may also have divergence angles horizontally and vertically with respect to the central orbit: $x' = dx/ds$, $y' = dy/ds$. Throughout this thesis, the convention maintained is that the $\vec{s}$-coordinate axis points in the direction of particle movement. The vector $\vec{s}$ is used for the coordinate along the path in contrast to $\vec{z}$ in the fixed coordinate system [11]. Therefore, the particles within a bunch are specified by the coordinates $(x, x', y, y', z, \delta)$; z represents the longitudinal position of a particle relative to the beam centre (for relativistic particles $z \approx ct$) and $\delta = (p - p_0)/p_0 = (E - E_0)/E_0$, where p_0 and E_0 are the designed momentum and designed energy (figure 3.3).

One can plot a point for each pair (x, x') or (y, y') on a phase-space diagram. To first order one can choose an ellipse around the particles and the area of this ellipse is a measure of how much the particle departs from the ideal trajectory which in the diagram is represented by the origin (figure 3.4). The area of the ellipse is

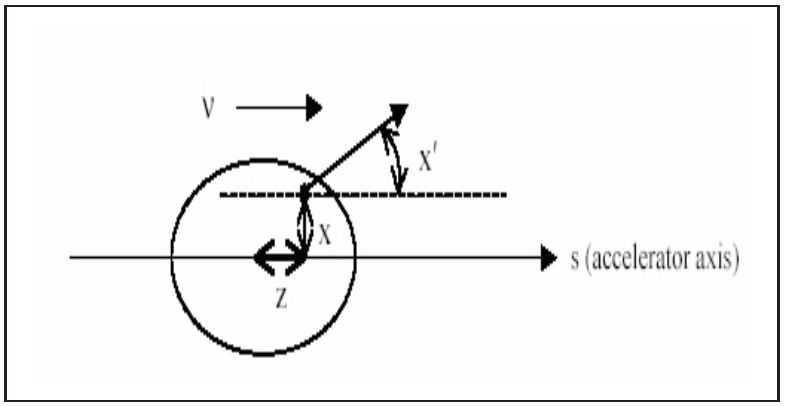

Figure 3.3: Phase space variables which characterize particles in a bunch (adapted from [41]).

called the emittance as was mentioned in chapter 2, and is usually quoted in mm mrad [44]. According to Liouville's theorem [11], under the influence of conservative forces the density of the particles in phase space stays constant. This is true for a system of particles for which the motion in time can be described by Hamiltonian dynamics (ie. no acceleration or damping or other dissipative effects such as space charge). Describing analytically an ellipse in phase space is of great help, as there is a large number of particles in a bunch and it would be impractical to calculate the trajectory for each of them. It is the aim of the following sections to show how these considerations lead directly to a simplified mathematical method.

3.3.2 The Equations of Motion

As the particles move in the accelerator, they must be kept focussed towards the ideal path by focussing devices. The oscillations performed are called betatron oscillations and they exist in both horizontal and vertical plane. To first order the equation of motion is called Hill's equation and assuming no coupling between horizontal and vertical motion it has the following form [44]:

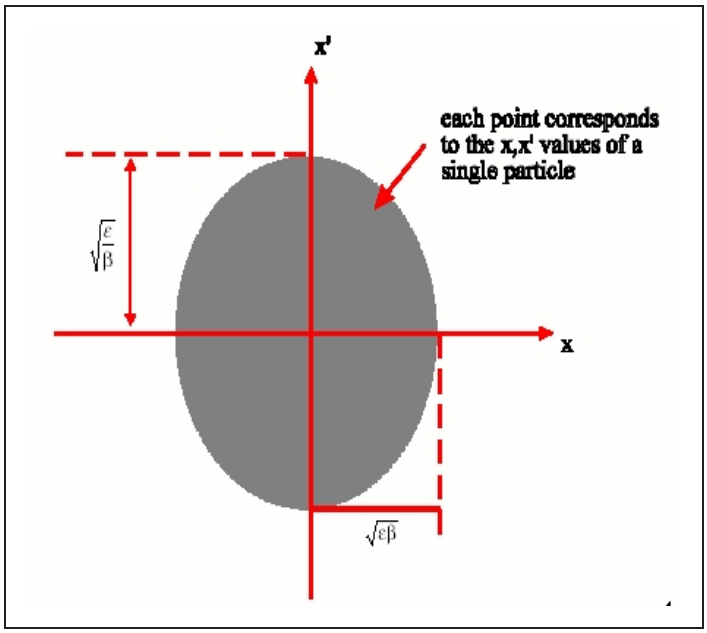

Figure 3.4: Transverse phase space plot for a large number of particles. (adapted from [42]).

$$\frac{d^2x}{ds^2} + \left[\frac{1}{\rho(s)^2} - k(s)\right] x = 0 \tag{3.6}$$

$$\frac{d^2y}{ds^2} + k(s)y = 0 \tag{3.7}$$

where $k(s)$ is a coefficient with the period L which describes the variation of the focusing strength along the orbit, $k(s) = k(s+L)$, and ρ is the radius of the curved path. One can see that the restoring force being periodic, the betatron oscillations are intuitively understood as examples of simple harmonic motion. For periodic $k(s)$ the solutions to Hill's equation have the form [44]:

$$x = \sqrt{\beta(s)\,\epsilon}\, cos[\phi(s) + \phi(0)] \tag{3.8}$$

$$x' = -\sqrt{\frac{\epsilon}{\beta(s)}}\, \sin[\phi(s) + \phi(0)] + \left[\frac{\beta'(s)}{2}\right] \sqrt{\frac{\epsilon}{\beta(s)}} \cos[\phi(s) + \phi(0)] \tag{3.9}$$

Similar solutions to the ones above are obtained in the vertical plane. The quantity $\beta(s)$ represents the amplitude modulation of the beam motion and $\phi(s)$ the phase advance that describes a change in β phase. Wilson [44] shows that if one looks at this function where β' is zero and hence where the second term in the divergence equation is zero, one may find an ellipse with semi-axis $\sqrt{\beta(s)\epsilon}$ in the x-direction and $\sqrt{\frac{\epsilon}{\beta(s)}}$ in the x' direction (figure 3.4). Its area is $\pi\epsilon$, where ϵ is an invariant of the motion for a single particle or the emittance of a beam of many particles.

If one eliminates the phase diference in the previous two equations, and define two other parameters $\alpha(s) = \beta'/2$ and $\gamma = (1 + \alpha^2)/\beta$ one can obtain a constant of motion which is called the Courant-Snyder invariant:

$$\gamma(s)\, x(s)^2 + 2\alpha(s)\, x(s)x(s)' + \beta(s)\, x'(s)^2 = \epsilon \tag{3.10}$$

The functions $\alpha(s)$, $\beta(s)$ and $\gamma(s)$ are called Twiss parameters. This invariant expression is equal to the equation of an ellipse with the area $\pi\epsilon$. The physical interpretation of this invariant is that of a single particle trajectory in phase space along the contour of an ellipse with parameters $\alpha(s)$, $\beta(s)$ and $\gamma(s)$. Since these parameters are functions of s, the form of the ellipse is changing constantly but due to Liouville's theorem, any particle starting on that ellipse will stay on it. Therefore, the choice of an ellipse to describe the evolution of a beam in phase space is thereby a mathematical convenience. One may now select a single particle to define a phase ellipse, knowing that all particles with smaller betatron oscillation amplitudes will stay within that ellipse. The description of the ensemble of all particles within a beam is thereby reduced to that of a single particle [11].

3.3.3 Dispersion

But the particle beams are not monochromatic, they have a finite spread of energies about the nominal energy. The chromatic error ΔE causes variations in the deflection of the particle trajectories and therefore a particle with a relative energy deviation δ from the ideal momentum P_0 has an offset trajectory. The offset of the reference trajectory from the ideal path represents the dispersion [11]. The displaced equilibrium orbit for momentum $p = p_0 + \Delta p$ can be given in terms of the momentum dispersion function D [10]:

$$x(s) = D(p, s)\frac{\Delta p}{p} \tag{3.11}$$

$D(p, s)$ satisfies an inhomogeneous Hill's equation [44]:

$$\frac{d^2x}{ds^2} + k(s) = -\frac{1}{\rho}\frac{\Delta p}{p} \tag{3.12}$$

where $\rho(s)$ is the local curvature in a dipole bending magnet.

3.3.4 The Magnets

During acceleration, the beam must be transported through a long straight accelerator section of few kilometers and keeping the particle motion bounded within a suitable volume of phase space such that the beam does not become unreasonably large is not an easy task. The method adopted is to use various types of magnets placed at regular intervals along the accelerator; the guidance of the charged particle is done with magnetic fields, which deflect particles as determined by the Lorentz force (equation 3.1).

The simplest type of magnet is the dipole, characterised by a length L and a constant field B, perpendicular to the beam trajectory. A dipole is used to bend the trajectory of charged particles and its working principle is demonstrated graphically in figure 3.5. One may see from the geometry that:

$$sin\frac{\theta}{2} = \frac{L}{2\rho} = \frac{LB}{2B\rho} \tag{3.13}$$

where the quantity $B\rho$ is called the magnetic rigidity and has a value of $B\rho \simeq 3.3356 \cdot p$ in units TM if p is in GeV/c [42]. There also exist sector magnets which are curved such that the beam enters and leaves magnet at 90° to pole faces.

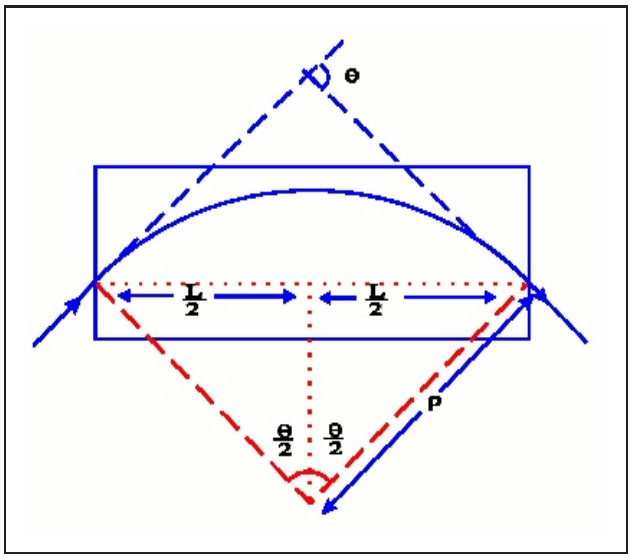

Figure 3.5: Effect of a uniform dipole field of length L and field B (adapted from [42]).

Because the beam has a tendency to spread out due to an inherent beam divergence, in order to keep the particles together, focusing devices are required. The focusing elements are quadrupole magnets having, as their name suggests, four poles (two North and two South) arranged symmetrically around the beam (figures 3.6 and 3.7). The field is zero on the axis but its strength rises linearly with distance from the axis. The strength of the quadrupole is characterized by its gradient $k = (1/B\rho)dB_y/dx$

expressed in units (TM^{-1}). Therefore a particle which deviates from the central axis of the quadrupole in the horizontal plane, is deflected back towards the centre of the magnet. This is a focusing quadrupole (QF), which focuses horizontally but defocuses vertically. If one rotates the poles by 90° it would become a defocusing quadrupole (QD) which focuses in the vertical plane but defocuses in the horizontal plane.

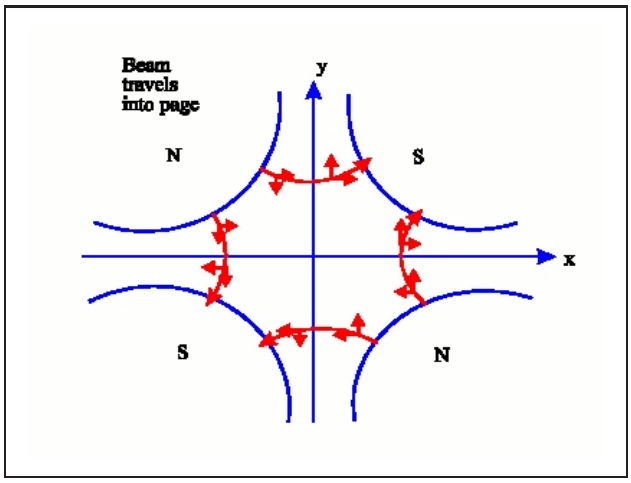

Figure 3.6: Magnetic field in a quadrupole magnet (adapted from [42]).

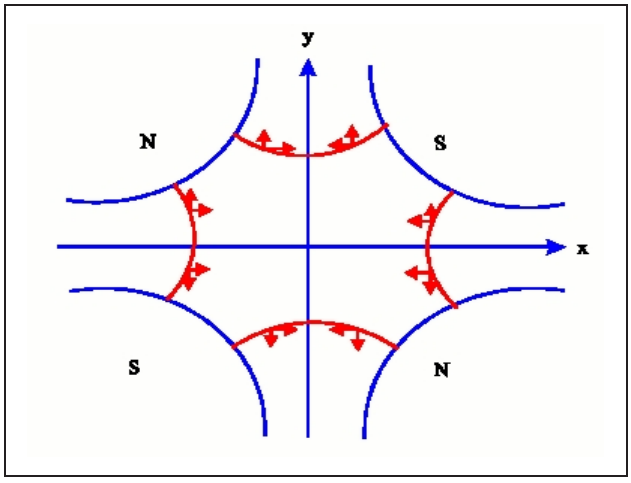

Figure 3.7: Force on a particle moving through a quadrupole magnet (adapted from [42]).

The behaviour of the quadrupoles can be studied by considering them as "thin lenses" and the beam as a diverging light beam. The envelope of the particles oscillations follows the function $\beta(s)$ which typically has a waist near a QD and a maximum at the centre of a QF (figure 3.8). Since quadrupoles focus in one plane but defocus in the other plane, the two functions $\beta_h(s)$ and $\beta_v(s)$ will have changing values in the lattice. The beam envelope contains all the particle trajectories and therefore defines the transverse size of the beam: $E(s) = \pm\sqrt{\epsilon\beta(s)}$, where the two signs indicate that there is an envelope an either side of the beam centre.

Other types of magnets used in particle accelerators are sextupoles and octupoles; higher order multipoles are rarely used. Sextupole magnets are used to compensate the chromatic abberation in strongly focusing magnetic structures and octupole magnets are used for field correction.

3.3.5 Transport Matrices

Knowledge of the area occupied by particles in phase space at the begining of a beam transport line is used to determine the location and distribution of the beam at any other place along the transport line without having to calculate the trajectory of every individual particle. The method used for beam transfer in optical elements is based on a matrix formalism because matrices are particularly helpful when dealing with systems with a large number of different elements. The effects on particles of a single element and combination of elements are described by the rules of matrix algebra and they are covered in many standard texts, ie. [11], [42] [44], [45]. Each individual component, drift space, quadrupole, dipole etc has its own associated transfer matrix, which can be used because real magnetic elements can be well described in these terms. The following examples illustrate how the matrices for various elements are derived [38]. In each transverse plane the relation between the angle of the ray and the divergence of the trajectory is $\theta = tan^{-1}(x')$ [44].

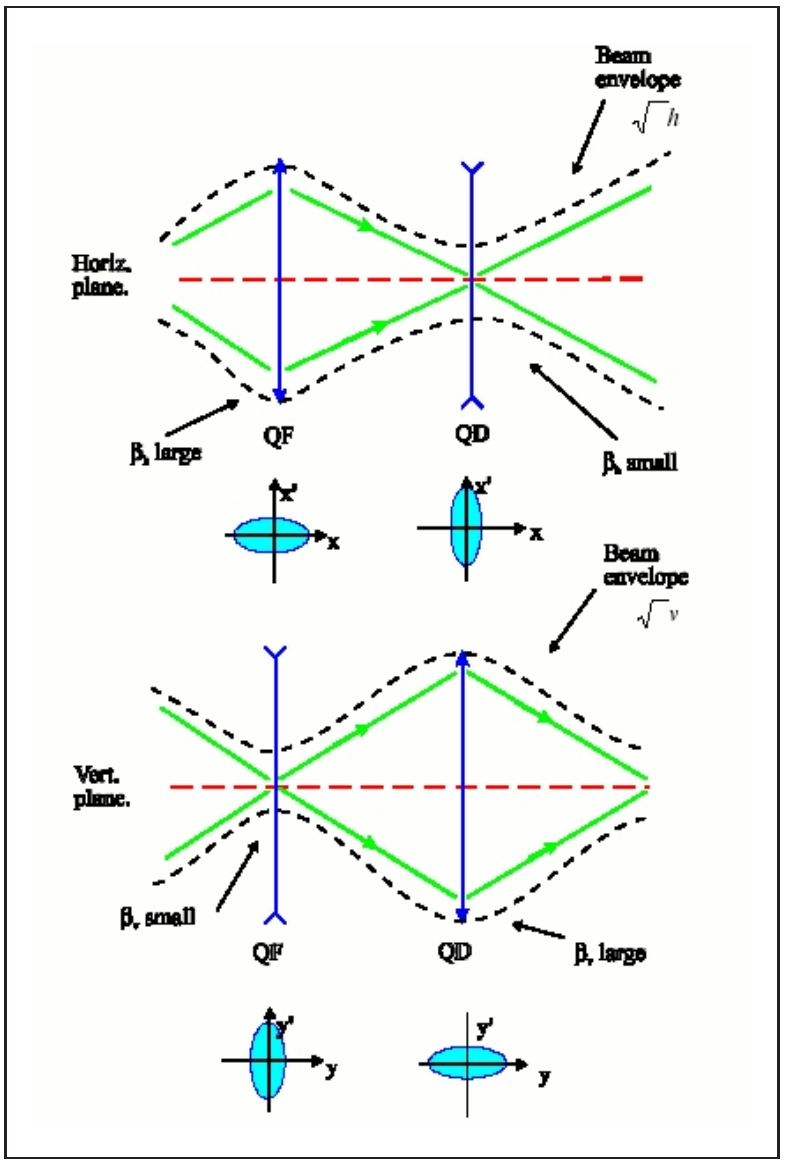

Figure 3.8: Beam envelope variation passing through a pair of quadrupoles (adapted from [42]).

The simplest case is the drift space of length l, a field free region where the angle of trajectory does not change. If the initial position of the ray is x_1 and the slope is m_1, the final values will be (figure 3.9):

$$x_2 = x_1 + ml$$
$$m_2 = m_1$$

Replacing the slope $m_{1,2}$ with divergence of the particle trajectory $x'_{1,2}$, the matrix associated with translation in field free space along the z axis is:

$$\begin{pmatrix} x_2 \\ x'_2 \end{pmatrix} = \begin{pmatrix} 1 & l \\ 0 & 1 \end{pmatrix} \begin{pmatrix} x_1 \\ x'_1 \end{pmatrix} \tag{3.14}$$

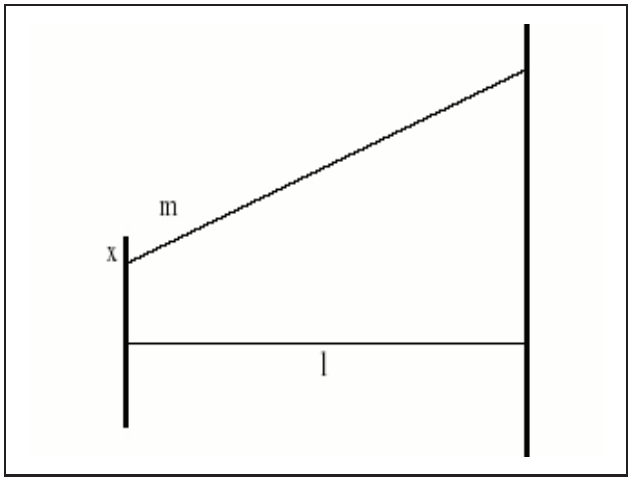

Figure 3.9: Rays passing through a drift space (adapted from [38]).

Therefore, the matrix associated with the drift is given below. A similar matrix can be obtained in the vertical plane.

$$\begin{pmatrix} 1 & l \\ 0 & 1 \end{pmatrix} \tag{3.15}$$

Another simple case is the quadrupole where only the angle of the trajectory changes when the particle passes through the magnet. Because in some cases it is desirable to calculate the approximate properties of a set of elements, the thin lens approximation is used here for quadrupoles, where we assume that the length of a quadrupole magnet is small compared to its focal length. Figure 3.10 shows the analogy between a focusing quadrupole and a converging lens of focal distance f.

$$x_2 = x_1$$
$$p = f \cdot m$$
$$x_1 + m_2 f = p$$

The transformation of orbit variables can be written in the matrix form as in equation 3.16. Therefore, the transformation matrix for a focusing quadrupole is 3.17.

$$\begin{pmatrix} x_2 \\ x_2' \end{pmatrix} = \begin{pmatrix} 1 & 0 \\ -\frac{1}{f} & 1 \end{pmatrix} \begin{pmatrix} x_1 \\ x_1' \end{pmatrix} \tag{3.16}$$

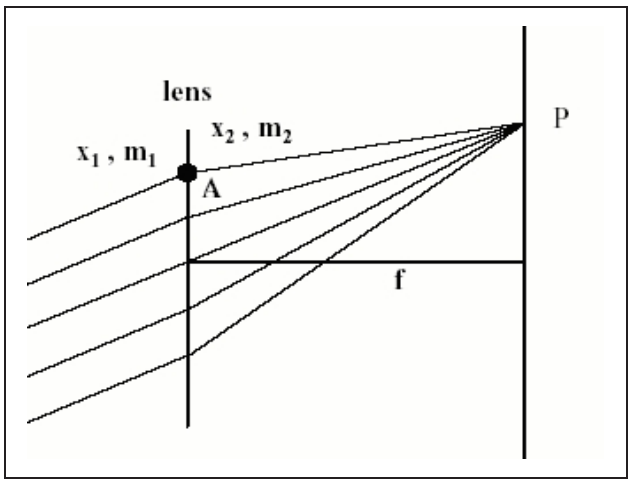

Figure 3.10: Rays passing through a converging lens (adapted from [38]).

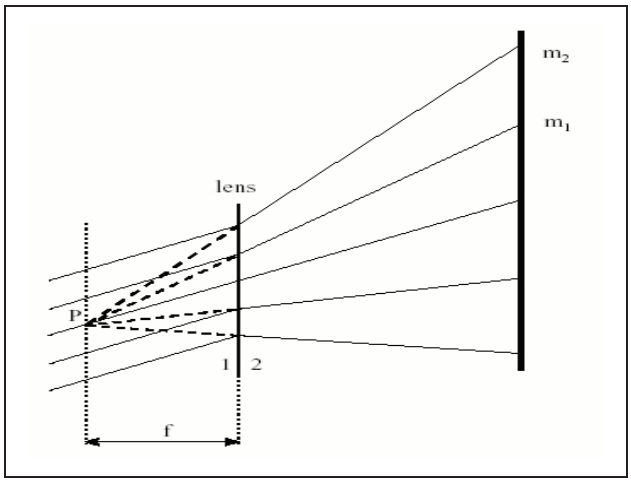

Figure 3.11: Optics ray passing through a diverging lens (adapted from [38]).

$$\begin{pmatrix} 1 & 0 \\ -\frac{1}{f} & 1 \end{pmatrix} \tag{3.17}$$

The matrix for a defocusing quadrupole is the same except for the term a_{21} which equals $+1/f$. A similar exercise to the one above shows that the transformation of the variables for a diverging lens is (figure 3.11):

$$\begin{aligned} x_2 &= x_1 \\ p &= -f \cdot m_1 \\ p &= x_2 - f \cdot m_2 \end{aligned}$$

$$\begin{pmatrix} x_2 \\ x_2' \end{pmatrix} = \begin{pmatrix} 1 & 0 \\ \frac{1}{f} & 1 \end{pmatrix} \begin{pmatrix} x_1 \\ x_1' \end{pmatrix} \tag{3.18}$$

The transformation matrix for a defocusing quadrupole is then:

$$\begin{pmatrix} 1 & 0 \\ \frac{1}{f} & 1 \end{pmatrix} \tag{3.19}$$

It is worth mentioning that a quadrupole which focuses in the horizontal plane defocuses in the vertical plane and vice versa.

The transformation matrices are useful tools in following a bunch of particles through the lattice. The arbitrary sequence of elements in a beam line can be represented by a series of transformation matrices M_i. The transformation matrix for the whole beam line is just equal to the product of the individual matrices in the reverse order encountered by the bunch.

$$M = M_n ... M_3 M_2 M_1 \tag{3.20}$$

Since, especially on computers, it is very simple to multiply matrices, this is the method of choice for the basic design of optical elements.

3.3.6 Linear Transformations in Six-Dimensional Phase Space

The particle motion can be analysed in one phase plane (x, x') or (y, y') at a time as was shown previously. But when designing a real accelerator, one needs to keep track of the motion in the entire six-dimensional phase space at once. Therefore, the 2×2 matrices are replaced by a 6×6 matrix $R(s, s_0)$, called the transport matrix, which transforms the vector $\bar{\mathrm{X}}$ from one position in the beamline, s_0, to another s. The equation of this transformation is [46]:

$$\vec{X}(s) \equiv R(s, s_0) \cdot \vec{X(s_0)} \tag{3.21}$$

where the vector $\bar{\mathrm{X}}$ has the components $\bar{\mathrm{X}} = (x, x', y, y', ct, dp)$ and the matrix $R(s, s_0)$ can be written as:

$$R(s,s_0) = \begin{pmatrix} \frac{\partial x_f}{\partial x_i} & \frac{\partial x_f}{\partial x'_i} & \frac{\partial x_f}{\partial y_i} & \frac{\partial x_f}{\partial y'_i} & \frac{\partial x_f}{\partial (ct)_i} & \frac{\partial x_f}{\partial (dp)_i} \\ \frac{\partial x'_f}{\partial x_i} & \frac{\partial x'_f}{\partial x'_i} & \frac{\partial x'_f}{\partial y_i} & \frac{\partial x'_f}{\partial y'_i} & \frac{\partial x'_f}{\partial (ct)_i} & \frac{\partial x'_f}{\partial (dp)_i} \\ \frac{\partial y_f}{\partial x_i} & \frac{\partial y_f}{\partial x'_i} & \frac{\partial y_f}{\partial y_i} & \frac{\partial y_f}{\partial y'_i} & \frac{\partial y_f}{\partial (ct)_i} & \frac{\partial y_f}{\partial (dp)_i} \\ \frac{\partial y'_f}{\partial x_i} & \frac{\partial y'_f}{\partial x'_i} & \frac{\partial y'_f}{\partial y_i} & \frac{\partial y'_f}{\partial y'_i} & \frac{\partial y'_f}{\partial (ct)_i} & \frac{\partial y'_f}{\partial (dp)_i} \\ \frac{\partial (ct)_f}{\partial x_i} & \frac{\partial (ct)_f}{\partial x'_i} & \frac{\partial (ct)_f}{\partial y_i} & \frac{\partial (ct)_f}{\partial y'_i} & \frac{\partial (ct)_f}{\partial (ct)_i} & \frac{\partial (ct)_f}{\partial (dp)_i} \\ \frac{\partial (dp)_f}{\partial x_i} & \frac{\partial (dp)_f}{\partial x'_i} & \frac{\partial (dp)_f}{\partial y_i} & \frac{\partial (dp)_f}{\partial y'_i} & \frac{\partial (dp)_f}{\partial (ct)_i} & \frac{\partial (dp)_f}{\partial (dp)_i} \end{pmatrix} \tag{3.22}$$

The subscript i indicates the initial value of the vector element at s_0 and the subscript f indicates its final value at s. One may identify the components of $R(s, s_0)$: the upper left diagonal 2×2 block in $R(s, s_0)$ is the horizontal betatron transformation matrix, the middle diagonal 2×2 block is the vertical betatron transformation matrix etc.

The 6×6 transport matrix transformation of the vector $\bar{\mathrm{X}}$ is used in many computer codes and the next chapter will describe how the magnets are "built" in a computer code and how the tracking mechanism is performed for a bunch in a given lattice.

Chapter 4

The Software

4.1 Object Oriented Programming

Large computer programs can become extremely complicated and because of their complexity, few programmers are able to comprehend a program of more than a few hundred statements in length. More than that, the programs contain errors and debugging software errors is not a trivial undertaking. Therefore, during the last decade, programmers have been trying to solve the problem by creating something that is clearer, more reliable and more easy to work with: object oriented programming (OOP) [1]. OOP represents a method of designing and implementing software systems and programming languages which provide a platform to support OOP are C++ and Java. The fundamental idea behind OOP is partitioning the program into a set of *classes* which are a description of a number of similar objects. Probably the most benefit of OOP comes from the close correspondence between the real-world things being modelled by the program and the units of classes, called *objects*. In computer language, one could say that both *data* (associated to attributes of real-world things) and *functions* (associated to behaviour) are combined in a single unit. The idea of classes leads to idea of *inheritance* where some classes are derived from others. The principle of this division is that each subclass shares common characteristics and therefore *derived classes* inherit some characteristics from their *base*

[1] For references see [47], [48], [49], [50].

classes, but add new ones of their own.
Two important benefits of OOP must be mentioned here. The first feature is *reusability*, which means that once a class has been written, created and debugged, it can be distributed to other programmers for use in their own programs. The other feature is *extensibility* because by creating new classes, the capabilities of the language are extended.

Object oriented programming was arguably the most dramatic innovation in software development of the last decade [50]. Applied soon in many fields of science due to its exciting new approach, it has not been long until accelerator physics took advantage of this complex and powerful methodology. A C++ based simulation code called "MERLIN" [51] was developed at DESY by Nick Walker and used to model the beam dynamics issues related to the beam delivery system of the TESLA linear collider.

4.2 The Simulation Code

It is worth specifying from the begining that "MERLIN" is not an accelerator design tool: there is no optics fitting currently implemented which could be used to design lattices. Originally designed to study ground motion effects in BDS, it has now been extended to model other effects related to this linear collider component. It is continually being improved, new features being added as needed. New versions are released from time to time as "MERLIN" has become a general tool applicable to many accelerator problems. Some of the characteristic features are:

- support for all the common standard components found in an accelerator;
- full three-dimensional geometry including alignment errors;
- physics (tracking) is six-dimensional (see chapter 3);
- full support for field, alignment and diagnostics errors;

- allows modeling of orbit feedback systems;
- dynamic alignment errors, such as ground motion are directly supported.

"MERLIN" does not include collective effects, wakefield effects and Coulomb scattering through materials. It supports construction of accelerator lattice models and beam tracking. It models only the e^- BDS although for the original studies it modelled both the e^- and the e^+ beam delivery systems, colliding the beams at the IP. This took a factor of two more time and does not actually change the results [67] .

The current release of "MERLIN" is the third attempt at producing a generic class library for particle accelerator simulations [51]. The library contains over 230 classes and it can be divided into two sections: the accelerator model description and the beam dynamics simulation (the various tracking algorithms used to model the beam dynamics). This separation allows the same accelerator model to be used repeatedly for different forms of beam dynamics simulations, without the need to modify the accelerator model code directly. Currently, the only beam dynamics package supported is particle tracking [51]. But before going into detail with various tracking tasks, a description of how an accelerator model is constructed from a prototype lattice described separately in an optics file is needed at this stage.

4.2.1 Construction of the Accelerator Model

The accelerator model can be thought of as a pure representation of the physical accelerator, each component containing a description of its physical attributes (geometry, aperture, field). During a tracking operation, the beam described at some initial point in the lattice is tracked sequentially through each component until it reaches the last one. Therefore, at the first element there is a specification of the phase space region occupied by the beam and as it passes each component, the properties of the beam are calculated in the the local frame of each component.

A) The Lattice

The lattice is described separately in an optics file which is read by the code. The optics file used for constructing the accelerator model is "*tesla_bds_8.05.optics*" [52]. Created with the MAD program (Methodical Accelerator Design) [53], the lattice described in this file is a series of accelerator components which reflect the real machine. Most of these components share a few attributes: the identifier, the position in the lattice, the length, the associated field (if any), the aperture.
The identifier is a simple string which specifies the label which the constructed component in the accelerator model will have. The elements are coded as folows:

- 1st letter: D, B, Q, S, K for Drift, Bend (Sector Bend), Quadrupole, Sextupole, Kicker;
- 2nd letter: the code letter of the section it belongs to (ie. L for Linac to Collimation, C for Collimation and Diagnostics, F for Final Focus System, E for Extraction System);
- 3rd letter: S for Skew Elements only;
- 3rd to 5th letter, if any : any number 0-9 or letter A-Z to differentiate elements of the same type in the same section.

There are a few exceptions: ESPOI and XYSPOI (spoilers in the collimation section), COLX and COLY (spoilers in the chromatic correction section), BPM (beam position monitors).
The length is the physical length of the component.
The field strengths are in $MKSA$ units and are labeled K0L for Sector Bends, K1L for Quadrupoles, K2L for Sextupoles, K3L for Octupoles, where K1L$\equiv k(s)$, etc. The bending angles in dipoles are expressed in radians.
The aperture is the cross section of the vacuum pipe or other collimating aperture. Since MAD does not support aperture definitions in magnets, the apertures are indicated by the TYPE property attached to each element:

- TYPE = D20 : denotes circular aperture of 20 mm diameter;

- TYPE = X10Y40 : denotes rectangular aperture of 10 mm horizontal width and 40 mm vertical height.

The component types are [53]:

Drift

A **Drift** represents a section free of electromagnetic field. It has rectangular geometry and is generally used to specify the distance between accelerator components in the lattice. It is specified by its identifier and characterized by its position s and by its length.

Marker

A **Marker** does not represent a physical accelerator component, but is used to mark a specific position in the lattice. It can be thought of as zero-length drift and has no field or geometry associated with it.

Monitor

A **Monitor** represents any diagnostic which is typically found in an accelerator. There are beam position monitors **BPM** which record the beam position for closed orbit corrections.

SectorBend

A **SectorBend** is a representation of a sector bend magnet. By default, the magnet is hard edged (this is an approximation which states that the magnetic strength is constant within the magnet and drops to zero immediately outside the dipole; in real magnets the field strength does not change suddenly from zero to full value but rather follows a smooth transition from zero to the maximum field [11]). However, in most situations the hard-edged model is adequate.

Quadrupole

A **Quadrupole** represents a hard-edge quadrupole magnet. It has a rectangular geometry and a quadrupole coefficient K1L = $(1/B\rho)(\partial B_y/\partial x)$ in m^{-2}. A positive quadrupole strength implies horizontal focussing of positively charged particles.

Sextupole

A **Sextupole** represents a hard-edge sextupole magnet. It has a rectangular geometry and a sextupole coefficient K2L = $(1/B\rho)(\partial^2 B_y/\partial x^2)$ in m^{-3}.

Octupole

An **Octupole** represents a hard-edge octupole magnet. It has a rectangular geometry and an octupole coefficient K3L = $(1/B\rho)(\partial^3 B_y/\partial x^3)$ in m^{-4}.

All magnets are normally considered aligned on the ideal path. A particle following this trajectory through a magnet experiences a uniform field which begins and ends abruptly at the entrance and exit faces of the magnet.

B) The AcceleratorModel Class

Having given this description of the components of the BDS lattice, it is instructive to return to the simulation code to see how these elements and their corresponding parameters are read by the program.
The accelerator model (class **AcceleratorModel**) is constructed from model elements and table 4.1 shows the correspondence between the lattice elements and their classes in the simulation code. In the case of class **RectMultipole** the program makes the difference between quadrupoles, sextupoles and octupoles by looking at the n-th field derivative (in T/m^n where n is the number of poles) evaluated at radius $r = 0$.
The parameters of the lattice elements are read by the code using other three classes: class **Aperture** for apertures, class **EMField** for the electromagnetic field and class

lattice element	class
Drift	class **Drift**
Marker	class **Marker**
Monitor	class **Monitor**
Sector Bend	class **SectorBend**
Quadrupoles, Sextupoles, Octupoles	class **RectMultipole**

Table 4.1: The corresponding class of each component described in the BDS lattice.

AcceleratorGeometry for geometry. Class **Aperture** provides functions which returns the radius of apertures at a location z and can specify if a point with coordinates (x, y, z) is within the aperture. Class **EMField** can return the electric and magnetic field of an element in the lattice. Class **AcceleratorGeometry** is responsible for calculating coordinate transformations to and from the local component coordinate frame during tracking operations.

Components can be considered as "stand alone" elements, in that they have their own local coordinate frame in which all their physical characteristics are defined. They know nothing about their surroundings, or where they sit in the lattice. Location of an accelerator component in a beamline is the job of a **LatticeFrame** object. **LatticeFrame** objects contain all the beamline related information for a given component and supports full 3-dimensional transformations (rotation and translation). They also form a nested-frame hierarchy, which allows a set of sub-frames to be transformed as a group (ie. allows to handle the simulation of groups of elements mounted on a common support) [51].

AcceleratorModel acts as an interface to the model because allows the user either to access the entire beamline or only a subsection of it. The following two examples illustrate these two cases.
In the first example, the function *ConstructModel()* causes the construction of an

AcceleratorModel object based on the MAD optics file for which the path is provided in the brackets. This is the case when the entire beamline is constructed. The data structure *BeamData* defines the 6-dimensional beam phase space (x, x', y, y', ct, dp), where ct is the substitute for z in the code which assumes $v \approx c$ and $dp = (p - p_0)/p_0$. The nominal energy of the beam p_0 is specified in brackets (250.0 GeV).

```
pair<AcceleratorModel*, BeamData * > mb =
ConstructModel("D:/merlin/Merlin/BeamDynamics/tesla_bds.optics",
    250.0*GeV)
```

In the second example only a subsection of the beam delivery system is constructed. The function *GetBeamline()* is called by a reference (*theModel*) to the class **Accelerator Model** and returns a beamline from the first component to the second component specified as an argument. If at least one of these elements is not found, the program throws a warning as the argument "true" is also specified in brackets. A particle bunch (in this example denoted as *bunch*0) is tracked through this line, from element "Drift.BEGL" to element "BMP.BMP7040".

```
ParticleTracker tracker
(theModel.GetBeamline("Drift.BEGL", "BMP.BMP7040"), bunch0, true)
```

The first example was used in a simulation where the beam core was tracked through the BDS to the IP. The second example was used in a simulation where a halo (see section 5.2.1) was tracked until the final doublet (the last element in the lattice having a non zero length was "BMP.BMP7040").

4.2.2 Construction of the Beam

Once the lattice is constructed, a bunch of particles must be defined to be tracked through it. In the simulation code, a *Bunch* is represented by an ensemble of particles with the specified momentum, total charge and particle array. The class

ParticleBunchConstructor is responsible for taking the beam data (supplied by the class **BeamData**) and the number of particles to generate a particle bunch. The beam data (Twiss parameters, emittance $\epsilon_{x,y}$, etc.) is supplied for defining the six-dimensional phase space and the bunch is constructed with random particles taken from this six-dimensional distribution. The form of the distribution can be either normal (gaussian) in which case the beam data is interpreted as RMS values, or flat, in which case the data specifies the $\pm$ extents for a flat (rectangular) distribution.

The example below shows the construction of a gaussian bunch core. The fragments of code discussed here are part of the function CoreLossSimulation which also constructs the accelerator model and tracks the newly constructed bunch to the IP. It will be observed that for a gaussian bunch core, the constructor of the class **ParticleBunchConstructor** takes the beam data (*beam*), the number of particles (*npart*) and the type of distribution (*normalDistribution*) and calls the function *ConstructParticleBunch()* which returns the particle bunch based on the current bunch parameter settings (*core*):

```
void CoreLossSimulation (AcceleratorModel& theModel,
const BeamData& beam0, size_t npart)
{BeamData beam = beam0;
ParticleBunch* core = ParticleBunchConstructor(beam, npart,
normalDistribution).ConstructParticleBunch();}
```

The construction of a flat halo can be done with a similar function but with the $\pm$ extents ($\pm\sigma_x$ and $\pm\sigma_y$) supplied by the main program. The type of distribution specified in the constructor of the class **ParticleBunchConstructor** must be *flatDistribution* in this case.

Within the bunch, a reference particle is defined as the particle which sits on the nominal orbit, responsible for maintaining the reference momentum and time (ct). The reference particle also represents approximately the centroid of the bunch. At any specified position in the system an arbitrary charged particle is represented by a

vector $\vec{X}$, whose components are the positions, angles and momentum of the particle with respect to the reference trajectory (x, x', y, y', ct, dp).

The centroid of the bunch can be offset with respect to its nominal position and chapter 6 will discuss in detail the causes and the consequences of an offset beam. A qualitative view of the method performed for applying an offset to the centroid of the bunch in the computer code is described as follows.
In the body of the function described previously, one may create an object (*offset*) of type phase space vector (*PSvector*). The class **PSvector** is well suited for creating such a 6-dimensional phase space vector. This object can call all the member functions of the class **PSvector** ($x(), xp(), y(), yp(), ct(), dp()$) and takes the values of the new parameters supplied by the main program $(ox, oxp, oy, oyp, oct, odp)$. Then the object *core* calls a function which sets the coordinates of the centroid to the new values:

```
PSvector offset;
offset.x() = ox;
offset.xp() = oxp;
offset.y() = oy;
offset.yp() = oyp;
offset.ct() = oct;
offset.dp() = odp;
core → SetCentroid(offset);
```

Once the offset is applied, the tracking is performed as in the usual case and the final particle distribution is output.

4.2.3 Particle Tracking

The tracking algorithm is based on the first-order matrix theory of Brown [55]. The magnets are represented to first order by a 6×6 matrix (see chapter 3) referred to as

the R matrix, which describes the action of the magnet on the particle coordinates [67]. Thus the passage of a charged particle through the system may be represented by the equation:

$$\vec{X_1} = R \cdot \vec{X_0} \tag{4.1}$$

where $\vec{X_0}$ is the initial coordinate vector and $\vec{X_1}$ is the final coordinate vector of the particle under consideration. The same transformation matrix R is used for all particles traversing a given magnet, one particle differing from another only by its initial coordinate vector $\vec{X_0}$ [54].
The first-order R matrix for a drift space with length L is:

$$\begin{pmatrix} 1 & L & 0 & 0 & 0 & 0 \\ 0 & 1 & 0 & 0 & 0 & 0 \\ 0 & 0 & 1 & L & 0 & 0 \\ 0 & 0 & 0 & 1 & 0 & 0 \\ 0 & 0 & 0 & 0 & 1 & 0 \\ 0 & 0 & 0 & 0 & 0 & 1 \end{pmatrix} \tag{4.2}$$

The first-order R quadrupole matrix is represented next. The parameters which appear are L, the effective length of the quadrupole and $K_q^2 = (B_0/a)(1/B\rho_0)$, where $B\rho_0$ is the magnetic rigidity of the trajectory. In the previous relation a is the radius of the aperture and B_0 is the field at radius a. The matrix repersentation is for a quadrupole which focuses in the horizontal plane. A vertically focusing quadrupole has the first two diagonal submatrices interchanged.

$$\begin{pmatrix} cos\, k_q L & \frac{1}{k_q} sin\, k_q L & 0 & 0 & 0 & 0 \\ -k_q\, sin\, k_q L & cos\, k_q L & 0 & 0 & 0 & 0 \\ 0 & 0 & cosh\, k_q L & \frac{1}{k_q} sin\, k_q L & 0 & 0 \\ 0 & 0 & k_q\, sin\, k_q L & cosh\, k_q L & 0 & 0 \\ 0 & 0 & 0 & 0 & 1 & 0 \\ 0 & 0 & 0 & 0 & 0 & 1 \end{pmatrix} \tag{4.3}$$

The traversing of several magnets and drift spaces is described by the same basic equations, but with R now being replaced by the product matrix of the individual matrices of the system elements [54]:

$$R(t) = R(n)...R(3) \cdot R(2) \cdot R(1) \tag{4.4}$$

This formalism may be extended to second order by the addition of a second term. The components of the final coordinate vector, are given as [67]:

$$\vec{X_i}(1) = \sum_j R_{ij} \cdot \vec{X_j}(0) + \sum_{jk} T_{ijk} \cdot \vec{X_j}(0) \cdot \vec{X_k}(0) \tag{4.5}$$

where T is the second-order transfer matrix. The T matrix is also accumulated by the program as one traverses a series of elements.

The particle tracking is performed on a sequence of components that represents the lattice and the class **TrackingSimulation** is responsible for tracking the bunch through the specified beamline. A single process which can represent any physical (ie. particle transport) or abstract mechanism (ie. output) can be applied to a *bunch* object during tracking and the class **BunchProcess** is provided for this. During transport, the process which increments the independent variable s and actually tracks through a step Δs is supported by the class **ParticleTransportProcess**. The class **ParticleBunchIntegrator** is responsible for tracking particles through

accelerator components.

An example of particle tracking is described below. The constructor of class **ParticleTracker** takes the beamline to be tracked (*theModel.GetBeamline()*) and the particle bunch (*core*). Then the function *Run()* is called, which actually runs the simulation.

```
ParticleTracker tracker(theModel.GetBeamline(),core,true);
tracker.Run();
```

4.3 The Simulation Program for Beam Offsets

The analysis described in chapter six (spoiler survivability in the case of a beam offset) was performed on the results obtained with "MERLIN". The *AcceleratorModel* was constructed using the techniques described previously and a *Bunch* was created and tracked through the lattice. Offsets in positions, angles and energy were applied to the centroid of the bunch. The particle collimation was performed at each element using the constructor of class **CollimateParticleProcess**. The particles which are outside the collimated aperture are considered lost and their vectors $\vec{X}$ are collected in *loss files* (ie. *lossummary*). The collimation process is added to the tracking by calling the function *AddProcess()*:

```
ParticleTracker tracker (theModel.GetBeamline(), core, true);
CollimateParticleProcess* collproc =
new CollimateParticleProcess(2, COLL_AT_EXIT, &lossummary);
tracker.AddProcess(collproc);
tracker.Run();
```

But before presenting the results, a full description of the collimators and their role as part of the machine protection system is given in chapter 5.

Chapter 5

Machine Protection Issues

5.1 Introduction

The Machine Protection System (MPS)[1] is one of the most serious operation issues that any future linear collider will face. The high luminosity achieved in linear colliders ($\sim 10^{34} cm^{-2} s^{-1}$) requires high beam power and density. Unfortunately, these beams will almost certainly damage any material that is intercepted unless extreme care is taken.

The purpose of the MPS is to prevent damage to the collider components in the event of a routine failure or mistake. But the system cannot provide comprehensive protection against any possible failure; the complexity of the MPS must be balanced against the cost, difficulty, and time for repair of the systems it protects.

5.1.1 Machine Protection System for TESLA

For TESLA, the complete accelerator complex and the various beam transfer and delivery lines have to be equipped with a machine protection system to prevent beam operation in case of technical failures. The machine protection system is an

[1]The TESLA Technical Design Report [19] was extensively used in this chapter.

independent alarm system. It is remotely controlled, configured and read out by the main accelerator control system. It will consist of distributed interlock modules which have digital I/O channels and interfaces to a redundant fibre-optic alarm line as well as to the main Ethernet network [19]. The structure of the machine protection system follows the structure of the TESLA complex having separate section permits for the different machine sections. It reacts to trigger events, e.g. from beam loss detectors, beam current measurements, RF systems, collimators etc.
The BDS collimators are part of the MPS and this chapter will present the main issues associated with them.

5.2 Overview of the TESLA-BDS Collimators

5.2.1 The Collimation System as Part of the MPS

The collimation system is used to remove particles with large amplitude, the so-called beam halo. Although the amount of halo expected from the main linac is insignificant ($\sim 10^4$ particles per bunch [35]), in high energy physics colliders the halo particles surrounding the core of the beams would cause intolerable background in the physics detector if not removed.

The beam halo expected at the end of the main linac is produced by three sources. The first source of beam halo is represented by the large amplitude particles escaping from the damping ring (10^{-3} particles of the total number of particles per bunch [35]). The large amplitude is due to the non-Gaussian nature of the particle distribution in the tails caused by a small number of hard scattering events. Although the pre-linac collimation system will remove most of these particles, some of them will escape in the main linac.
Beam-gas scattering was found to be another source of beam halo in the main linac.

Assuming for the helium pressure at 2 K $p = 10^{-10}$mbar, the halo population was estimated of about 10^3 particles per bunch [35].
Electrons that are field-emitted from the linac structure walls (the so-called dark current [46]) represent the last source. They can be accelerated to high energies and since they have much lower energies than the main beam, they will be over-focused by the quadrupole lattice and most of them will rapidly reach betatron amplitudes large enough to hit the cavity walls [35].

The high energy of the halo particles (close to the beam energy - 250 GeV for TESLA) requires multiple stage collimation. The collimation system consists of two types of collimators. Collimators defining the phase space acceptance for the beam are called spoilers, while collimators used to remove secondary particles produced by showering at the spoilers are called absorbers. The spoilers are placed close to the beam and used to scrape the particles off; the particles scattered by the spoilers are then collected in absorbers, placed at suitable locations downstream of the spoilers (figure 5.1). The absorbers are well within the optical shadow of the spoilers, so that the spoilers protect the absorbers from a direct hit from the beam. The reason is that whereas the spoilers are made of titanium to reduce the probability for mechanical failure in the material if the beam is incident head on, the absorbers are made of copper [59] which has a lower melting temperature.

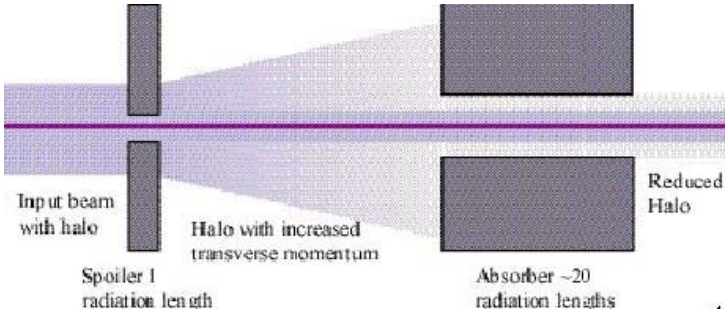

Figure 5.1: Spoiler/Absorber combination (adapted from [74]).

Since publication of the TESLA Conceptual Design Report (CDR)[58], the post-linac collimation system has undergone a major design change. The change reflects a shift in philosophy with respect to the machine protection issue: the system presented in the CDR [58] was based on the philosophy that all the collimators should withstand a direct hit from a few bunches of the bunch train. The system was characterised by very large (18 km) β-functions, and the tolerances on the magnet alignment and field quality were very tight. Unfortunately, this system was later shown not to be safe from damage from a large amplitude beam.
The philosophy reflected in the new design is to protect the momentum collimator against a fast momentum error - e.g. klystron phase errors - since such events are the most probable (and frequent) failure modes for a linear accelerator. Large amplitude betatron oscillations are by comparison rare events, and tend to be associated with magnet failures which are relatively slow (several milliseconds): a failure of a magnet could be detected by direct monitoring and the beam inhibited at the gun.

The TESLA concept has several advantages which relieve the constraints on a collimation system (Table 2.1):

- the large bunch spacing (337 ns) allows a head-on collision scheme using large aperture superconducting final doublets, which result in a relatively large required collimation depth (see section 5.2.4): $\pm 13\ \sigma_x$ and $\pm 80\ \sigma_y$;

- the long bunch train (2820 bunches) and large bunch spacing allows the majority of the beam (section 5.3.2) to be safely extracted to the beam dumps by the fast emergency extraction line in the event of some machine error or failure;

- the amount of halo expected from the superconducting linac is extremely small ($\sim 10^4$ particles per bunch [35]).

5.2.2 TESLA Collimators

In the TESLA Beam Delivery System, the collimation system is based upon a combination of a thin spoiler (1 radiation length) and a thick absorber (20 radiation lengths). The advantage of the thin spoiler is a low energy deposition in the material and therefore the possibility of accepting a large number of bunches. Only the thin spoiler is located close to beam where damage and wakefield effects are significant. The spoilers will increase the beam angular divergence so that, by the time the beam strikes another component, it will not cause any damage (figure 5.1). The thick absorber protects magnets against irradiation with low energy electrons and secondary particles emitted from spoilers.
But the extremely small beam emittances and corresponding beam sizes pose significant safety issues for the design of the mechanical spoilers: relatively large β-functions are generally required to increase the beam-sizes at the spoiler in order to reduce the peak particle density on the spoiler if it is hit by the beam.

Beam collimation is performed at two stages: the first stage in the CDS lattice, the second stage in CCS lattice.

A) Collimation at the CDS module

The design for the collimation system in CDS comprises [34]: a non-linear magnetic system upstream of the momentum collimator, called the magnetic energy spoiler and used to "blow-up" the beam size on that collimator in the event of a large energy error ($\geq$ 2%), a downstream spoiler in a dispersive system used for momentum collimation (ESPOI) and a pure betatron collimation system with four spoilers (XYSPOI).

Figure 5.2 shows how the magnetic energy spoiler works[2]: an off-momentum bunch with an error $\delta = \Delta p/p$ receives a horizontal kick ($\Delta X'_{oct}$) from the octupole at the

[2]Reference [35] was used extensively for this study.

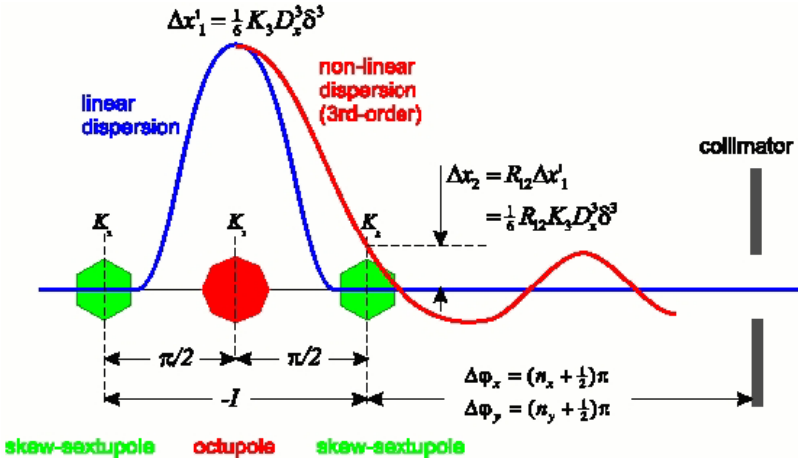

Figure 5.2: Magnetic Energy Spoiler (adapted from [19]).

high dispersion point (D_x=-100 mm):

$$\Delta X'_{oct} \approx \frac{1}{3!} K_3 D_x^3 \delta^3 \tag{5.1}$$

where K_3 is the octupole strength and D_x is the horizontal dispersion at the octupole. At the second skew-sextupole, this kick generates third-order dispersion:

$$\Delta X_{sext} \approx \frac{1}{3!} R_{12} K_3 D_x^3 \delta^3 \tag{5.2}$$

where ΔX_{sext} is the offset at the skew-sextupole and R_{12} is the linear Green function from the octupole to the skew-sextupole ($R_{12} = \sqrt{\beta_{x,oct}\beta_{x,sext}}$). The momentum-dependent offset of the beam in the skew-sextupole generates a skew-quadrupole with strength K_1:

$$\begin{aligned} K_1 &\approx K_2 \Delta X_{sext} \\ &\approx \frac{1}{3!} K_2 K_3 R_{12} D_x^3 \delta^3 \end{aligned}$$

The effective skew-quadrupole couples the horizontal emittance into the vertical plane. The result is a significant increase in the vertical beam size at the momentum spoiler. If the coupling is strong enough that the vertical divergence at the sextupole ($\sigma_{y',sext}$) is dominated by the coupling, the relative increase in vertical beam size becomes:

$$\begin{aligned}\left[\frac{\sigma_y(\delta)}{\sigma_y(0)}\right]_{spoiler} &\approx \left[\frac{\sigma'_y(\delta)}{\sigma'_y(0)}\right]_{sext} \\ &\approx K_1\frac{\sigma_{x,\,sext}}{\theta_{y,\,sext}} \\ &\approx \frac{1}{3!}R_{12}K_2K_3D_x^3\sqrt{\frac{\epsilon_x\beta_x\beta_y}{\epsilon_y}}\delta^3\end{aligned}$$

where $\epsilon_{x,y}$ represents the emittance and $\beta_{x,y}$ represents the betatron function β. At some momentum error δ_{crit}, the beam will strike a downstream vertical spoiler. The maximum beam size increase is constrained by a maximum permissible kick ΔX_{max} at the skew-sextupole:

$$\left[\frac{\sigma_y(\delta)}{\sigma_y(0)}\right]_{max} \leq \frac{1}{2}K_2\Delta X_{max}\frac{\sigma_x}{\sigma_{y'}} \tag{5.3}$$

where $\sigma_{y'}$ is the nominal design vertical beam divergence at the skew-sextupole. But the collimation depth $N_{x,y}$ can be written as:

$$N_x \geq \frac{\Delta X_{max}}{\sigma_x} \tag{5.4}$$

$$N_y \geq \frac{1}{2}\frac{K_2\Delta X_{max}^2}{\sigma_{y'}} \tag{5.5}$$

therefore equation 5.3 becomes:

$$\left[\frac{\sigma_y(\delta)}{\sigma_y(0)}\right]_{max} \leq 2N_y\frac{\sigma_x}{\Delta X_{max}} \leq 2\frac{N_y}{N_x}$$

This relation shows that the maximum achievable beam size increase before hitting a spoiler is given by the ratio of the vertical to horizontal normalised collimation apertures. The energy spoiler intercepts the beam first so the gap is set smaller than $\pm\delta_{crit}/D_{x,spoi}$ where $D_{x,spoi}$ is the linear dispersion at the energy spoiler.

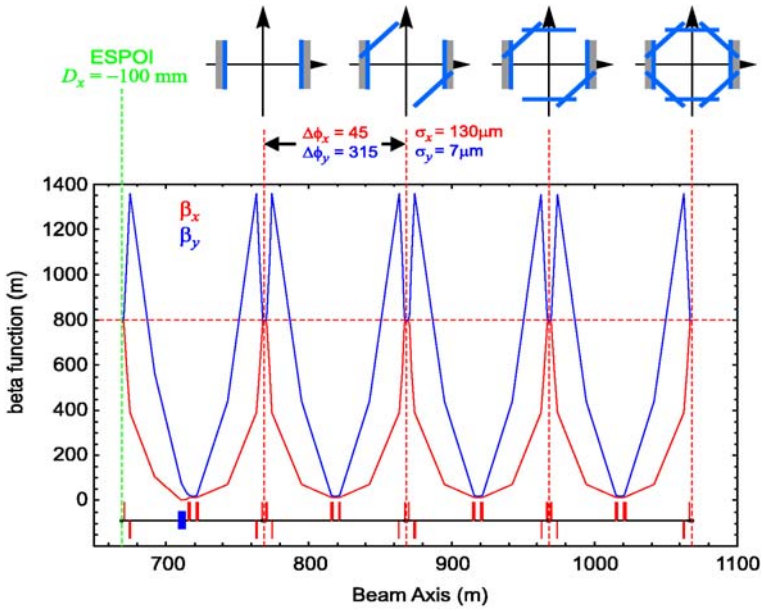

Figure 5.3: Collimation and Diagnostics System - the optics (adapted from [19]).

In order to prevent destruction of the protection spoilers in the CDS lattice, the spoilers are located in the main collimation section at the symmetry points where $\beta_x = \beta_y$=800 m, such that the beam size is large in both the horizontal and vertical plane. This is translated into a beam size of $128\times 7\,\mu$m at 250GeV. The phase advance per cell (spoiler) is $\phi_x = 45°$, $\phi_y = 315°$. Figure 5.3 shows the optics.

Because the particle beams are not monochromatic but have a finite spread of energies about their nominal energy, the first spoiler is at a high dispersion point

($D_x = -100mm$) and is used as the momentum collimator (spoiler)-ESPOI. The other four spoilers (XYSPOI) are located in a zero dispersion region, and are referred to as the betatron collimation system because they are used to collimate particles with large amplitude. They effectively define an octagon in phase space (figure 5.3). The physical apertures of the spoilers are set to a factor $\cos(45°/2)$ $\sim$0.92 smaller than the required collimation depth, which fits the octagon defined by the spoilers inside the ellipse defined by the collimation depth. Since it is the spoilers which effectively define the collimation aperture, the words collimator and spoiler will be used interchangeably in the following sections.

The exact positions of the CDS spoilers in the BDS lattice are listed in Table 5.1. These values corespond to the optics file *tesla_bds_8.05.optics*:

Spoiler	Z (m)
ESPOI	678.24
XYSPOI.1	777.88
XYSPOI.2	877.56
XYSPOI.3	977.24
XYSPOI.4	1076.92

Table 5.1: Position of the CDS spoilers in the BDS lattice (adapted from [52]) .

B) Collimation at the CCS module

The design for the collimation system in the CCS comprises a set of four betatron spoilers. This second stage of halo collimation gives safety in suppressing background from large amplitude particles which may escape from the first stage or may be produced from gas scattering between the collimation system and final focus system. The reason for this is that although the vacuum system works to maintain an average pressure of 10^{-8} mbar in beam pipes [19], there is still enough residual gas for incident particles to scatter off. It will also help to keep the detector background

at an acceptable level even at a small deviation of the beam position in the first stage of collimation [19].

Spoiler	Z (m)
COLX 1.1	1191.17
COLX 1.2	1283.17
COLY 1.1	1375.17
COLY 1.2	1467.17

Table 5.2: Position of the CCS spoilers in the BDS lattice (adapted from [52]).

The second set of spoilers is located at the high β points in the chromatic correction system and are known as CCS collimators - COLX and COLY. The positions of the CCS spoilers are listed in Table 5.2. as they are in the optics file *tesla_bds_8.05.optics*.

5.2.3 The Geometry and Material Choice

The choice of the construction and of the material of collimators are defined by the parameters of the intercepting particles and by the features of processes of their interaction with the collimator substance. The collimators are intended basically for the interception of the peripheral part of the beam. It means that they should have a rectangular aperture, when the beam is symmetric in transverse planes relative to its axis [61].

The main reasons for the choice of the materials for the spoilers are: they should withstand any thermal heating and the arising mechanical stresses should not lead to destruction of the spoilers. This is one of the greatest challenges in the design of the collimation system, although for TESLA the spoilers only need to survive two bunches, as the inter-bunch spacing is so long that the later bunches can be sent

through a bypass line directly onto the dump. The heating induces thermal stresses in the material which, if too high, will lead to cracks and damage the spoiler. The temperature limit can be estimated from the induced stresses:

$$\sigma_{UTS} \geq \frac{1}{2}\alpha\, E\, \Delta\, T_{inst} \tag{5.6}$$

where ΔT_{inst} is the instantaneous temperature rise. Here one should take into account that the material dependent parameters σ_{UTS} ultimate tensile strength, α linear expansion coefficient and E elastic modulus are also functions of temperature. From equation 5.6, the estimated limit for titanium is $\approx$ 1000 C [59].
It was concluded that titanium is suitable for a beam spoiler and can withstand a sufficient number of bunches [19]. It is assumed that one radiation length of titanium will be used for the spoilers (X_0=3.56 cm). Some properties of titanium are presented in Table 5.3:

	dE/dx [MeV/g/cm^2]	$\rho[g/cm^3]$	C [J/g K]	K [W/cm K]	$T(C)$
Ti	1.476	4.54	0.525	0.219	1660

Table 5.3: Properties of Titanium (adapted from [76] and [60]).

5.2.4 Collimation Depth

Halo particles with large amplitudes will radiate photons in the quadrupoles close to the interaction region; in particular, photons generated within the strong final doublet may strike inner parts of the detector and cause an unacceptable background. The required collimation depth is defined as the aperture within which photons generated by halo particles pass cleanly through the interaction region [19]. The collimation depth has been calculated in [62]. Figure 5.4 shows the limiting case for photons generated by an incoming halo in the final doublet; the resulting collimation depth is $\pm 13\sigma_x$ and $\pm 80\sigma_y$, where σ_x and σ_y are the nominal transverse

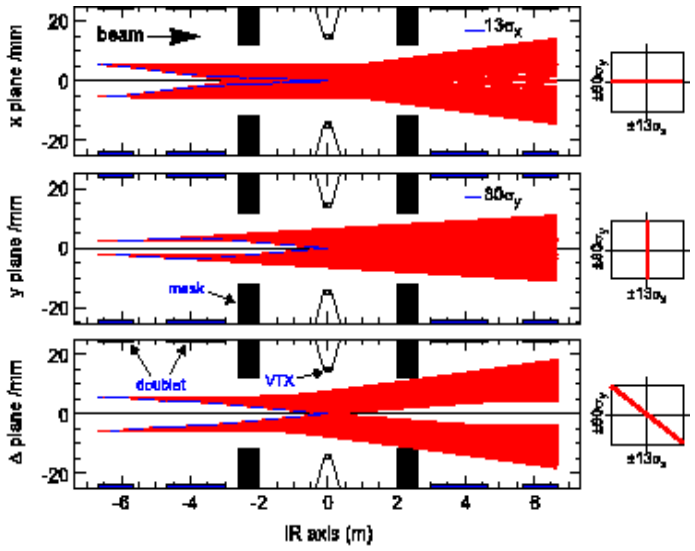

Figure 5.4: Synchrotron radiation fan generated by the last quadrupoles and traced through the IR. The envelope defines the required collimation depth of $\pm 13\sigma_x$ and $\pm 80\sigma_y$. The limiting aperture is defined in the diagonal plane by the exit 24 mm mask (adapted from [19]).

beam dimensions at 250 GeV. The values in Table 5.4 represent the nominal physical apertures of the spoilers in the beam delivery system.

Spoiler	x	y
ESPOI	4	20
XYSPOI	3	1
COLX	3.9	0.6
COLY	0.9	2.7

Table 5.4: Physical apertures (gaps) in mm of the various spoilers in the BDS. ESPOI= energy spoiler, XYSPOI= betatron spoiler (CDS), COLX(Y)= CCS spoilers (adapted from [52]).

5.3 The problem of spoiler protection

5.3.1 Motivation

The TESLA design for the collimation system incorporates many of the hard lessons from the Stanford Linear Collider (SLC), the only linear collider built so far. Over the years, the SLC has installed a large number of collimators to reduce the background in the detector and this is also felt to be essential for any future linear collider. On inspection at the end of the 1994-1995 run, it was found that many of these collimators were badly damaged. The collimators had been coated with a layer of gold to reduce the number of backscattered particles. Unfortunately the thermal contact between the gold layers and the body of the collimators was insufficient and the beam melted a very irregular channel through the gold. This caused wakefields that were roughly 25-50 times larger than expected [64]. Most of these damaged collimators were replaced for the 1996 run.

Tests performed for the NLC at SLAC showed that an electron or a positron beam are capable of damaging the accelerator's structures and beamline vacuum chambers during a single accelerator pulse if the beam is mis-steered. Pilot beams were sent on a copper target of 1.4 mm thickness since there is no guarantee that a first pulse through the linear collider will traverse the system properly. The copper sample was hit by a $\sigma_{x,y}$=15μm round beam of 10^{10} electrons and a small melted spot, about 10μm wide was seen on the sample [65].

Similar tests have been done at SLAC and figures 5.5 and 5.6 are scanning electron microscope images of selected impact points, and both the front and the back side of the impact points are shown in these figures [66]. These tests indicated a high pressure in the material along the path of the beam, with force enough to eject the liquid at the surface.

For the tests at SLAC a beam having a beam size of order 10^{-6}m was used and this is comparable to TESLA beam size in the collimation system (10^{-6}m), but a copper target instead of a titanium one, as the TESLA collimators are made of titanium (section 5.2.3). However, the copper sample was badly damaged and an important conclusion can be drawn: the accelerator structures can be degraded by impact from relatively low intensity pulses. It is the spoilers' responsibility to protect the downstream structures from a direct hit and the next chapter will answer the question: how many bunches can hit a spoiler without melting an area in it?

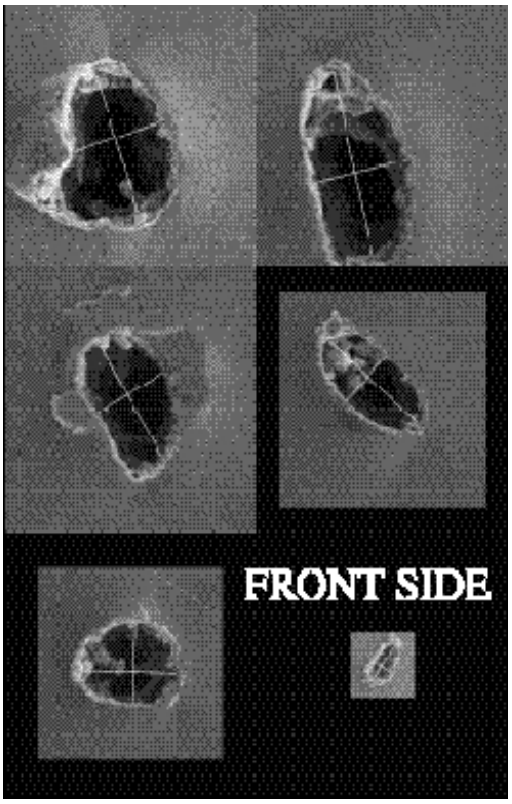

Figure 5.5: SLC- single pulse damage in copper, front side (adapted from [66]).

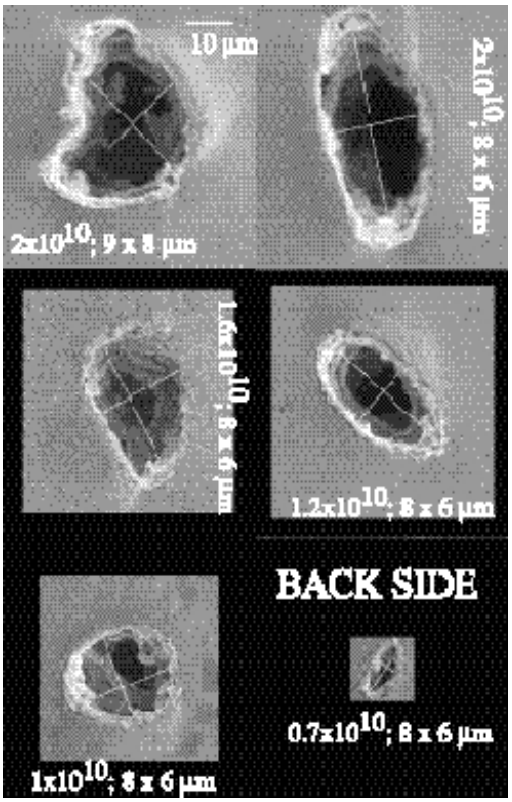

Figure 5.6: SLC- single pulse damage in copper, back side (adapted from [66]).

5.3.2 Spoiler Protection

There are two primary ways in which the beams can damage the protection collimators: dE/dX heating when the beam passes through the collimators in case of an energy error or position and angle offset, and ohmic heating by the image currents when a beam passes close to the collimator surface.

Apart from being placed in the collimation system at positions where the β- function is large and so the peak charge density is lower, the collimators are protected from a direct hit by the MES (section 5.2.2). Only two bunches are allowed to pass and the rest of the bunch train is dumped off by the FEXL. In addition, the FEXL will serve as a by-pass system during commissioning. Figure 5.7 shows the overall concept of the FEXL.

The extraction point into the FEXL is placed just downstream of the MES. Should

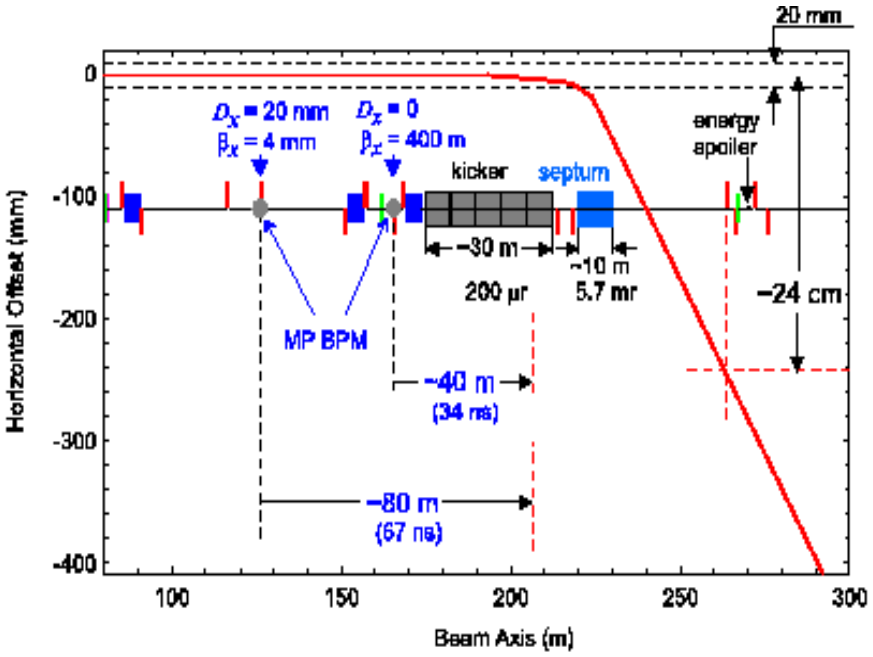

Figure 5.7: Concept of the FEXL line (machine protection system) (adapted from [19]).

an off-energy bunch train exit the linac (with $\delta E/E$ >2%), the BPM at the non-zero dispersive point in the MES can send a signal to the fast kicker system , approximately 80 m downstream. Since the signal and the beam travel in the same direction, the delay is of the order of ∼67 ns. A second BPM at a zero-dispersion point with $\beta_{x,y} = 400$ m is used to detect pure betatron errors: the delay in this case is ∼34 ns. The kicker system comprises of 30×1 m kicker modules, giving a total kick of ∼200 μr, with a rise time of 100 ns. Allowing an additional 100 ns for signal processing, the total signal delay time is ∼270 ns, which is still less than the bunch spacing of 337 ns. Hence only one (two at the most) bunches will be allowed through, before the remainder of the bunch train can be safely extracted.
When the FEXL is used as a commissioning line, two weak dipole magnets are switched on to provide the same kick geometry as the kicker system.

The beam is extracted horizontally, and then transported by a FODO system - focusing (F) and defocusing (D) quadrupoles with a drift space (O) in between - to a

section comprising both a horizontal and vertical bend, which steers the beam down ($\sim$15 mrad) to the main dump.

Chapter 6

Effects of Beam Offsets

Frisch *et al.* [56] [74] have shown that the problem of spoiler protection is technically very challenging, as the beam intensities and small spot sizes are sufficient to damage any solid material. Designs that avoid damage by increasing the beam size in the collimation system result in a very long system length and a sensitive optical design. On the other hand, if the beam collides with a spoiler due to various offsets at the exit of the linac, the beam passes into the material and the energy is deposited on a timescale of several nanoseconds causing spoiler failure. For this reason the survivability of the collimators to a given number of bunches is of great interest to accelerator physicists.

This chapter gives a qualitative review of the main effects in the TESLA linac which could cause beam offsets at the entrance of the BDS. There is a discussion regarding how these effects can be compensated and the magnitude of the emittance growth is calculated for each of them. The effects of position, angle and energy offsets are outlined for each case separately, and the specific elements that will be hit by the beam with the corresponding energy deposition on these elements is presented. The chapter continues with an estimation of the energy distribution and temperature rise on the spoilers for a maximum particle deposition.

6.1 Causes of Emittance Growth

To achieve the desired high luminosity, long trains of bunches with small transverse emittances are required. Dilutions of this emittance will arise due to changes in the particle positions or angles. The primary sources of emittance dilution may be separated into those that affect the bunch train - such as long-range longitudinal and transverse wakefields - and those that impact a single bunch - like short-range wakefields, betatron coupling, rf deflections, ground motion and jitter effects. Other effects include beam-gas scattering, where individual particles scatter from residual gas and change their trajectory, and intra-beam scattering where individual particles within a beam scatter off each other. Because the vertical beam emittance is much less than the horizontal, all these dilution effects are more important in the vertical plane.

6.1.1 Wakefield effects

Due to unavoidable manufacturing and construction tolerances, cells in accelerator structures can be misaligned relative to each other. Strong electromagnetic interaction between bunches and cavities must therefore be expected as the beam passes off axis. Wiedemann [11] shows that a bunch passing by such a structure deposits electromagnetic energy which in turn causes heating of the structure, and can act back on particles in a later segment of the same bunch or in a subsequent bunch. These fields are called wakefields and appear even at the smallest step in cross section of the vacuum chamber.

There are two types of instabilities caused by wakefields: single bunch instabilities and multibunch instabilities. The single bunch instabilities appear due to sudden changes of the vacuum chamber cross section and decay before the next bunch arrives due to the generally low value of the associated quality factor ($Q \approx 1$) [11].

The wakefield generated by the head of the bunch acts back on the bunch itself and deflects the tail. Multibunch instabilities last a longer time due to the typically high values of the quality factor Q in structures in the accelerator which resonate like cavities [11]. The wakefield generated by earlier bunches deflect the later ones in the bunch train.

Both types of wakefields appear as longitudinal or transverse modes and cause correspondingly longitudinal or transverse instabilities. If not compensated or corrected, the transverse modes (wakefields) will lead to a phenomenon known as beam break-up (single-bunch or multi-bunch) which destroys the transverse beam quality (emittance), while the longitudinal wakefields affect the energy of the particles along the bunch leading to a correlated energy spread [10].

The additional emittance growth due to random structure transverse alignment errors with an RMS of y_a is approximated by:

$$\delta(\gamma\epsilon) \approx \langle(y_a^2)\rangle \left[\pi\epsilon_0 N_B r_e W_\perp(2\sigma_z)\frac{L_{acc}\overline{\beta}_i}{2G\alpha} \left[\left(\frac{\gamma_f}{\gamma_i}\right)^\alpha - 1\right]\right] \tag{6.1}$$

where ϵ_0 is the permittivity of free space, N_B is the number of particles per bunch, r_e is the classical radius of electron, $W_\perp$ is the transverse wakefunction, L_{acc} is the length of the accelerator structures, σ_z is the bunch length, $\overline{\beta}_i$ is the average β-function ($\beta \approx 127$ m [67]), γ_i and γ_f are the initial and final relativistic factors, α is the exponential scaling of the β-function along the linac ($\alpha \approx 1$[67]) and G is: $G = e\epsilon_{rf}/(m_e c^2)$ [10].

Using the values for linac parameters given in Table 2.4 and assuming a random structure misalignment y_a of 0.5 mm for TESLA [19] it was found that the emittance dilution due to wakefield effects is $\delta(\gamma\epsilon) \approx 2.70\ 10^{-8}$ m with a relative emittance growth $\frac{\delta(\gamma\epsilon)}{\gamma\epsilon}$ of 13.5%.

It is very likely that this off-axis beam, having an additional emittance growth of

13.5% at the end of the linac (ie. entrance to the BDS), and a deflected tail and corresponding energy spread due to transverse and longitudinal wakefields, will hit at least one component of the BDS lattice producing damage (section 6.6).

In the multi-bunch case, the solution is to damp the modes generated by the passage of one bunch before the next bunch arrives. This can be done in two steps [67]: the fast "damping" is achieved by randomly detuning neighbouring RF cells within a structure. The modes generated by these cells destructively interfere with each other and cause a rapid reduction in amplitude over the short time between bunches. But the energy of the modes is still present and due to the finite tune spread of the detuned structures, the modes will at some later time re-cohere. So on a longer time scale, true damping (so-called higher order mode or HOM dampers) is used to extract the energy of the modes from the structures.

On the time scale of a single bunch it is not possible to damp the modes mechanically, but it can be controlled by the use of BNS (Balakin, Novokhatski and Smirnov) damping. This technique uses the fact that the betatron oscillation frequency depends on the energy of the particles [43]: by accelerating the bunch behind the crest of the accelerating field the tail gains less energy than the head, and the tail is more focused than the head.

6.1.2 Betatron Coupling

In practice, the particle motion is not completely contained in the horizontal or vertical plane, although to first order the motion in both planes is treated separately (see chapter 3). Fabrication and alignment tolerances will introduce rotated quadrupole components around the s-axis where only upright quadrupole fields were intended, or vertically misaligned quadrupoles [10] [11]. Whatever the source of coupling, these skew fields are considered as small perturbations to the particle motion.

Assuming purely random errors, the emittance dilution $\delta(\gamma\epsilon)$ is [10]:

$$\delta(\gamma\epsilon)_y \approx \gamma\epsilon_x 4N_{cell}\left(\frac{\tilde{K}}{K}\right)^2 \tag{6.2}$$

where $\tilde{K}$ is the skew quad gradient normalized by the magnetic rigidity $B\rho$ and K is the normalized quad gradient. In the case of quadrupole roll errors, the skew field is $\tilde{K} = 2\theta_q K$. The quadrupoles in all 365 TESLA linac FODO cells have a roll tolerance of ± 0.1 mrad [19] which gives an emittance dilution of 0.05 10^{-8} m and a vertical emittance growth of 0.25%.

Although for TESLA the emittance growth due to betatron coupling is small, such misalignments are unavoidable [11] and is good practice to place weak skew quadrupoles in the transport system to provide the ability to counter this linear coupling.

6.1.3 RF Deflections

RF deflections occur if the time-varying acceleration field is not completely oriented in the direction of beam propagation. The misalignment can arise from a misaligned accelerator structure, an angled trajectory of a beam through a structure, or asymmetries in a structure such as tilted irises or couplers. In addition to deflecting the beam, the RF deflections will increase the projected emittance by causing a deflection that is a function of the longitudinal co-ordinate s [10], approximately

$$\delta(\gamma\epsilon) \;\approx\; \langle(g^2)\rangle\,(\sigma_z K_{rf})^2\,\frac{\overline{\beta}_i L_{acc} G}{\alpha}\,\left[\left(\frac{\gamma_f}{\gamma_i}\right)^{\alpha} - 1\right] \tag{6.3}$$

$K_{rf} = 2\pi/\lambda_{acc}$ with λ_{acc}= 0.223 m [19] and g is the longitudinal-transverse coupling of the deflection.

$$g = \begin{cases} \theta_{acc}/2 & structure \quad misalignment \\ \theta_{tra}/2 & trajectory \quad misalignment \\ \leq \theta_{iris} & tilted \qquad iris \end{cases}$$

Using the TESLA parameters given in the Table 2.4 and considering a tolerance on the cavity angle error of 0.5 mrad from numerical simulations [19], it was found that the emittance dilution is $\delta(\gamma\epsilon) = 129\ 10^{-8}$ m and the vertical emittance growth is $\frac{\delta(\gamma\epsilon)}{\gamma\epsilon}$= 645%. This is the worst effect on the beam emittance.

6.1.4 Beam-Gas Scattering

Beam-gas scattering is rarely an issue for the emittance in a linac given readily achievable gas pressures - instead, the primary effect is to contribute to a halo of large amplitude particles which may cause background or radiation problems. The increase in the rms emittance can be estimated [10]:

$$\delta(\gamma\epsilon)_y \approx (n_{gas}) \frac{160\pi \cdot Z(Z+1) r_e^2 \overline{\beta}_i}{\alpha G} \left[\left(\frac{\gamma_f}{\gamma_i} \right)^{\alpha} - 1 \right] \tag{6.4}$$

where Z is the atomic number of the gas and n_{gas} is the density of the residual gas. At 20°C, $n_{gas} \approx 3.22 \cdot 10^{22}\ n_{mol} P[m^{-3}]$. Here, n_{mol} is the number of atoms per molecule of gas and P is the vacuum pressure in torr. Assuming for TESLA linac a vacuum pressure of 10^{-14}mbar [67], and using the parameters from Table 2.4, it was found that the emittance dilution is $\delta(\gamma\epsilon)$= 2 10^{-16} with an emittance growth $\frac{\delta(\gamma\epsilon)}{\gamma\epsilon}$ of $(\sim 10^{-6})$%.

It can be seen imediately that the additional emittance growth due to beam-gas scattering in linac is insignificant for transverse offsets of the centroid of the bunch, although it can contribute to the background level in the detector.

6.1.5 Ground motion and jitter effects

Given the extremely small beam sizes required at the IP, particular attention must be made to component stability, in particular with respect to ground motion and vibration. They can cause beam offsets and if the effect of the ground motion accumulates in time it can result in emittance growth due to betatron oscillations. At low frequency $\leq$ 1 Hz, the sources of ground motion are atmospheric activity, change of underground water, ocean tides, earth-tides from lunar motion, temperature variation of the surface ground etc. At high frequency $\geq$ 1 Hz, the motion consists of seismic activity and man-made noise.

What is important for a linear collider is the relative motion of two quadrupoles separated by distances less than the betatron wavelength. In order to predict the effects of longer term ground motion on linear colliders, an empirical law called the "ATL law" has been successfully used so far. It assumes that slow relative ground motion is a random process and it states that after a time T, the variance of the relative offset of two points separated by a distance L is proportional to both T and L [69]:

$$< \sigma_y^2 > = ATL \tag{6.5}$$

The parameter A varies by a few orders of magnitude when measured in different locations and is site and geology dependent. Measurements at the DESY site gave a value of $A = 4{\cdot}10^{-6}\mu m^2 m^{-1} s^{-1}$ [69].

In the TESLA linear collider there are two feedback systems [72] [73]: a Slow Feedback System located in the main linac and working at the repetition frequency of 5 Hz, and a Fast Feedback System situated in the beam delivery system and at the IP. They perform the following functions [71]:

- the Slow Feedback System situated at the end of the linac corrects position and angle of each bunch;

- the Fast Feedback System in the chromatic correction section removes angle offsets at the IP;
- the Fast Feedback System located at the IP steers the beam into collision.

A summary of these effects on the beam emittance is presented in the table below:

	$\delta(\gamma\epsilon)$	$\frac{\delta(\gamma\epsilon)}{\gamma\epsilon}$
Wakefield effects	2.70 E-8	13.5%
Betatron coupling	0.05 E-8	0.25%
RF deflections	129 E-8	645%
Beam-gas scattering	2 E-16	(10^{-6})%

Table 6.1: Summary of the main effects which degrade the beam emittance in TESLA linac.

6.2 Beam Offsets

When a bunch of particles comes out of the linac with the ideal design parameters then only a small number of particles in the transverse tail of the bunch are scattered by the spoiler. However if a bunch enters the BDS with incorrect parameters then a large part of that bunch may impact on a small area of a particular spoiler, and produce damage.

Although the beam is enlarged at the spoiler location by optical magnification it still exhibits an enormous power density which can not be withstood by any material for any length of time. On the other hand, the spoilers are close to the beam and one has to take into account the possibility that a mis-steered beam hits the spoiler head on. Although the spoiler is able to accept two bunches in such a case [19], and during that time the beam loss can be detected and the remaining bunch train can be dumped away, the question to be answered is what happens in the case of a faulty protection system? We are interested to find out what elements will be hit, what will be the maximum particle deposition and temperature rise on them in this case, and finally, will they sustain damage or will they melt an area in these elements?

In order to provide an answer to these questions, computer simulations were performed for beam offsets in position, angle and energy. A bunch containing 10^5 particles in the Gaussian core was sent out of the linac with an energy of 250 GeV and an energy spread of $\sigma_\delta = 1.5 \cdot 10^{-3}$ [67]. The bunch was tracked through the BDS lattice to the IP. Scattering effects were not included for this simulation and collimation apertures were treated as hard-edges (ie. a particle which hit a particular spoiler is deemed lost). It is also worth mentioning here that no particles are lost when the bunch core was tracked on axis.

6.2.1 Offset in Positions

The offsets in positions, angles and energy are applied at the entrance to the BDS. The results obtained for offsets in horizontal position applied to the centroid of the bunch are shown in figure 6.1.

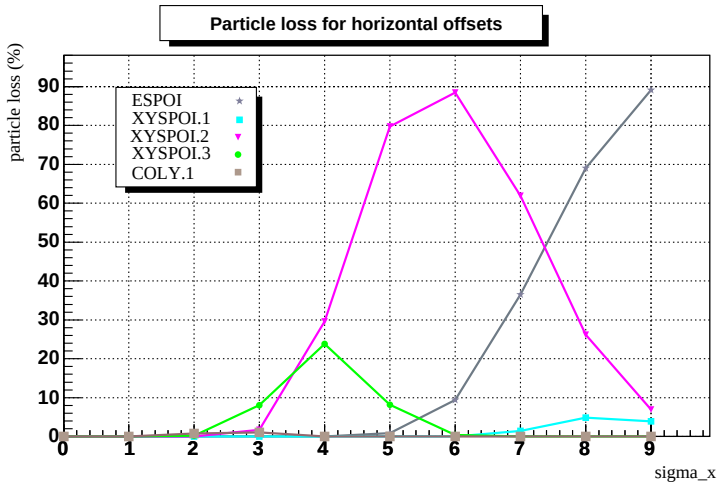

Figure 6.1: Particle losses as a function of horizontal beam offset.

For a varying offset between $1\sigma_x$ and $9\sigma_x$, the particles are lost mainly in the CDS spoilers. Due to non-linear effects, which get worse progressively downstream, the beam becomes disrupted and hits first the third position spoiler even at small offsets ($1\sigma_x$ - $3\sigma_x$); as the horizontal beam offset is increased, other spoilers situated upstream in the lattice will start to intercept particles. The second position spoiler clearly dominates the situation at an offset between $4\sigma_x$ - $6\sigma_x$. At larger offsets, the energy spoiler and first position spoiler start to shadow the following two. For offsets larger than $6\sigma_x$, the particle deposition on the energy spoiler increases, reaching a maximum value of 89% at $9\sigma_x$. The beam is lost at an offset of $10\sigma_x$.

"MERLIN" calculates not only the number of particles that strikes the collimator,

but also records their spatial distribution. This information can be used to obtain the energy deposition and thus the rise in temperature, to see whether the collimator sustains damage. Figure 6.2 gives an example of particles lost on the energy spoiler ESPOI and the exact position where they hit this element when the beam comes out of the linac with an offset in the horizontal plane.

The horizontal and vertical axes are expressed in terms of σ_x and σ_y and the colours represent the number of particles that strike the collimators in different regions. For the purposes of simulation, the collimator surface is divided into a grid of pixels and this number of pixels is kept constant throughout this study for the beam core. The band in the middle is the beam aperture measuring 4 mm across (Table 5.4), and is expressed in number of σ_x in the picture.

Although the number of particles lost on the ESPOI is maximum at an offset of $9\sigma_x$, the particle deposition per pixel is small (450 particles). They strike a large area in the collimator because the offset is very large and the energy spoiler is situated in a point with large dispersion in the horizontal plane (ie. beam is spread out).

Figure 6.3 shows a similar case but for the second position spoiler XYSPOI.2 when $\approx 88\%$ of the particles are lost. The gap in the middle measures 3 mm horizontally and 1 mm vertically (Table 5.4) and here is expressed in numbers of σ_x and σ_y. The spot is smaller compared to the one in figure 6.2 as other particles are intercepted by the upstream energy spoiler, such that the number of particles per pixel is 1300.

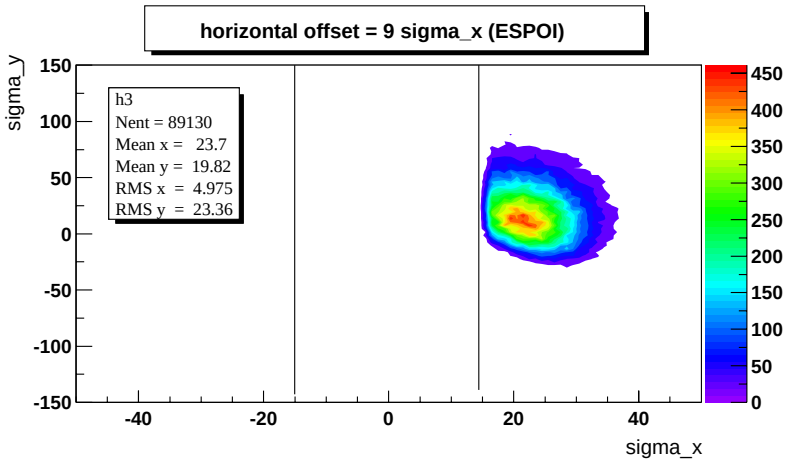

Figure 6.2: Mapping of the particles lost on the energy spoiler at an offset of $9\sigma_x$ in the horizontal plane (the aperture measures $31\sigma_x$ horizontally and $2857\sigma_y$ vertically).

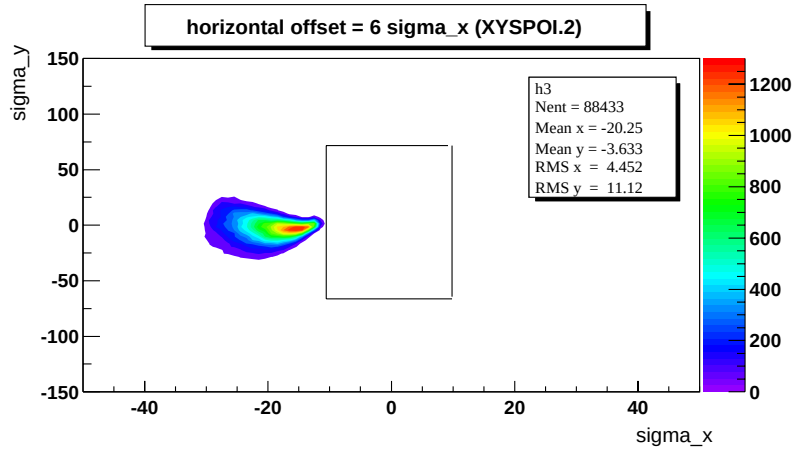

Figure 6.3: Mapping of the particles lost on the second position spoiler at an offset of $6\sigma_x$ in the horizontal plane (the gap measures $24\sigma_x$ horizontally and $143\sigma_y$ vertically).

For a varying offset from $1\sigma_y$ to $34\sigma_y$ in the vertical position, important losses occur in all four position spoilers and one of the CCS collimators (figure 6.4). The energy spoiler is not hit at all even at large offsets for two reasons: firstly, its vertical aperture is the same as for the rest of the elements in the BDS lattice, apart from collimators, namely 20 mm (Table 5.4), and secondly, the vertical dispersion is much smaller than the horizontal one. The beam starts to strike the spoilers when the centroid of the bunch is shifted up by $15\sigma_y$. Again, due to nonlinearities, the second and the third position spoilers are the most affected at smaller offsets ($20\sigma_y$ - $25\sigma_y$), but as the offset increases, the first position spoiler starts to catch more particles than the following three. The beam is lost at an offset of $35\sigma_y$.

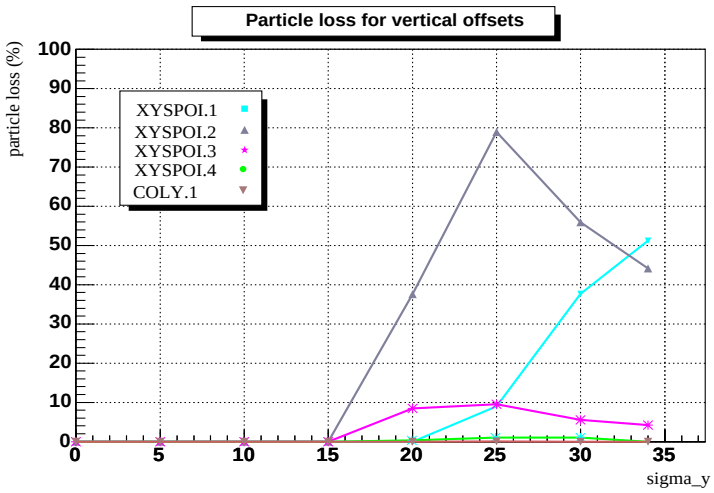

Figure 6.4: Particle losses as a function of vertical beam offset.

The maximum particle distribution occurs at an offset of $25\sigma_y$ on the second betatron collimator XYSPOI.2 when ≈79% of the particles are lost. The particle deposition per pixel is 8000 in this case (figure 6.5).

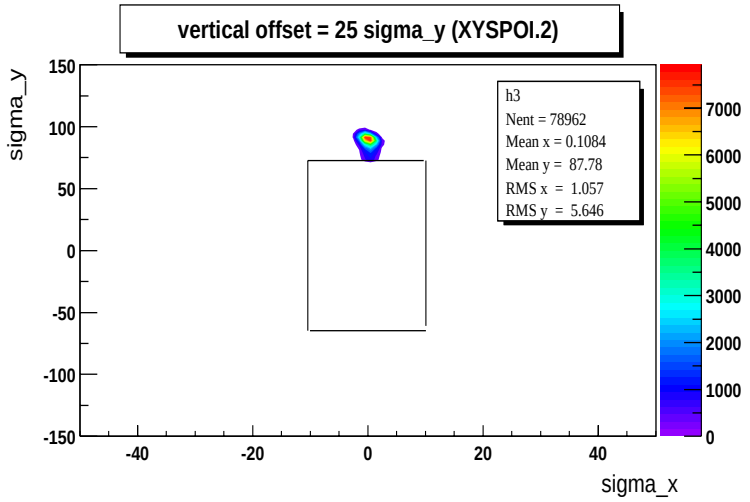

Figure 6.5: For an offset in the vertical plane, the maximum number of particles lost occurs on the second position spoiler at an offset of $25\sigma_y$ (aperture size: $24\sigma_x$ horizontally and $143\sigma_y$ vertically).

6.2.2 Offset in Angles

Similar studies were done for offsets in horizontal and vertical angle. All the other coordinates of the centroid of the bunch were set to zero apart for the angles, which were varied in steps of 0.5 μrad. The results obtained for offsets in angle x' are shown in figure 6.6. Only three collimators are hit in this case. The beam strikes firstly the position spoiler XYSPOI.1 at an offset of 2 μrad and the number of particles caught by it increases drastically reaching a maximum at 4.5 μrad and then decreases as the energy spoiler starts to play a more important role. The particle loss on the second position spoiler is less than 0.1% for offsets between 0 and 5.5 μrad. The beam is lost at 6μrad.

The number of particles that strike the collimators is a maximum at an offset of 4.5 μrad. The mapping of the particle distribution is shown in figure 6.7: $\approx$97 % of the particles hit the collimator and the particle deposition per pixel is 2750.

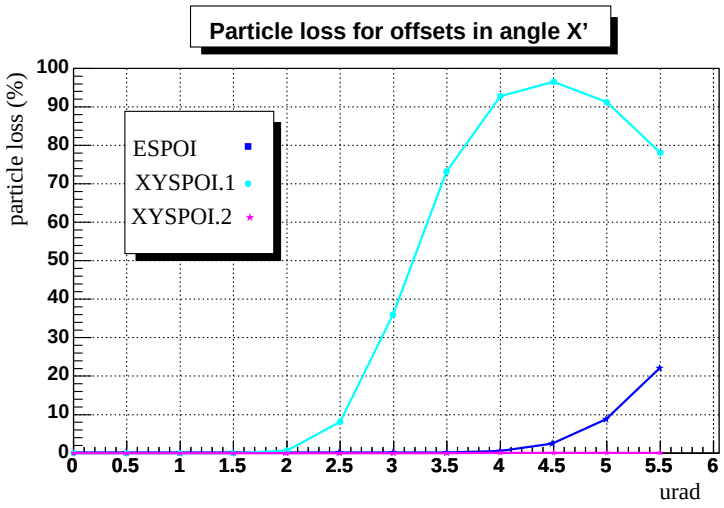

Figure 6.6: Percentage of particle loss for a beam offset in x' angle.

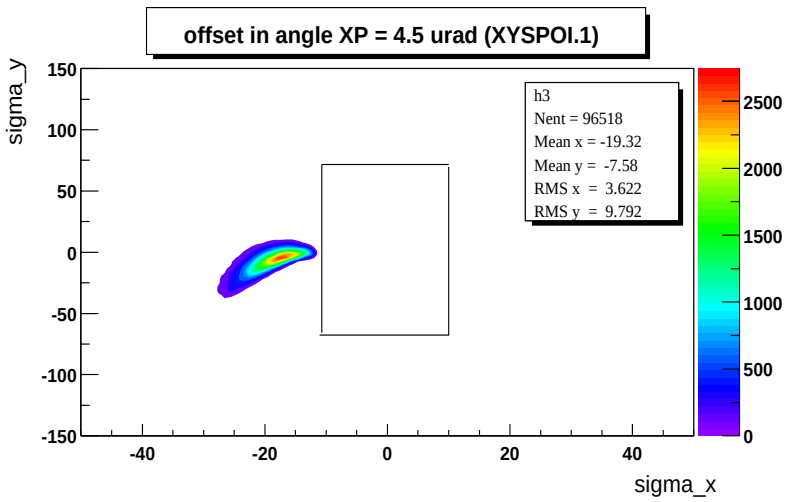

Figure 6.7: Mapping of the maximum particle loss for offset in angle x' at 4.5 μrad (aperture size: $24\sigma_x$ and $143\sigma_y$).

The results obtained for beam offsets in vertical angle are presented in figure 6.8. The situation is a bit different in this case in the sense that the beam offset is varying on a much smaller scale. Particles strike the collimators at offsets between 1.5 μrad and 2.5 μrad, at 3 μrad the beam is lost. The energy spoiler is not hit at all, only position spoilers. The reason is that when the beam is tracked with an offset in vertical angle, it passes through the energy spoiler's large aperture (20 mm) but it can not pass cleanly through the gap of the position spoilers which is 1 mm vertically (Table 5.4).

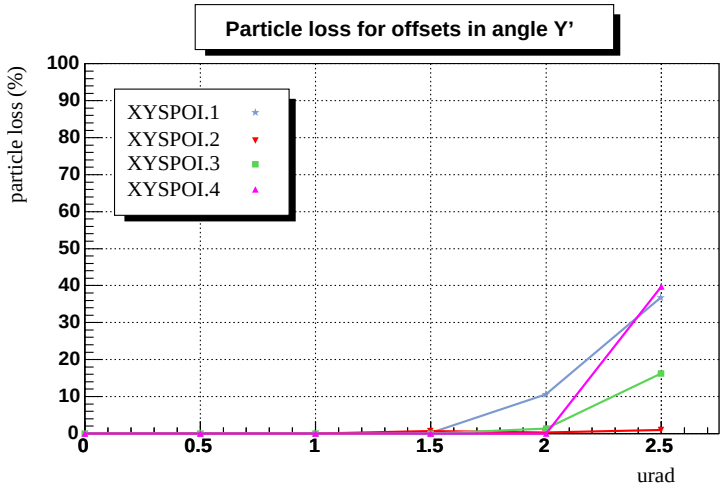

Figure 6.8: Percentage of particle loss for a beam offset in y' angle.

The particle deposition on the collimators is mapped for two situations: on the first collimator XYSPOI.1 and on the fourth collimator XYSPOI.4 at an offset of 2.5 μrad. Both pictures show that the number of particles lost is not very different: $\approx$37% on XYSPOI.1 with 1950 particles per pixel and $\approx$40% on XYSPOI.4 with 8000 particles per pixel. The spot of the first spoiler is larger as it is the first one encountered in the lattice for a given offset.

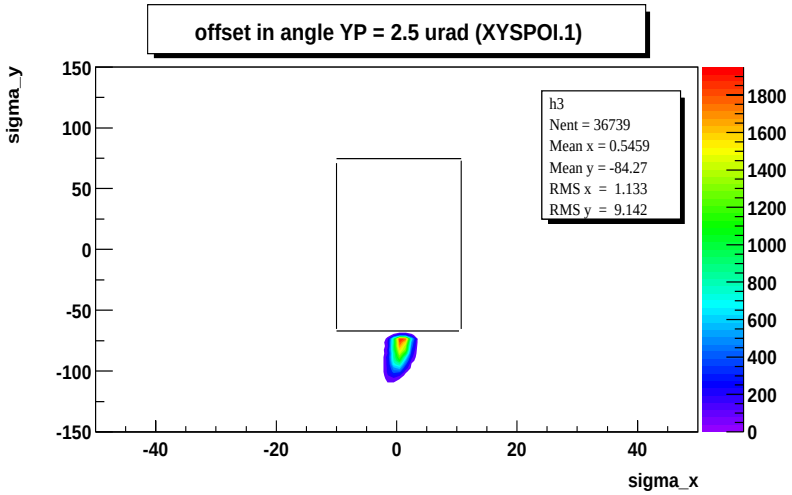

Figure 6.9: Mapping of particle loss at an offset of 2.5 μrad on first position spoiler (aperture size: $24\sigma_x$ and $143\sigma_y$).

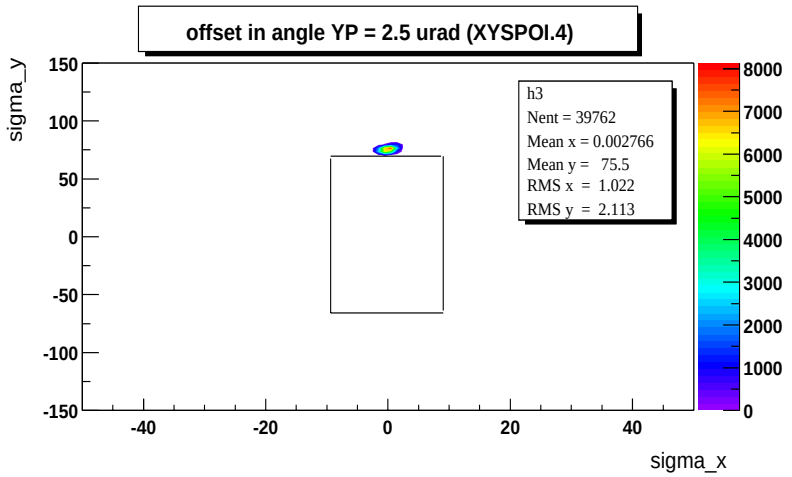

Figure 6.10: Mapping of particle loss at an offset of 2.5 μrad on fourth position spoiler (aperture size: $24\sigma_x$ and $143\sigma_y$).

6.2.3 Offset in Energy

The case was also examined of a beam which is sent out, not only with a spread in energy of $\sigma_\delta = 1.5 \cdot 10^{-3}$, but also with offsets with respect to its nominal energy, 250 GeV. Being situated at a high dispersion point (D_x = -100mm) [19], the energy spoiler clearly dominates the picture as figure 6.11 shows, although particles are lost in other collimators as well. The whole beam is lost at an offset of 0.030 GeV.

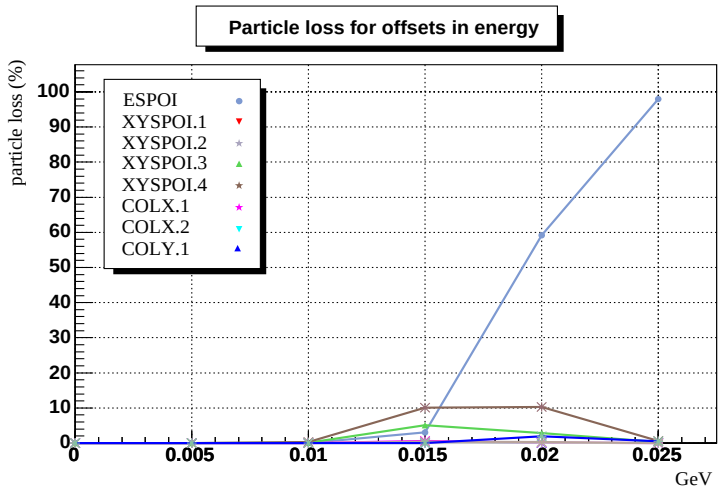

Figure 6.11: Percentage of particle loss as a function of energy offset in GeV.

The maximum particle deposition of ≈98% is at 0.025 GeV, and the distribution is shown in figure 6.12. The maximum number of particles per pixel is 5500 in this case.

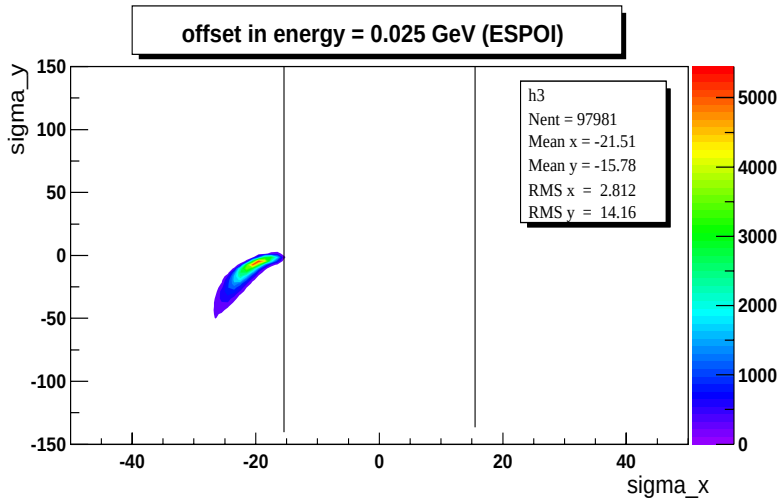

Figure 6.12: Particle deposition on the energy spoiler for an offset of 0.025 GeV (the gap measures over $31\sigma_x$ horizontally and $2857\sigma_y$ vertically).

6.3 The Contribution from Beam Halo

In the cases considered so far, the particle deposition per pixel for various core beam offsets varies from a couple of hundred particles to several thousand. But the beam core is accompanied by a halo of particles of about $\approx$0.1% of the total number of particles per bunch. Having a large betatron amplitude, these particles will hit various elements in the BDS lattice, especially spoilers due to their tight apertures. Therefore, for a realistic calculation of temperature rise in the collimators, an estimation of the contribution from the beam halo is needed at this stage.

The beam halo and the beam core are treated separately in the "MERLIN" code. Only the beam halo was constructed for this study, having 10^5 particles uniformly distributed within an extent of $\pm 13\sigma_x$ horizontally and $\pm 80\sigma_y$ vertically plus 25% increase over collimation depth. The 25% overlap is an arbitrary safety margin: the phase space volume was "filled" with particle to avoid the presence of "holes" in the collimated phase space due to optics [67].

The particles' mean energy was 250 GeV with an energy spread of -3% $\leq \Delta p/p \leq$0.5%. Unfortunately, there is no real model for the energy distribution of the halo or what that might look like [67]. The cut at -3% is based on previous simulations, as no particles survived beyond this limit. The upper cut is based on the following argument: the initial Gaussian energy spread at the entrance of the linac has a RMS of 3% and this is adiabatically damped to $\approx 0.05\%$ at the end of the linac [67].
The beam halo was tracked on axis through the BDS lattice until the final doublet. Scattering effects on spoilers' material were not included for this simulation. The results are presented in figure 6.13: the main components hit by the halo are the CDS collimators (ESPOI at 678 m, and all four betatron spoilers XYSPOI at 778, 878, 977 and 1077 m) but also the CCS collimators situated at 1191, 1283, 1375 and 1467 m. The halo also strikes other components such as drifts and quadrupoles, but the particle deposition is insignificant (less than 0.1%).

The mapping of the halo particles loss on the CDS collimators is shown in figure 6.14 for the energy spoiler, figure 6.15 for the first and second betatron collimator, and figure 6.16 for the third and fourth betatron collimator. The left plots are

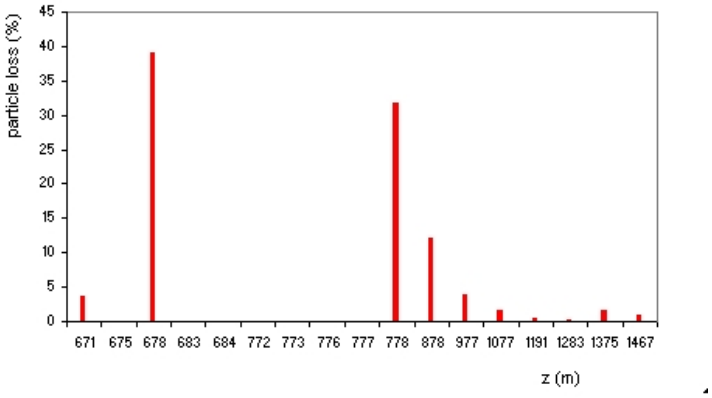

Figure 6.13: Particle losses along the beamline, expressed as a percentage of the initial halo particle number tracked.

three-dimensional images of the spoilers with the gap in the middle. The particle deposition per pixel is represented as bars. The right plots are two-dimensional images of the same spoilers. The axis are expressed in numbers of σ_x and σ_y and the colours represent the particle deposition on various regions. The colours are different in the left and right images as the scales are different and are chosen automatically by the program. The aperture size of the energy spoiler is over $31\sigma_x$ and $2857\sigma_y$ and for the position spoilers is $24\sigma_x$ and $143\sigma_y$. The pixel size was kept constant for comparison for all three left and right diagrams. Although in the simulation program the beam halo contains the same number of particles as the beam core for comparison, they are spread out due to their large betatron amplitudes, such that the maximum particle deposition per pixel is insignificant compared to the particle deposition given by the core (see right plots). There are three particles per pixel for the ESPOI, six for the XYSPOI.1 and two for the XYSPOI.2, and one particle for the XYSPOI.3 and XYSPOI.4. These results do not differ much if the halo is tracked with offsets applied. Therefore, for calculation of temperature rise, only the particle deposition given by the core will be taken into account from now on.

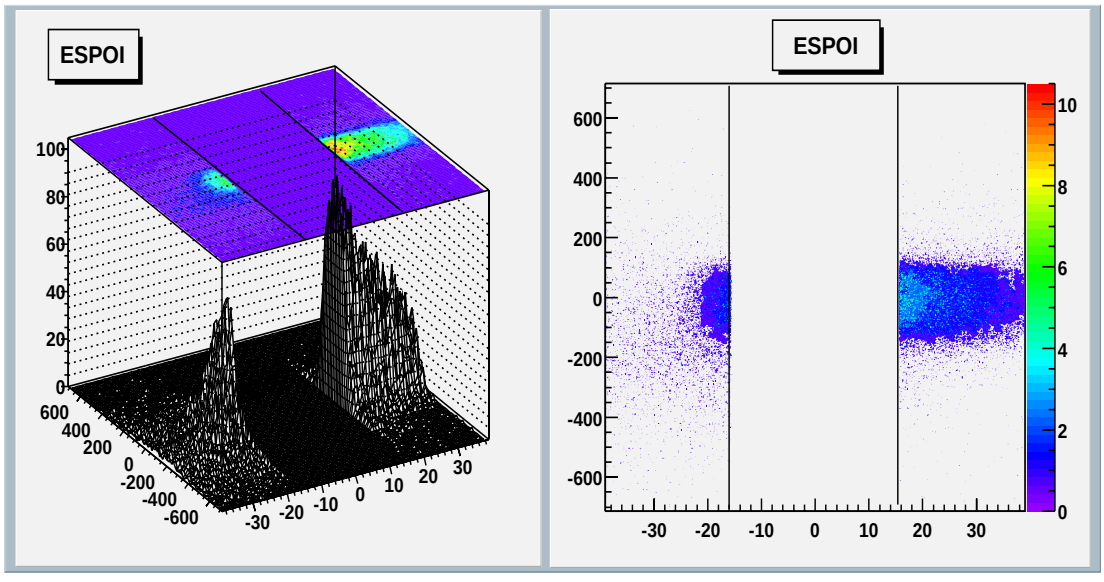

Figure 6.14: Particle deposition on the energy spoiler, due to halo (the gap measures over $31\sigma_x$ horizontally and $2857\sigma_y$ vertically).

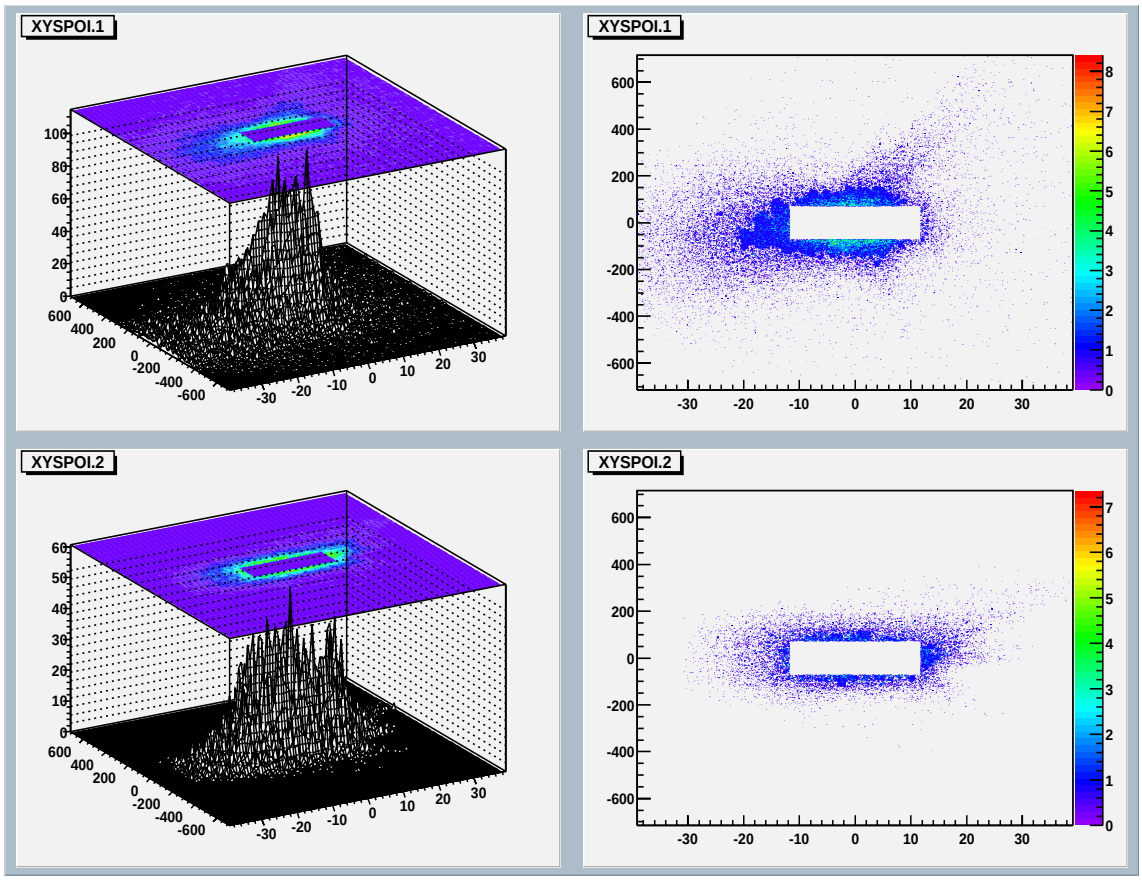

Figure 6.15: Particle deposition on the first and second betatron spoiler due to halo, in two-dimensional and three-dimensional images (aperture size: $24\sigma_x$ and $143\sigma_y$).

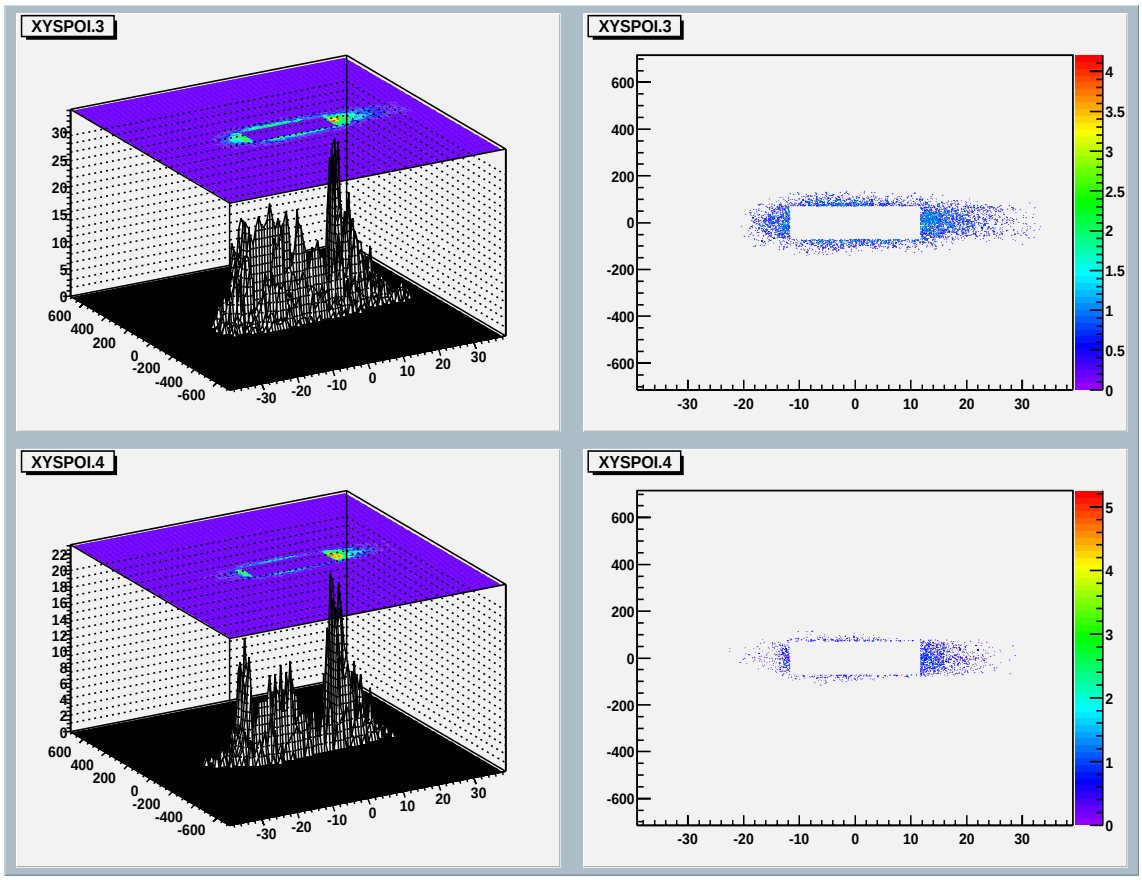

Figure 6.16: Particle deposition on the third and fourth betatron spoiler due to halo, in two-dimensional and three-dimensional images (aperture size: $24\sigma_x$ and $143\sigma_y$).

6.4 The Interaction of Electrons with Matter

Charged particles moving through matter lose energy by collision and by radiation. The loss rate of these two processes depends strongly upon the particle's energy: at low energy the collision losses are more important, while at large energies the radiation losses are dominant. The critical energy E_c is defined as the energy at which the two loss rates are equal, and has the expression [76]:

$$E_c \simeq \frac{610\,MeV}{Z + 1.24} \quad (solids\ and\ liquids) \tag{6.6}$$

$$E_c \simeq \frac{710\,MeV}{Z + 0.92} \quad (gases) \tag{6.7}$$

The critical energy is sometimes approximated in textbooks as E_c ~600 MeV/Z [75].

6.4.1 Energy Loss by Radiation

A 250 GeV electron which hits a collimator has an energy $E > E_c$ so that the energy loss due to radiation is more important than the energy loss due to collision with the medium. The electron incident upon matter brakes in the field of the nucleus and is decelerated over a short distance, radiating energy in the form of a photon. This effect is called bremsstrahlung and depends strongly upon the material and the energy: it increases roughly linearly with energy and quadratically with the atomic number Z of the medium. The interaction of the newly produced photon with the Coulomb field of the nucleus leads to the phenomenon of pair production whereby the photon disappears and a positron and an electron simultaneously come into existence. For this phenomenon to occur, the energy of the photon must exceed the rest energy of the $e^- - e^+$ pair. The excess energy appears almost completely as kinetic energy of the e^- and e^+, while the recoil of the nucleus takes care of momentum

conservation. It is worth mentioning here that at high energy only pair production is of any importance (the photoelectric effect dominates at low energies in the keV range while the Compton effect dominates for energies from several hundreds of keV to a few MeV).

The electron produced by pair production radiates more photons which again materialize into $e^- - e^+$ pairs. Thus the number of particles (electrons and photons) rapidly increases as the radiation progresses through matter and their average energy decreases. This phenomenon is called a cascade shower and continues only as long as electrons have energies greater than E_c.

6.4.2 Energy Loss by Collision

As the process of showering goes on, more and more electrons fall into an energy range where radiation losses cannot compete with collision losses. The electrons are no longer capable of radiating photons and photons are no longer capable of producing pairs, and at this point the shower dies out.
The electrons' low energy will be now dissipated through collisions with the atomic electron clouds. As a result, the atoms are either excited or ionised. Excitation occurs when the binding energy of the atomic electron is greater than the energy of the photon absorbed, such that it goes over into a quantum orbit of higher energy. Ionisation implies that the binding energy of the atomic electron is less than the energy of the photon absorbed and the atomic electron breaks loose from the atom. The energy lost to ionisation by electrons is described by the Bethe-Bloch formula [76]:

$$-\frac{dE}{dx} = Kz^2\frac{Z}{A}\frac{1}{\beta^2}\left[\frac{1}{2}\,ln\frac{2m_ec^2\beta^2\gamma^2T_{max}}{I^2} - \beta^2 - \frac{\delta}{2}\right] \tag{6.8}$$

where T_{max} is the maximum kinetic energy which can be imparted to a free electron in a single collision and K is $4\pi\, N_A r_e^2 m_e c^2$ (with N_A Avogadro's number, r_e classical

electron radius and $m_e c^2$ the electron mass multiplied by the speed of light squared); z is the charge of the incoming particle, $\beta = v/c$ and $\gamma = 1/\sqrt{1-\beta^2}$ are the kinematic variables, Z/A is the atomic number divided by the atomic mass of the absorber medium, I is the mean excitation energy in eV [76] and δ represents a density effect correction to ionization energy loss.

It can be seen that the energy loss depends on the properties of the incident particle through the relation $dE/dx \sim z^2/v^2$ and is independent of mass m; apart from a weak dependence through I in the logarithmic term, dE/dx depends also on the medium through variations of Z/A.

6.4.3 The Energy Loss by a Single Electron

A minimum ionising electron loses energy according to equation 6.8 and this energy loss for titanium is $(dE/dx)_{Ti} \simeq 1.476\ MeV \cdot cm^2/g$ [76]. The product between the energy loss and the density $\rho_{Ti} \simeq 4.54\ g/cm^3$ [76] gives the energy loss per unit length is $(dE/dx) \cdot \rho \simeq 6.701$ MeV/cm.

It was shown previously that electrons at high energies produce electromagnetic showers which develop appreciably over the one radiation length depth of the collimator. GEANT4 simulations estimate this effect as producing a factor 2.5 in the energy deposition by the time the particle has travelled one radiation length [77]. Taking into account the fact that each e^- in the simulation program represents $2 \cdot 10^5$ particles in the real bunch (Table 2.4), the real energy deposited by the e^- in the spoiler is the product of all three quantities: $E_{e^-} = 5.36 \cdot 10^{-7}$ J/cm.

If a collimator is divided into a grid of pixels of size δ, the temperature rise given by n electrons, each of which deposits an energy E_{e^-} per pixel, is:

$$T = \frac{n}{\delta^2} \frac{E_{e^-}}{C\rho} \tag{6.9}$$

where C=0.525 J/gK is the specific heat of Titanium [78], ρ is the density (ρ=4.54 g/cm^3 5.3), thus $C\rho$ is $2.36 J/K cm^3$. The variation of C with temperature is not considered for simplicity (at high temperatures, i.e. in the classical limit, C is a

constant). This formula will only give sensible answers if there are many particles per pixel, otherwise the temperature distribution depends on pixel size. For a pixel area of 1 micron square, equation 6.9 gives a temperature rise of 22.4 K per simulated particle.

6.5 The Temperature Rise on Spoilers

In order to determine the survivability of the collimator to a given number of incident bunches, a temperature study was done for the case when the particle deposition per pixel is maximum, whatever the type and the magnitude the offset has. It was found that for an offset of $20\sigma_y$ in the vertical plane, there are 9000 electrons per pixel on the second betatron collimator (figure 6.17). The total number of pixels is 100 on the horizontal and vertical axis each.

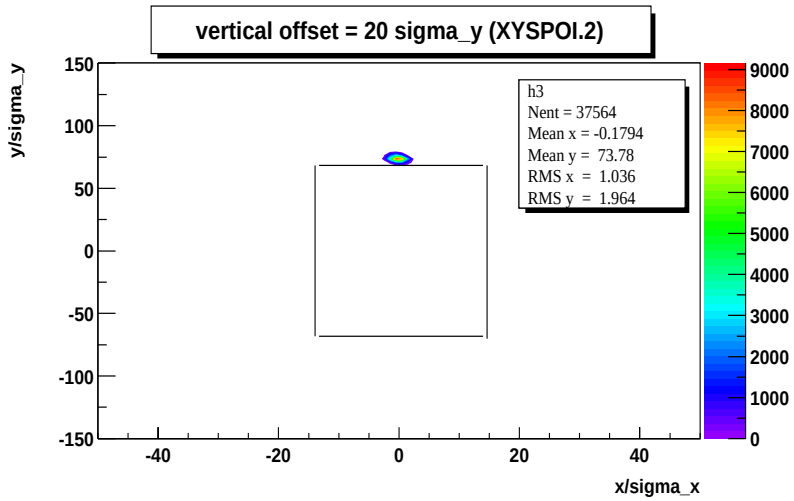

Figure 6.17: The particle deposition per pixel is maximum for an offset in the vertical plane (9000 particles).

When calculating the temperature rise due to a given number of pulses, one must take into account the thermal conductivity between adjacent pixels. Therefore, a

brief review of the mathematical formalism of heat flow used for this study is given in the following section.

6.5.1 A Mathematical Analysis of the Heat Transfer

When a temperature gradient exists in a body[1] there is an energy transfer from the high-temperature region to the low-temperature region. The energy is transferred by conduction and the heat-transfer rate q is proportional to the temperature gradient $\partial T/\partial x$:

$$q = -kA\frac{\partial T}{\partial x} \tag{6.10}$$

This is Fourier's law of heat conduction where A is the unit area and k is the thermal conductivity of the medium indicating how fast heat flows (the minus sign is inserted so that the second law of thermodynamics will be satisfied; the basic equation which governs the heat transfer in a solid was determined using equation 6.10 as a starting point). For a steady state with no heat generation, the Laplace equation for a two-dimensional system is:

$$\frac{\partial^2 T}{\partial x^2} + \frac{\partial^2 T}{\partial y^2} = 0 \tag{6.11}$$

The thermal conductivity is considered constant, and the solution to this equation will give the temperature in a two-dimensional body as a function of the two independent spatial coordinates x and y. The heat flow in the x and y directions may be calculated from the Fourier equation 6.10. The total heat flow at any point in the material is the resultant of the q_x and q_y at any point.

$$q_x = -kA_x\frac{\partial T}{\partial x} \tag{6.12}$$

$$q_y = -kA_y\frac{\partial T}{\partial y} \tag{6.13}$$

[1]The book "Heat Transfer" [79] was used throughout this study.

If the solid body is suddenly subjected to a change in environment, some time must elapse before an equilibrium temperature condition will prevail. The non-equilibrium condition is referred to as the unsteady state and the equation which governs this situation in two-dimensions is :

$$\frac{\partial^2 T}{\partial x^2} + \frac{\partial^2 T}{\partial y^2} = \frac{1}{\alpha}\frac{\partial T}{\partial \tau} \tag{6.14}$$

where τ represents the time and α is the thermal diffusivity, usually expressed in m^2/s ($\alpha = k/\rho c$ with k thermal conductivity, ρ the density and c the specific heat). The solution to equation 6.11 may be obtained by analytical, graphical or numerical techniques. For the case of heat tranfer between adiacent pixels, the problem is best handled by a numerical method with the computer.

Numerical Solution for Heat Transfer

The analyses can be limited to a two-dimensional system divided into increments as shown in figure 6.18. The subscript m denotes the x position, and the subscript n denotes the y position. Within the solid body the differential equation which governs the heat flow is:

$$k\left(\frac{\partial^2 T}{\partial x^2} + \frac{\partial^2 T}{\partial y^2}\right) = \rho\, c\frac{\partial\, T}{\partial \tau} \tag{6.15}$$

where c is the specific heat, ρ is the density and τ is the time. The second partial derivatives and the time derivative may be approximated by (figure 6.18):

$$\frac{\partial^2 T}{\partial x^2} \approx \frac{1}{(\Delta x)^2}\left(T_{m+1,n} + T_{m-1,n} - 2T_{m,n}\right) \tag{6.16}$$

$$\frac{\partial^2 T}{\partial y^2} \approx \frac{1}{(\Delta y)^2}\left(T_{m,n+1} + T_{m,n-1} - 2T_{m,n}\right) \tag{6.17}$$

$$\frac{\partial T}{\partial \tau} \approx \frac{T^{p+1}_{m,n} - T^{p}_{m,n}}{\Delta \tau} \tag{6.18}$$

In this relation the superscripts designate the time step. Combining the relations above gives the difference equation :

$$\frac{T^{p}_{m+1,n} + T^{p}_{m-1,n} - 2T^{p}_{m,n}}{(\Delta x)^2} + \frac{T^{p}_{m,n+1} + T^{p}_{m,n-1} - 2T^{p}_{m,n}}{(\Delta y)^2} = \frac{1}{\alpha} \frac{T^{p+1}_{m,n} - T^{p}_{m,n}}{\Delta \tau} \tag{6.19}$$

Thus, if the temperatures of the various nodes are known at any particular time, the temperatures after a time increment $\Delta\tau$ may be calculated by writing equation 6.19 for each node. The procedure may be repeated to obtain the distribution after any desired number of time increments.

If the increments of space coordinates are chosen such that $\Delta x = \Delta y$ the equation for $T^{p+1}_{m,n}$ becomes:

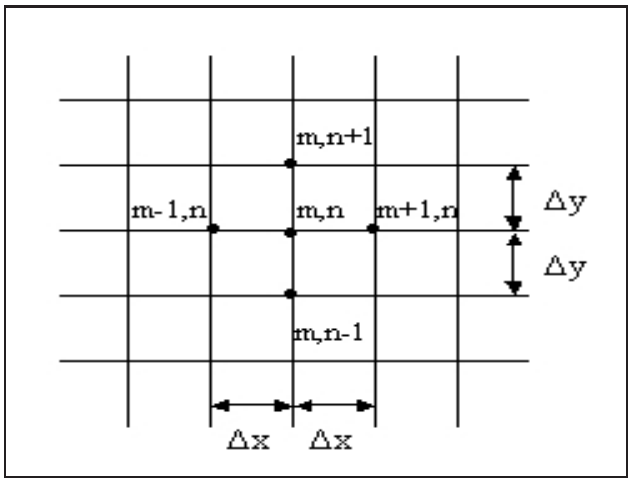

Figure 6.18: A sketch illustrating the nomenclature used in two-dimensional numerical analysis for heat conduction (adapted from [79]).

$$T_{m,n}^{p+1} = \frac{\alpha\Delta\tau}{(\Delta x)^2}\left(T_{m+1,n}^{p} + T_{m-1,n}^{p} + T_{m,n+1}^{p} + T_{m,n-1}^{p}\right) + \left[1 - \frac{4\alpha\Delta\tau}{(\Delta x)^2}\right] \cdot T_{m,n}^{p} \quad (6.20)$$

If the time and distance increments are chosen such that $(\Delta x)^2/\alpha\Delta\tau = 4$, it can be seen that the temperature at the node (m,n) after a time increment reduces to the arithmetic average of the four surrounding nodal temperatures at the beginning of the time increment. In this formulation, the calculation proceeds directly from one time increment $T_{m,n}^{p}$ to the next $T_{m,n}^{p+1}$ until the temperature distribution is calculated at the desired final state.

6.6 Calculation of Temperature Rise

The previous equations were used to calculate the temperature distribution arising when a number of bunches strike a collimator. For the case illustrated in figure 6.17 and assuming that the spoiler is hit by one bunch (figure 6.19), at time $t = 0$ the temperature distribution initially has a fine grained-structure (figure 6.20). It is assumed that the initial temperature of the spoilers is 300 K. At $t = 336$ ns, before a new bunch will hit the collimator, the structure produced by the particles will be blurred out by thermal conduction. This is shown in figure 6.21 when the temperature increases to T = 413.93 K.

The repeated effects of energy deposition and thermal diffusion can follow for a number of pulses until some temperature is reached. Figure 6.22 shows the energy spoiler after 22 bunches, at which point the hottest temperature is 1989 K. The melting temparture for titanium is 1933 K, and is very likely that the beam will melt an area at the collimator in this case.

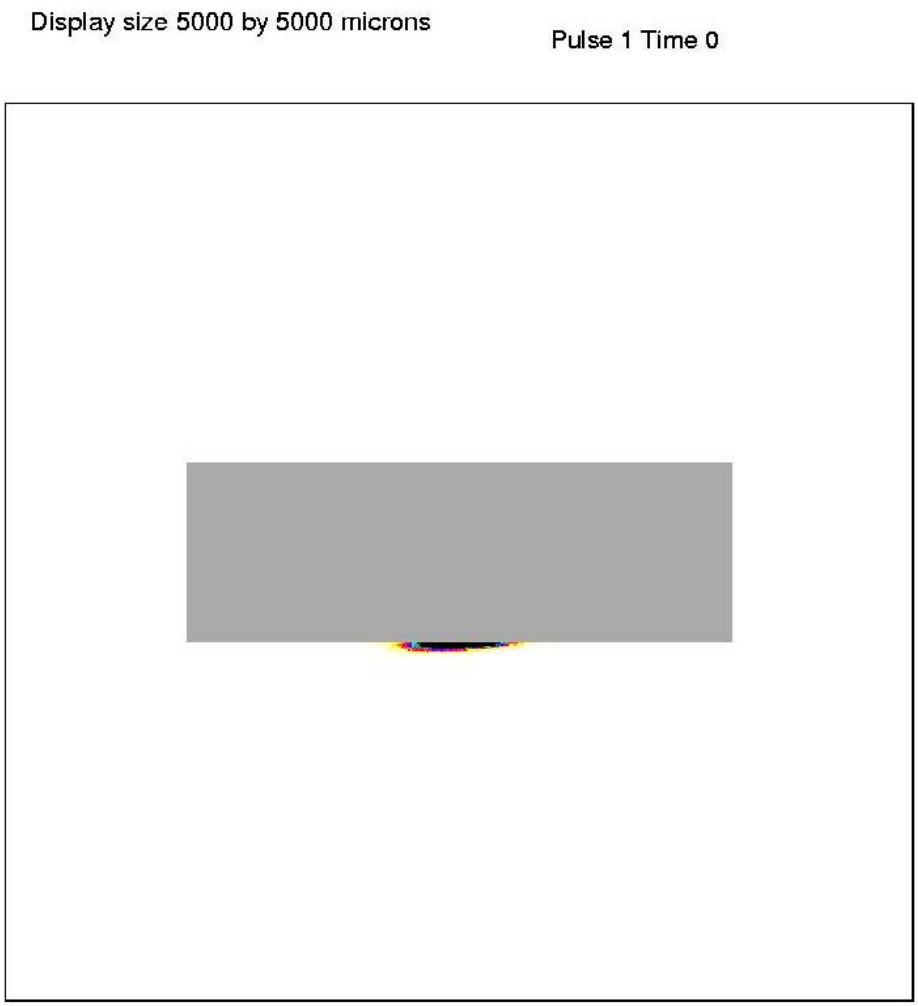

Figure 6.19: An image of the spoiler with the shaded area representing the aperture. At t=0 ns, the spoiler is hit by one bunch. The initial temperature of the spoiler is 300 K.

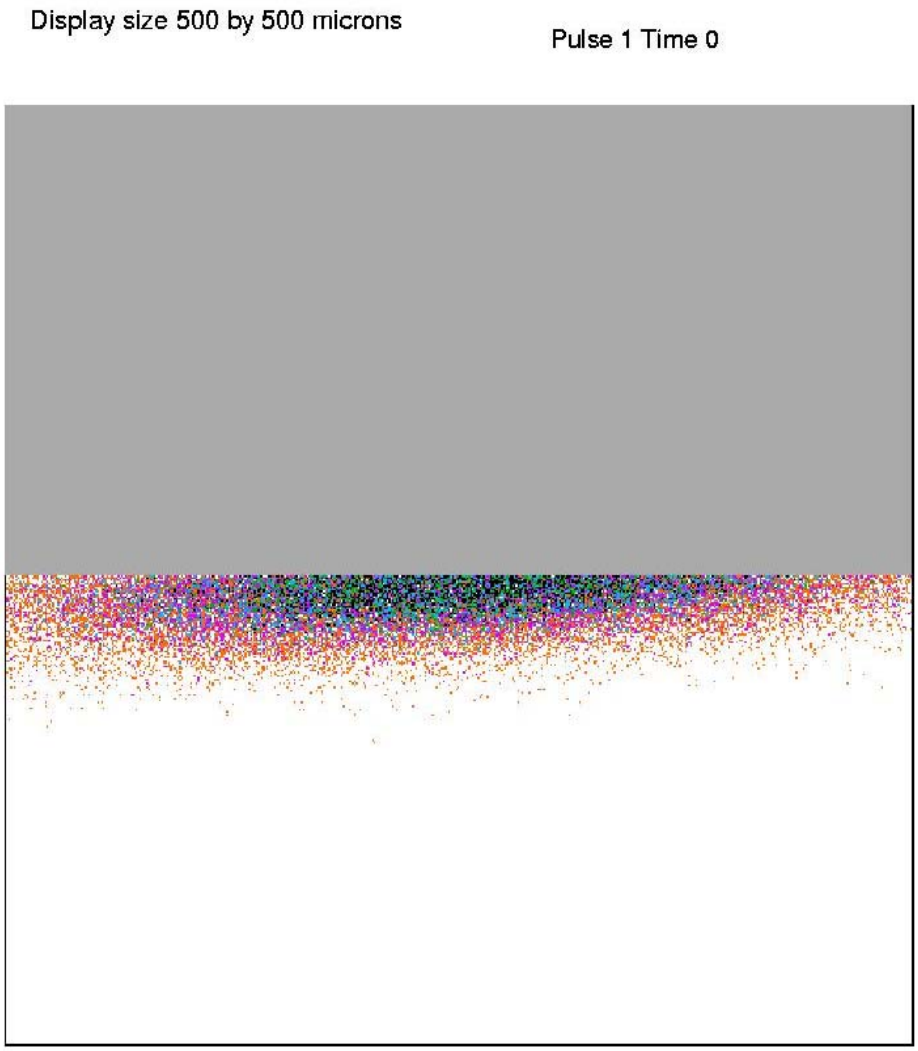

Figure 6.20: A magnified image of the same spoiler at t=0 ns when it is hit by one bunch. The temperature distribution has initially a fine grained-structure.

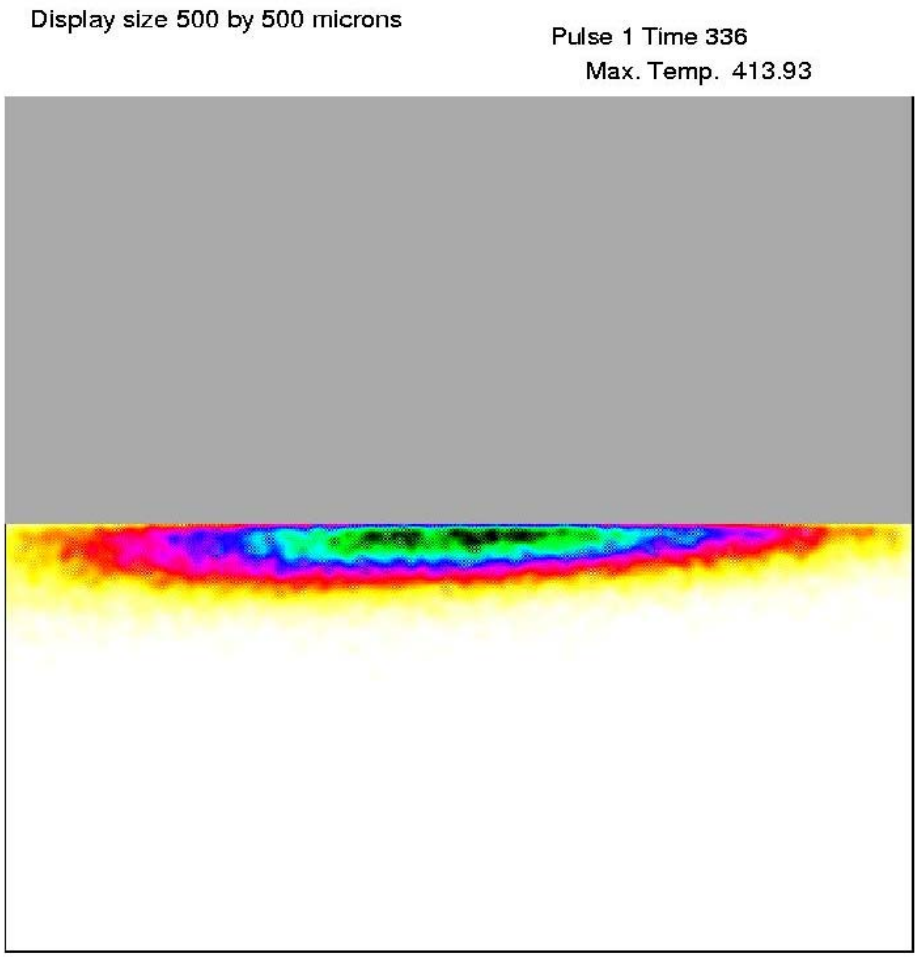

Figure 6.21: The fine grained-structure of figure 6.20 is blurred out by thermal conduction before the spoiler is hit by a second bunch (t=336 ns). The initial temperature of 300 K has increased to T = 413.93 K (the black spots).

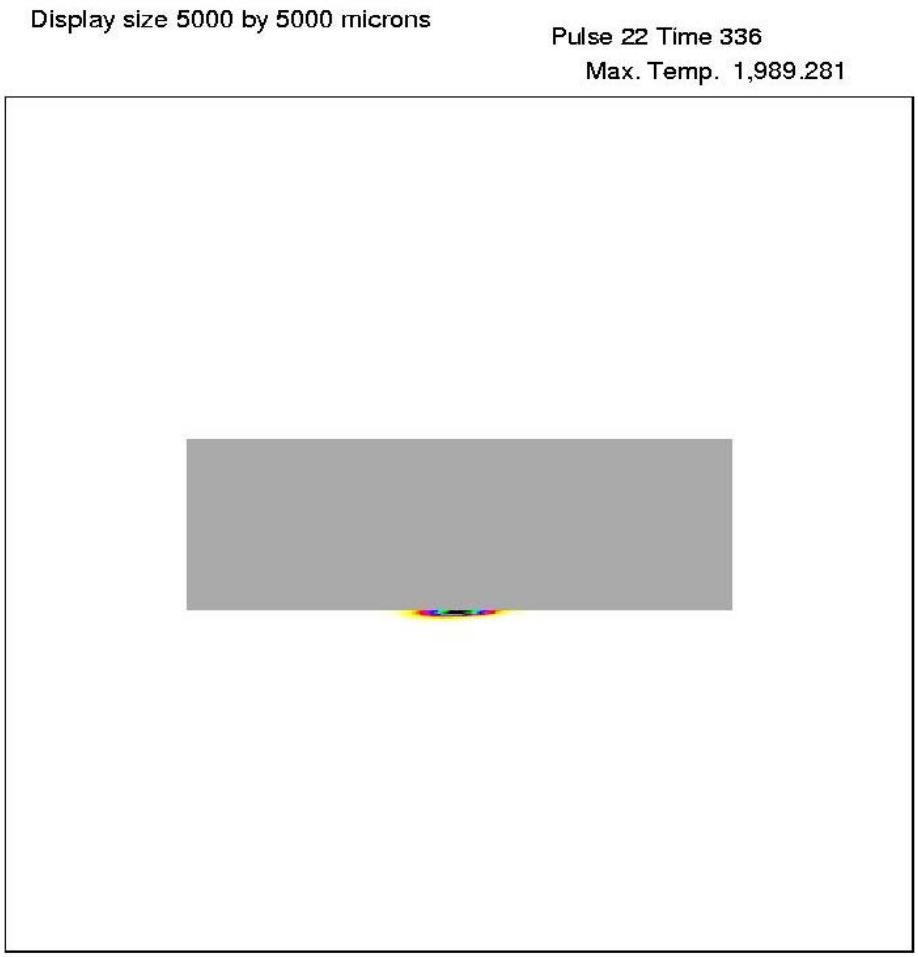

Figure 6.22: The temperature distribution on the spoiler after it has been hit by 22 bunches. The repeated effects of energy deposition and thermal difussion led to a maximum temperature of 1989 K. The melting temperature for titanium is 1933 K, so the beam will melt an area in the collimator.

Chapter 7

Scattering Effects through the Spoilers

For the remainder of the analysis conducted in this study, the last step was to include the effects of Coulomb scattering in the code. Scattering processes were not included initially in "MERLIN", therefore a realistic analysis of the particles which strike the collimators can not be possible without taking this effect into consideration. A large number of particles are scattered and collected in the absorbers, but other particles may continue onwards due to the small scattering angles and random output direction.

This chapter covers the mathematical treatment of multiple scattering through small angles and shows how this approach was implemented in the "MERLIN" code. The particle distributions at the exit of the BDS with and without scattering processes applied in the program are compared. The chapter ends with an analysis of the energy loss from the scattered particles.

7.1 Multiple Coulomb Scattering

The theory of the multiple scattering of charged particles has been treated by several authors, and references [80], [81] and [82] contain detailed accounts of the scattering

mechanism and mathematical approach. There are at least four different theories which are closely related: the theories of Molière, Snyder and Scott, Goudsmit and Saunderson, and of Lewis. The first two are mathematically closely related and use the approximation of small scattering angles and therefore an expansion in Bessel functions. Goudsmit and Saunderson develop a theory valid for any angle by means of an expansion in Legendre polynomials. Lewis starts from the Legendre expansion and then goes over to the limit of small angles, thus establishing the connection between the first three methods [80]. However, the mathematical treatment of the theory of multiple scattering is beyond the scope of this study and only a qualitative review of the differential scattering probability will be given next.

A charged particle which passes in the neighbourhood of a nucleus undergoes a large number of collisions which produce very small angular deflections. As a result of these successive collisions, the particle will perform a random walk as it proceeds, and will emerge from the material with a given lateral displacement and a given angular deflection (figure 7.1).

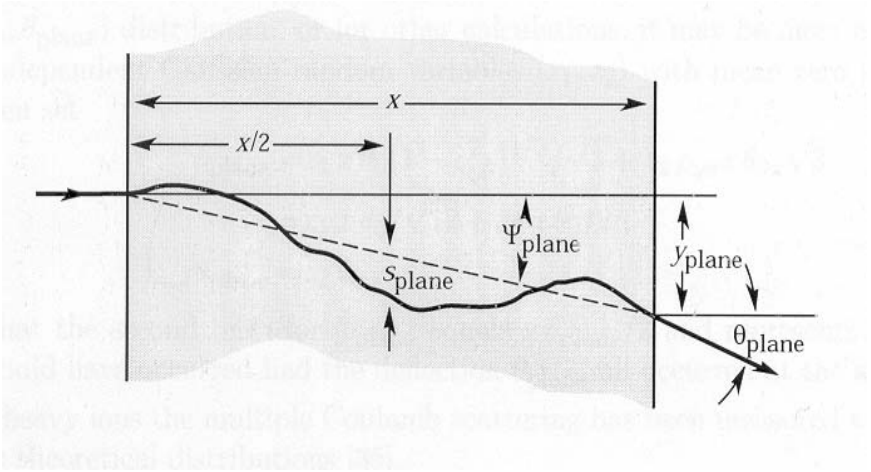

Figure 7.1: Quantities used to describe multiple Coulomb scattering. The particle is incident in the plane of the figure (adapted from [86]).

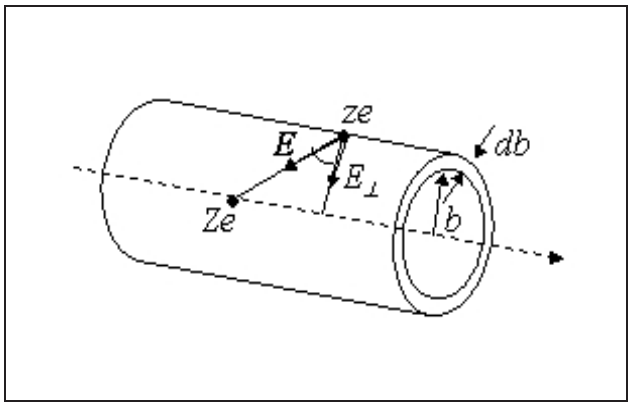

Figure 7.2: Transfer of momentum to a charge e passing near a heavy nucleus of charge Ze.

Consider an electron traversing matter of atomic number Z. Occasionally, the electron will collide elastically with a nucleus and will be scattered. In the process of scattering due to the Coulomb force, the transverse impulse given to the rapidly moving incident electron against a nucleus of charge Ze is:

$$\Delta p_\perp = \int_{-\infty}^{\infty} eE_\perp dt = \int eE_\perp \frac{dx}{v} \tag{7.1}$$

where v is the velocity of the particle and $E_\perp$ is the transverse component of the electric field. The integral can be easily calculated by applying Gauss' theorem to the cylinder of radius b (figure 7.2):

$$\phi = \int E_\perp 2\pi b dx = 4\pi Ze \tag{7.2}$$

Replacing the second integral of equation 7.1 by its value obtained from equation 7.2, one can obtain:

$$\Delta p = \frac{2Ze^2}{bv} \tag{7.3}$$

This represents the momentum acquired by the electron in a direction perpendicular to its initial trajectory. If the electron has an initial momentum p, its trajectory is deflected by an angle θ given by the equation [85]:

$$\theta = \frac{\Delta p}{p} = \frac{2Ze^2}{bvp}. \tag{7.4}$$

Rutherford evaluated the probability of a deflection between θ and $\theta+d\theta$ with impact parameter in db at b, where θ and b are related by equation 7.4. The probability of a collision with impact parameter in db at b is [85]:

$$\Xi(\theta)d\theta = \frac{N}{A}2\pi b\, db = \pi\frac{N}{A}\, d(b^2) \tag{7.5}$$

where N is the number of nuclei per unit volume and A is the atomic mass number. Equation 7.4 gives in absolute value:

$$d(b^2) = \left(\frac{2Ze^2}{vp}\right)^2 \frac{2d\theta}{\theta^3} \tag{7.6}$$

Hence the probability of a scattering in $d\theta$ at θ has the expression:

$$\Xi(\theta)d\theta = \pi\frac{N}{A}\left(\frac{2Ze^2}{vp}\right)^2 \frac{2d\theta}{\theta^3} \tag{7.7}$$

For sufficiently small angles, the solid angle $d\omega$ may be written as $2\pi\theta d\theta$ and the differential scattering probability becomes [85]:

$$\Xi(\theta)d\omega = \frac{N}{A}\left(\frac{2Ze^2}{vp}\right)^2 \frac{d\omega}{\theta^4} \tag{7.8}$$

This is known as the Rutherford scattering formula. At the limit $\theta = 0$, the scattering probability density tends to infinity.

Rutherford has treated the scattering due to the Coulomb force of a single nucleus acting on a charged particle. In addition to this single scattering, the cumulative effect of many small nuclear scatterings that produce a deviation θ from the initial direction of the particle has to be taken into account. For multiple very small scattering angles, the probability of finding a deviation between θ and $\theta + d\theta$ is considered to be described by a Gaussian distribution [84]:

$$P(\theta)d\theta = \frac{e^{-\frac{\theta^2}{\langle\theta^2\rangle}}}{(\pi\langle\theta^2\rangle)^{1/2}}d\theta \tag{7.9}$$

The value for $\langle\theta^2\rangle$ was calculated by Rossi [85]. He measured the thickness x in radiation lengths X_0 and found an expression for $\langle\theta^2\rangle$ (θ expressed in radians) with $E_s = 21{\cdot}10^6$ eV.

$$\langle\theta^2\rangle = \left(\frac{E_s}{vp}\right)^2 \frac{x}{X_0} \tag{7.10}$$

To summarise, a charged particle traversing a medium is deflected by many small-angle scatters. Most of these deflections are due to Coulomb scattering from nuclei, and hence the effect is called multiple Coulomb scattering (however, for hadronic projectiles, the strong interactions also contribute to multiple Coulomb scattering). The Coulomb scattering distribution is well represented by the theory of Molière. It is roughly Gaussian for small deflection angles, but at larger angles (greater than a few θ_0 defined in equation 7.11), it behaves like Rutherford scattering, having larger tails than does a Gaussian distribution [86]. This is illustrated in figure 7.3.

The net scattering angle - the angle measured between the entering and exiting track - (figure 7.1) represents the sum of all individual scattering events and was obtained from a fit to Molière distribution for charged particles with β=1 for all Z, and is accurate to 11% or better for $10^{-3} < x/X_0 < 100$ [86]. The horizontal and vertical rms net scattering angles are [86]:

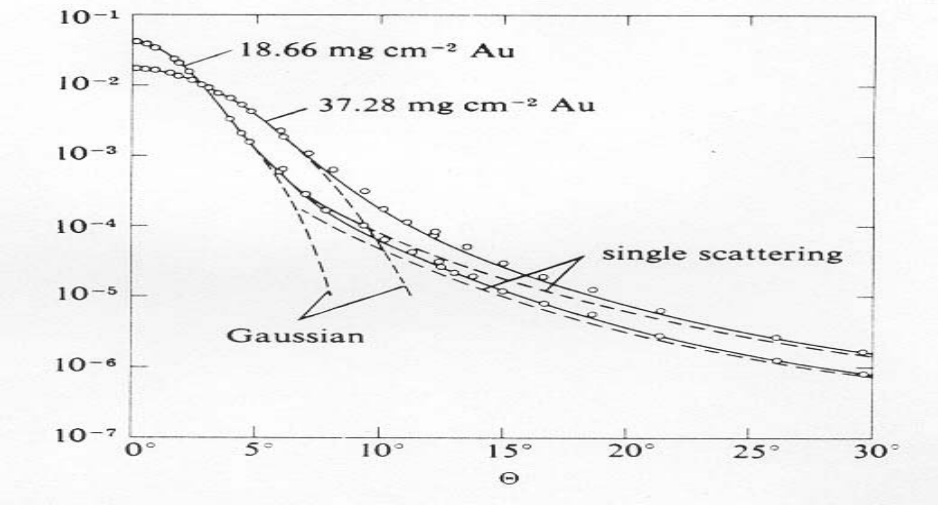

Figure 7.3: Angular distribution of electrons scattered from Au at 15.7 MeV. Solid lines indicate the distribution expected from the Molière theory for small- and large-angle multiple scattering, with an extrapolation in the transition region; dash lines, the distributions according to the Gaussian and single-scattering theories (adapted from [84]) .

$$\theta_0 = \frac{13.6MeV}{\beta cp} z \sqrt{\frac{x}{X_0}} \left[1 + 0.038\, ln \left(\frac{x}{X_0} \right) \right] \tag{7.11}$$

where p, βc, and z are the momentum, velocity and charge number of the incident particle and x/X_0 is the thickness of the scattering medium in radiation length.

The projected (plane) angular distributions $\theta_{plane,x}$ and $\theta_{plane,y}$ onto two planes orthogonal to the direction of motion are independent and identically distributed. For Monte Carlo generation of a joint $(y_{plane}, \theta_{plane})$ distribution or for other computer calculations - in this case, the "MERLIN" code - it is convenient to work with independent Gaussian random variables (z_1, z_2) with mean zero and variance one, and then set [86]:

$$y_{plane} = z_1 x\theta_0(1-\rho_{y\theta}^2)^{1/2}/\sqrt{3} + z_2\rho_{y\theta}x\theta_0/\sqrt{3} \quad (7.12)$$

$$= z_1 x\theta_0/\sqrt{12} + z_2 x\theta_0/2 \quad (7.13)$$

$$\theta_{plane} = z_2\theta_0. \quad (7.14)$$

where $\rho_{y\theta}$ is the correlation coefficient between the co-ordinate scatter y and the angle of scatter θ and has the value $\rho_{y\theta}=\sqrt{3}/2 \approx 0.87$.

Equation 7.11 describes scattering from a single material type, while in practice we often have to consider multiple scattering of a particle traversing many different layers and mixtures. Since the expression of θ is obtained from a fit to Molière distribution, it is incorrect to add the individual θ_0 contributions in quadrature; the result is systematically too small. It is much more accurate to apply equation 7.11 once, after finding x and X_0 for the combined scatterer [86].

A charged particle moving through a spoiler loses energy as a consequence of collisions with atomic electrons. For a spoiler of one radiation length, the average particle energy on exit is $1/e$ of its initial energy which represents 92.25 GeV for a beam having an initial energy of 250 GeV. The energy loss in the spoiler is due mainly to radiation according to equation 6.6 ($E > E_c$ with $E_c \approx 27.27$ MeV for a titanium spoiler) and only a small fraction of energy loss is due to collisions with the atomic electrons. This small fraction of energy can be calculated using the energy loss per unit length of 6.701 MeV/cm given in section 6.4.3 and the width of a TESLA spoiler which is 3.56 cm [19] and the computation gives $\simeq 0.024$ GeV.
If L is the length of the spoiler in radiation lengths ($r.l.$), the exact spectrum in $\delta = -\Delta p/p$ can be estimated from [85] [35]:

$$\frac{1}{N}\frac{dN}{d\delta} = \frac{ln\left(\frac{1}{1-\delta}\right)^{\frac{L}{ln2}}}{\Gamma\left(\frac{L}{ln2}\right)} \quad (7.15)$$

The particle momentum is lowered after passage through the spoilers and figure 7.4 shows the spectrum obtained using equation 7.15 with L=1 $r.l.$, $\delta = x$ and $1/\Gamma(L/ln2) = 1.1287$. The values from this graph were used in order to construct an algorithm to lower the momentum of the scattered particles in the "MERLIN" code.

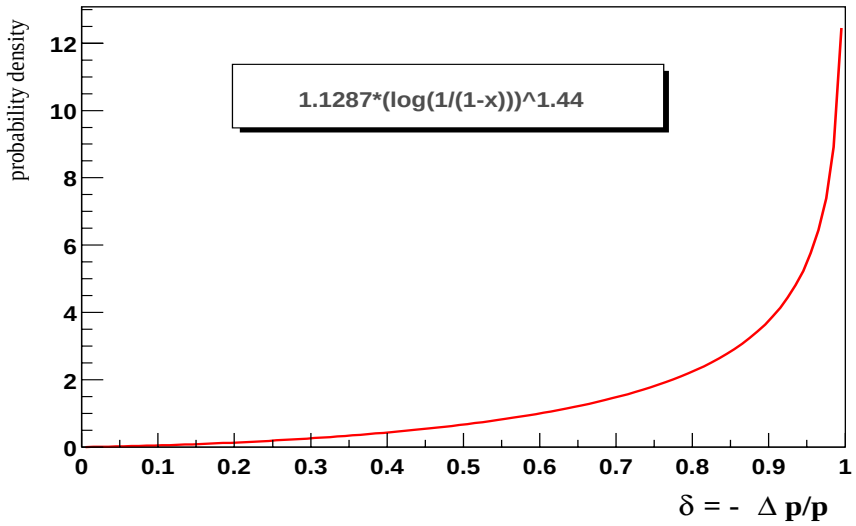

Figure 7.4: The integrated δ = -$\Delta p/p$ spectrum for a one radiation length.

7.2 Coulomb Scattering in the "MERLIN" Code

Having given the theoretical framework for small scattering angles, the implementation of the scattering process in the computer code is described next.

As mentioned in section 4.1, the most powerful feature of OOP is the program partitioning into a set of classes which can be used by a large number of people without modifying them. However, there are cases when the existing library is not suited to a particular situation and the programmer must create new classes adapted to

work in the new situation. The Coulomb scattering of high energy electrons in the TESLA spoilers was such a case as will be shown next.

When creating a new class, instead of writing completely new data members and new member functions, the programmer can designate that the *derived class* is to *inherit* the behaviour and the attributes from a previously defined *base class*. The derived class can add then data members and data functions of its own. One can say that the class library is constructed from standardized reusable classes just as hardware is constructed from reusable components [83].
The "MERLIN" code provides a class **CollimateParticleProcess** which collimates the particles by reading the aperture of each element and by scraping off the particles which are found outside this aperture. These particles are deemed lost (section 4.3). As mentioned in section 5.2.2, the spoilers are located close to beam having tight apertures (Table 5.4). They are struck by a large number of particles compared to rest of the elements and their aim is to protect other components from a direct hit by increasing the beam angular divergence. Therefore, a class **Scattering** derived from the base class **CollimateParticleProcess** was created to apply a position and angle displacement to the particles found outside the spoilers' aperture.

7.2.1 The Class Interface

When writing a new class, the programmer must take into account a basic principle of software engineering: the separation of interface from implementation [49]. This means that the class declaration is placed in a header file (ie. *Scattering.h*) and this represents the class *interface*, and the definitions of class member functions are placed in a source file (ie. *Scattering.cpp*). This represents the *implementation* of the class. The users do not need to know the implementation details, the interface must supply all the information needed.

The interface of the class **Scattering** is presented in Appendix A. The One-Definition

Rule (ODR) of a C++ program says that a given class must be defined exactly once in a program [47]. But for larger codes - and the "MERLIN" code is such an example - a class may be included in more than one source file. This means that the class **Scattering** could be included in other classes in the future, as the "MERLIN" code is continually improved and extended. Should the compiler be presented with *Scattering.h* more than once during a compilation may lead to errors. To avoid this, *include guards* (*#ifndef*, *#define*, *#endif*) are used. Therefore, if the content of the file *Scattering.h* between *#ifndef* and *#endif* is seen for the first time, it is defined by using the *include guard* *#define*. If the content of the file is seen again, it is ignored.

Because the C++ codes are organised into a set of semi-independent files, the *#include* mechanism is used to get their interface into a single file for compilation to ensure consistency. The statements:

```
#include "BeamDynamics/ParticleTracking/CollimateParticleProcess.h"
#include "NumericalUtils/Utils.h"
```

replace the above lines with the contents of both files via the *#include* mechanism. The source code is read by the compiler and then linked together.

The class **Scattering** is derived from the class **CollimateParticleProcess** as was shown previously. It inherits the public and protected members of the base class but it can not use the private members [49]. The inheritance is specified in the following line:

```
class Scattering:public CollimateParticleProcess
```

The colon in the class declaration indicates inheritance and the keyword *public* indicates the type of inheritance. With *public* inheritance, every object of a derived class may also be treated as an object of that derived class' base class and all the *public* and *protected* members of class **CollimateParticleProcess** are inherited as *public* and *protected* members of class **Scattering**.

The class body is separated into two parts: the *public* part constitutes the public interface to objects of the class while the *private* part can be used only by class member functions. By restricting access to a private data of a class, C++ protects against accidents rather than deliberate fraud [47]. The public part contains the constructor and the destructor of the class and the function *Energy Loss()*. The constructor is called whenever an object of the class **Scattering** is created and is used to initialize its data members:

Scattering (double, double, int, int, std::ostream∗);

The destructor is called when an object of class **Scattering** leaves scope and the memory allocated must be released after use:

∼ Scattering ();

The function *double EnergyLoss()* is used to calculate the momentum loss $\delta = -(p' - p)/p$, where p is the initial momentum of the particles and p' is the final momentum after passing through the spoilers. The private function *void DoScattering()* is used to apply a position and angle deviation to particles found outside the spoilers' aperture and also to lower their momentum. The function *void DoProcess(double df)* performs the scattering process during particle tracking for the specified step *df*. All these functions will be discussed in detail in part B) of the next section. The file *Scattering.h* ends with a list of data members used by the member functions of the class.

7.2.2 The Class Implementation

The implementation of the class **Scattering** is presented in Appendix B. The source file *Scattering.cpp* uses the interface information presented in the class header file, so the header file must be included. It also uses the standard library facilities and an appropriate header is included to complete the program:

```
#include <fstream>
using namespace std;
```

Because some data is read from a file called *EnergyLoss.txt* (see function *EnergyLoss()*), the header <fstream> is included as it contains function prototypes for functions that perform input from files on disk and output to files on disk. The facilities are provided in the *std* namespace and their names are bring into the global namespace by using the statement *using namespace std*.

When writing a derived class, it is possible that some derived-class functions have the same name as the base-class functions and to avoid such ambiguity for the compiler, the functions of class **Scattering** are preceded by their class name and the *scope resolution operator*::. A special attention will be given to functions *DoScattering()*, *EnergyLoss()* and *DoProcess()*.

A) The Function DoScattering()

The function *DoScattering()* applies a displacement in position and angle to particles found outside the spoilers' collimation aperture and lowers their momentum after passing through the spoilers' material (section 7.2.1). The function reads first the aperture of each component of the BDS lattice and applies a sequential index (1..n) to particles, as indexing allows particles to be traced back to the original coordinates [51]. The index values for each particle are then maintained and output during any particle output operation as the first column.

```
const Aperture *ap = currentComponent->GetAperture();
PSvectorArray PSscat;
list<size_t>::iterator ip;
if (pindex!=0)
ip =pindex->begin();
```

Coulomb scattering is applied to particles found outside the CDS or CCS spoilers tight aperture because they are more likely to be hit (section 5.2.2):

```
if ("ESPOI"== currentComponent->GetName()|| "XYSPOI"==
currentComponent->GetName() || "COLX" == currentComponent
->GetName()|| "COLY"== currentComponent->GetName() ){
for (PSvectorArray::iterator p = currentBunch->begin(); p!=
currentBunch->end();p++)
if(!ap -> PointInside( p->x(),p->y(),s ))
```

Equation 7.13 is implemented next. The values of $1/\sqrt{12}$ and $1/2$ are assigned to the variables $n1$ and $n2$. The function *normal()* belongs to the class **RandomNG** and is called to generate a random number from a normal (Gaussian) distribution with the specified mean (0.0) and variance (1.0). The value of the random number is assigned to the variables $z1x$ and $z2x$.

The class **Scattering** may be used by other programmers to apply a position and angle displacement to other types of spoilers having a different width and scattering angle θ_0. Therefore, the corresponding values for width x and angle θ_0 in equation 7.13 are not defined in the class implementation as constants. Their values for TESLA spoilers are passed from the application (the program which contains the *main()* function) to the class **Scattering** where they are used in function *DoScattering()*. The data members *width* and *theta* are initialized with these values by the constructor. The code fragments are presented below:

```
const double n1 = 0.288; // 1/sqrt(12)
const double n2 = 0.5; // 1/2
double z1x = RandomNG::normal(0.0,1.0);
double z2x = RandomNG::normal(0.0,1.0);
p->x() += z1x*width*theta*n1 + z2x*width*theta*n2;
p->xp()+= z2x*theta;
```

The same argument applies also to the position and angle deviation in the vertical plane as the projected (plane) angular distributions $\theta_{plane,x}$ and $\theta_{plane,y}$ onto two planes orthogonal to the direction of motion are independent and identically distributed (section 7.1). The function *normal()* of class **RandomNG** is called again

to generate other random numbers and their values are assigned to variables $z1y$ and $z2y$:

```
double z1y = RandomNG::normal(0.0,1.0);
double z2y = RandomNG::normal(0.0,1.0);
p->y() += z1y*width*theta*n1 + z2y*width*theta*n2;
p->yp()+= z2y*theta;
```

One can see that if the particles are found outside the aperture of one of the CDS or CCS spoilers, they are scattered by adding to their vector components (x, xp, y, yp) the calculated displacements in position and angles.
The particles which strike elements other than spoilers do not undergo scattering and are deemed lost:

```
else
DoCollimation()
```

The function *DoScattering()* also lowers the particle momentum after passing through the collimators by calling the function *EnergyLoss()*. Therefore, it is useful to describe first the algorithm used by this function and its implementation in the computer code.

B) The Function EnergyLoss()

The algorithm used the values from graph 7.4. The probability density was calculated for various values of δ by dividing the horizontal axis in small intervals (in this case choosing 50 intervals each having a corresponding probability density P_i). The middle of each interval was considered to be the δ value associated with the corresponding probability density (ie. for the interval $\delta \in [0, 0.02]$, the probability density P_1 corresponds to an energy loss of 1%). The probability density can be calculated by integrating equation 7.15 for each interval.
If one chooses to represent the probabilities P_i on a horizontal axis where $P1$, $P2$, $P3$ ...Pn represent the length of each segment, their sum should be 1. The values

in each point A, B, C etc. are: $A = P1$, $B = P1 + P2$, $C = P1 + P2 + P3$ and so on (figure 7.5).

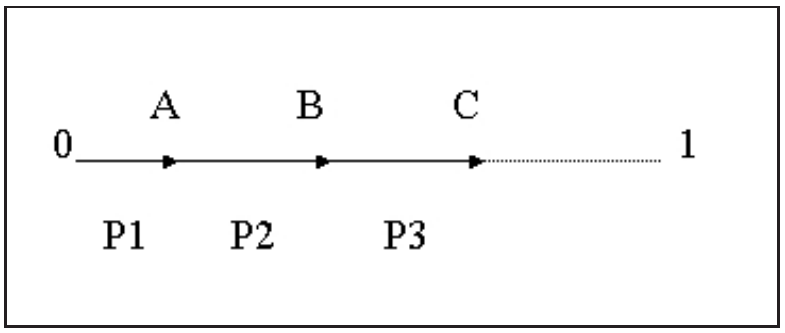

Figure 7.5: A representation of the sum of probability densities.

The program generates a random number within the interval [0,1]. The probability for that number to be in a given interval on the axis is the length of that segment divided by the total length. In the computer program one may say that if the value of a random number generated is greater than the value in a point $x(i)$ and smaller than the value in a point $x(i+1)$ the probability density is P_{i+1}. Therefore, both the energy loss (in %) and the values of points A, B, C etc. are recorded in a file which is read by the "MERLIN" code.

The implementation of this algorithm is given next. The values for energy loss in % (it is an integer in the file but will be multiplied with 0.01 in the function) and $\sum_{i=1}^{n} P_i$ are read from the file *EnergyLoss.txt*. The values are recorded in two arrays $x[n]$ and $y[n]$ declared *static*. The reason is that each time a random number is generated in the interval $y[j] < RNG < y[j+1]$, the energy loss is found from the arrays each time the function is called, but the data is read from the file into the arrays only on the first time. The value is then multiplied with 0.01 and stored. The random number is generated by calling the function *uniform()* from class **RandomNG** which returns a number in the interval (0, 1).

```
double Scattering::EnergyLoss(){
```

```
const int n=49;
static int x[n];
static double y[n];
static bool firsttime = true;
if(firsttime){
ifstream fromfile("EnergyLoss.txt");
for(int i=0; i<50; i++){
fromfile>>x[i]>>y[i];}
firsttime=false;}
double RNG = RandomNG::uniform(0.0,1.0);
for(int j=0; j<50; j++)
if(( y[j]<RNG ) && ( RNG<y[j+1] )){
double delta = 0.01 * x[j+1]; } }
return delta;}
```

The variable *delta* returned by the function represents the momentum loss by the particles in a scattering medium $\delta_G = -(p' - p)/p$. In this relation, p is the initial particle momentum and p' is the final momentum after passing through the spoiler. The result returned by the function *EnergyLoss* is assigned to a variable *deltaG* in the function *DoScattering()*.

It was stressed previously that δ in the "MERLIN" code is given by the relation $\delta = (p - p_0)/p_0$, where p is the initial particle energy and p_0 the design energy (section 4.2.1). This value is stored in the variable *deltaN* in the function *DoScattering()*. After passing through the collimators the previous relation can be written as $\delta' = (p' - p_0)/p_0$ where p' is the final particle momentum. Combining these three expressions one can obtain the relative momentum δ' after passing through the collimators ($p- > dp()$ in the function).

```
double deltaN = p->dp();
double deltaG = EnergyLoss();
p->dp() = deltaN*( 1-deltaG) - deltaG;
```

C) The Function DoProcess()

During a tracking operation, for an element situated between $s, s+\Delta s$ in the lattice where s is the coordinate along the path (section 3.3.1), the scattering process is performed by the function *DoProcess()*. When the process is finished, the total length of the lattice travelled by the bunch is updated by calling the function *SetNextS()*. The scattering process is then applied to the next element by calling the function *DoScattering()*:

```
void Scattering::DoProcess(double df){
f += df;
if (fequal(f, next_f)){
DoScattering();
SetNextS();}
}
```

The purpose of applying scattering in the "MERLIN" code was to study first the distribution of large amplitude particles at the final doublet and the following section will present the results.

7.3 Halo Distribution at the Final Doublet

A simulation of a flat halo of $\pm 13\sigma_x$ and $\pm 80\sigma_y$ plus 25% increase over collimation depth and containing 10^5 particles was sent out of the linac. The particles had an energy of 250 GeV and an energy spread of (-3%, 0.5%). Initially, the effects of scattering and transmission through material were not included. Figure 7.6 shows the spatial particle distribution at the entrance of the final doublet and one can see that the particles are collimated correctly, as the beam halo is enclosed within the collimation depth of $\pm 13\sigma_x$ and $\pm 80\sigma_y$.

The situation is different when the scattering is applied to the simulation code. After the interaction with the spoilers in the primary and secondary collimation system, a number of scattered particles are intercepted by other elements in the lattice and are lost. Other halo particles survive and can proceed onwards due to the very small θ angle and their corresponding outgoing arbitrary direction. These are the particles that are expected to hit the final doublet outside the collimation depth, and the beam loss distribution is presented in figure 7.7. With scattering applied, there are 7899 particles compared to 4784 in the first case. Due to their dispersive trajectories after passing through the spoilers material, these particles are outside the collimation depth of $\pm 13\sigma_x$ and $\pm 80\sigma_y$.

The particle distribution at the entrance of the final doublet after tracking through the entire BDS is shown in figures 7.8 and 7.9 for the horizontal and vertical plane respectively. Effects of scattering and transmission through material are not included. One may see that the halo particle distribution is enclosed within a transverse extent of $\pm 13\sigma_x$ (figure 7.8) and $\pm 80\sigma_y$ (figure 7.9).
Then scattering was applied in the simulation code and the particle distribution at the end of the BDS is illustrated in figures 7.10 for the horizontal plane and 7.11 for the vertical plane. One important result is borne out in these two plots: from the figures, one can observe that both histograms have a longer tail and it is clear that there are particles outside the collimation depth of $\pm 13\sigma_x$ and $\pm 80\sigma_y$. This demonstrates the importance of reconsidering the collimation depth at the final doublet, otherwise it is expected a significant background in the physical detector.

Figures 7.12 and 7.13 show the results for momentum before and after scattering was applied in the code. One may see that in figure 7.12 the momentum distribution is within (-3% and +0.5%) and the total number of particles at the final doublet is 4784. After scattering was applied, the momentum distribution is within the same values (-3% and +0.5%), but there are more particles at the final doublet which lose a fraction of their initial energy as the distribution has a longer tail.

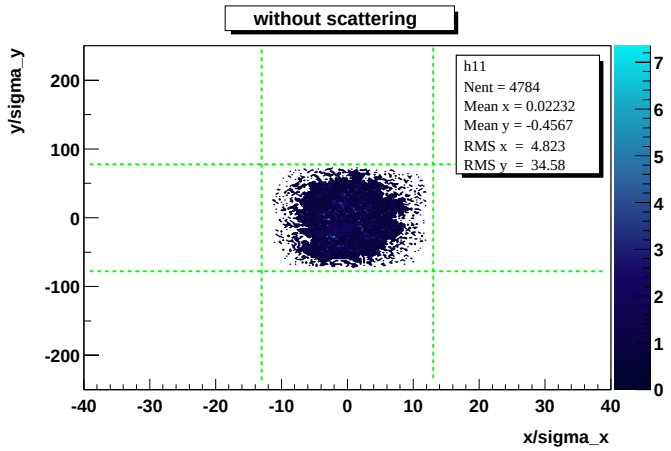

Figure 7.6: Without scattering, from a total of 10^5 halo particles at the entrance of the BDS, 4784 particles arrive at the final doublet; they are kept within the collimation depth of $\pm 13\sigma_x$ and $\pm 80\sigma_y$.

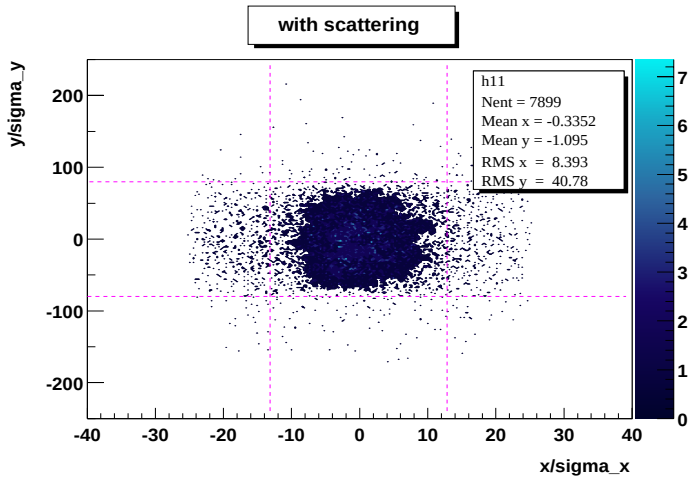

Figure 7.7: With scattering applied, from a total of 10^5 halo particles , 7899 particles arrive at the final doublet; 6726 particles are inside the required collimation depth of $\pm 13\sigma_x$ and $\pm 80\sigma_y$; the remaining 1173 particles are outside the collimation depth.

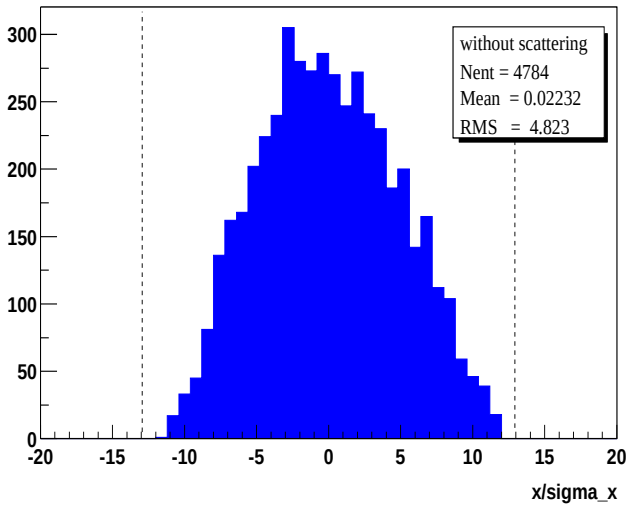

Figure 7.8: Results of halo particle tracking through the BDS; the particle distribution is within the collimation depth of $\pm 13\sigma_x$ near the final doublet.

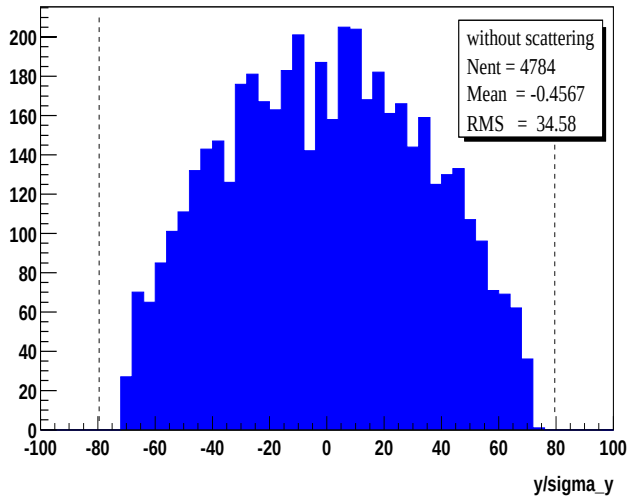

Figure 7.9: The halo particle distribution is within the collimation depth of $\pm 80\sigma_y$ after tracking through the entire BDS lattice to the final doublet.

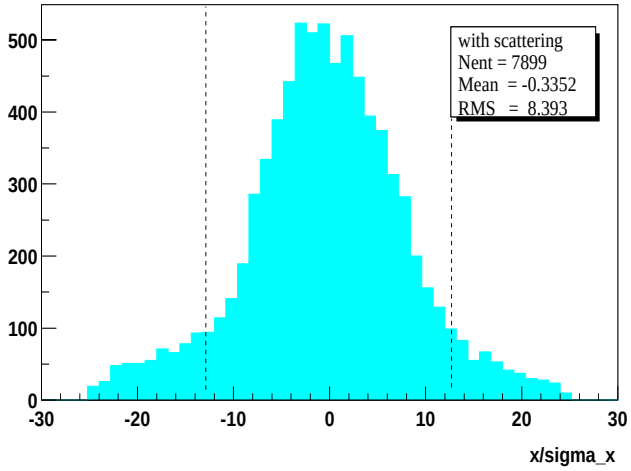

Figure 7.10: The halo particle distribution in the horizontal plane with scattering; the particle distribution is outside the collimation depth of $\pm 13\sigma_x$.

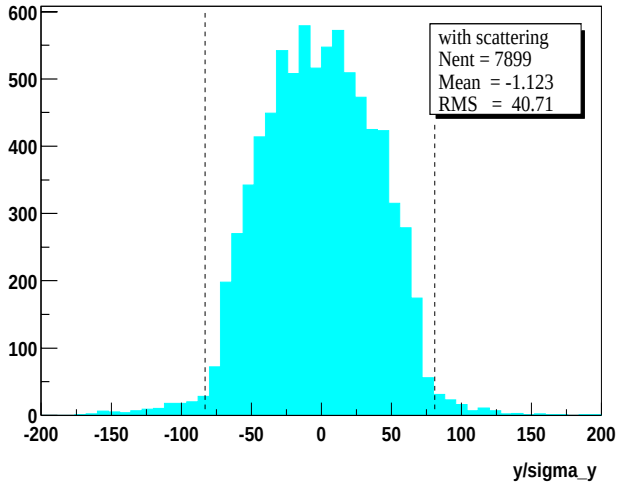

Figure 7.11: The halo particle distribution in the vertical plane with scattering; the particle distribution is outside the collimation depth of $\pm 80\sigma_y$.

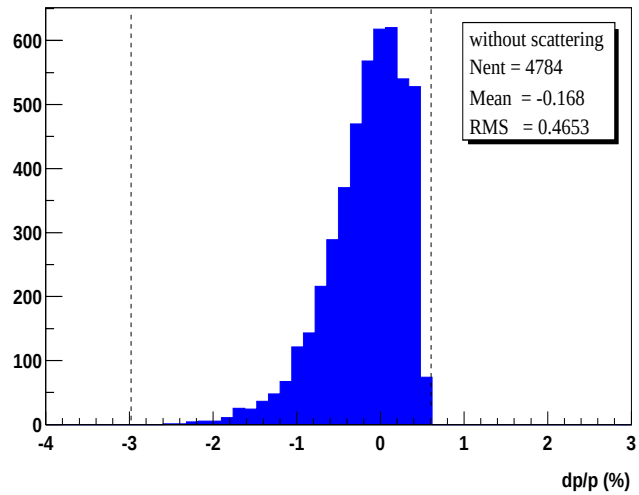

Figure 7.12: The momentum distribution for halo particles is within -3% and +0.5%. The scattering effects are not applied in this case.

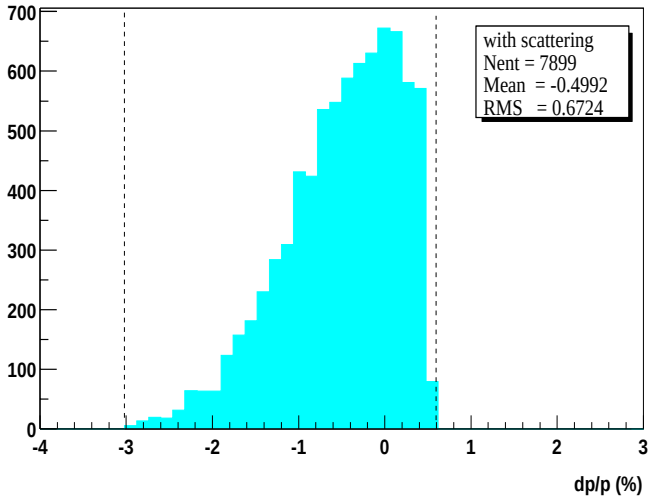

Figure 7.13: The momentum distribution for halo particles after scattering was applied is still within -3% and +0.5%, but there are more particles which lose energy.

7.4 The Absorbers

Although the spoilers' survival is difficult to guarantee if one of them is hit head-on by a highly energetic beam, the absorbers should be more safe. The beam size of a beam which strikes an absorber situated at a distance L downstream of the spoiler is [63]:

$$(\sigma_x \sigma_y)_{absorber} \sim L^2 \theta_0^2 \tag{7.16}$$

where θ_0 represents the Coulomb scattering angle. Choosing the distance L large enough, it is possible to obtain a beam size of a few square millimeters, adequate to guarantee absorber survival.

While the exact position of the absorbers is still to be determined, a simulation of a halo containing 10^5 particles was sent through the BDS until the final doublet. Due to scattering effects, the particles are lost in a large number of elements (179) but the particle deposition is less than 0.1% for the majority of elements. However, significant losses occur in four drift spaces called Drift.DCBC3 situated downstream the CDS spoilers: at 771.878 m (36% particles), at 871.559 m (31% particles), at 971.240 m (13% particles) and 1070.920 m (4% particles) (figure 7.14). The particle deposition on the elements after scattering through the CCS spoilers is less than 0.1% and there are not significant losses in the drifts.

In conclusion, only a few areas will be struck by a large number of particles and these areas can be identified and fitted with proper absorbers. The exact position of the absorbers in these regions is still to be determined.

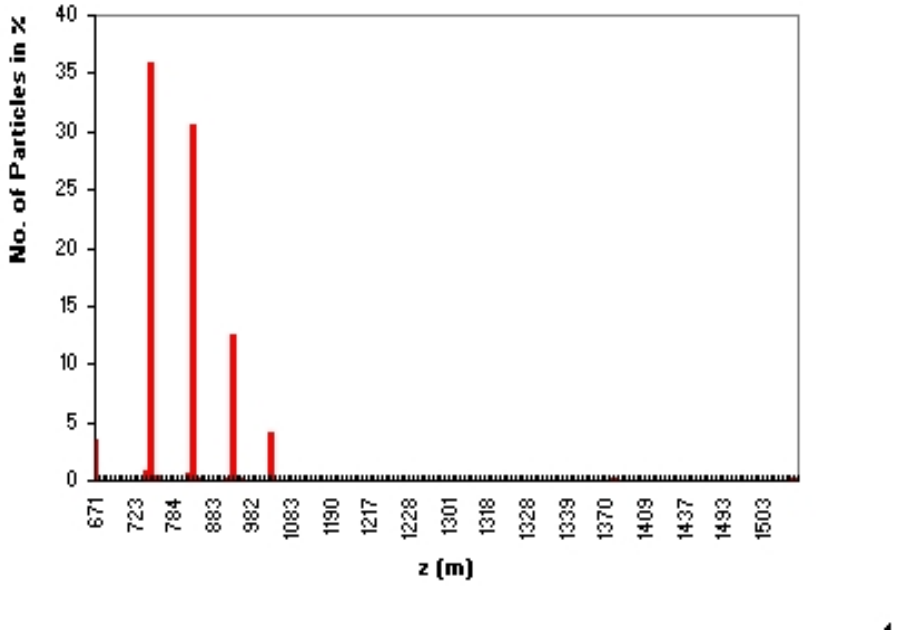

Figure 7.14: Particles losses along the beamline with scattering effects applied.

Chapter 8

Conclusions and Analysis

In order to obtain a high luminosity at the interaction point of order $\approx 10^{34} cm^{-2} s^{-1}$, a small transverse emittance is required. However, the emittance is difficult to preserve during acceleration through the main linac and is diluted due to various effects. The vertical emittance growth was calculated: wakefield effects give 13.5% emittance growth, betatron coupling gives a smaller value of 0.25%, while RF deflections are worst with 645%. The emittance growth due to beam-gas scattering is insignificant (0.000001%). The beam has an offset in position, angle and energy and it is very likely that it will hit at least one component of the BDS lattice producing damage.

Computer simulations were performed in order to analyse the effect of this offset beam on the BDS elements. A list of components hit by the beam with the corresponding particle deposition was obtained for each case separately and it was found that the spoilers are the most affected. Although the TESLA spoilers are sufficiently thin that no full electro-magnetic shower can develop, the spoilers can be damaged if the local temperature increases beyond an acceptable limit. For a maximum particle deposition per μm^2 of 9000 particles after repeated effects of energy deposition and thermal diffusion, the temperature reached was 1989 K for 22 bunches. The melting temperature for titanium is 1933 K.

In conclusion, in the case of a machine protection failure, the survival of the TESLA spoilers is very difficult to guarantee. It turns out that they can take more than two

bunches but not a whole bunch train if they are hit head-on by an offset beam.

All the analysis described above has been performed with spoilers treated as "hard-edges" in the computer code. A more realistic approach was achieved with Coulomb scattering applied in the simulation program: the incident particles receive a large kick angle and lose energy which brings them on dispersive trajectories. Therefore, the particle distribution at the final doublet was re-analysed and it was found that it was outside the collimation depth.

The next steps and areas for improvement it suggests are clear. An analysis of the spoiler design and material type is expected in the near future. The collimation efficiency is still to be determined and also the exact position of the thick absorbers in the lattice. The latter will help greatly the determination of the collimation depth which was determined initially without including scattering effects. The effect of particle deposition on the iron magnets is not understood yet.

The spoiler study is in many respects far from complete but this important linear collider component is still investigated and it is hoped that a completely satisfactory solution will be found in the near future.

Appendix A

```
// Declaration of class Scattering
#ifndef Scattering_h
#define Scattering_h

#include "BeamDynamics/ParticleTracking/CollimateParticleProcess.h"
#include "NumericalUtils/Utils.h"

class Scattering:public CollimateParticleProcess
{
public :
// Constructor
// Takes the calculated Coulomb scattering angle θ, the width of the scattering
// medium, the priority (the highest priority of the bunch process is 0, followed by
// 1,2...etc), the collimation mode, and the output stream pointer to which to print
// the results.
Scattering(double, double, int, int, std::ostream*);

// Destructor
~Scattering();

// Function which returns the momentum loss by the scattered particles in a
// scattering medium δ= -(p'-p)/p where p is the initial momentum of the
// particles and p' is the final momentum;
```

```
double EnergyLoss();

private:

// Function which applies a position and angle displacement to particles found
// outside the spoilers' collimation aperture and lowers their momentum;
void DoScattering();

// Performs the process for the specified step df;
void DoProcess(double df);

double width;
double delta;
double theta;
double f;
double next_f;
double S;
std::list<size_t>* index;
};
#endif
```

Appendix B

```
//Member function definition for class Scattering
#include <fstream>
#include "Random/RandomNG.h"
#include "Scattering.h"
using namespace std;

// class Scattering

Scattering::Scattering( double th, double wth, int Priority, int Mode, std::ostream*
oss) :CollimateParticleProcess( Priority, Mode, oss), theta(th), width(wth), delta(0.0){}

Scattering::~Scattering(){};

double Scattering::EnergyLoss()
{
        const int n=49;
        static int x[n];
        static double y[n];
        static bool firsttime = true;
        if (firsttime)
        {
            ifstream fromfile ("EnergyLoss.txt");
            for (int i=0; i<50; i++)
```

```
                { fromfile>>x[i]>>y[i]; }
            firsttime = false;
        }
        double RNG = RandomNG::uniform(0.0,1.0);
        for(int j=0; j<50; j++)
        {
            if(( y[j]<RNG )&&( RNG<y[j+1] ))
                {double delta = 0.01* x[j+1];}
        }
        return delta;
}

void Scattering::DoProcess(double df)
{
        f += df;
        if (fequal(f,next_f)){
            DoScattering();
            SetNextS();}
}

void Scattering::DoScattering()
{
        const Aperture *ap = currentComponent->GetAperture();
        PSvectorArray PSscat;
        list<size_t>::iterator ip;

        if (pindex!=0)
            ip =pindex->begin();

        if ("ESPOI"== currentComponent->GetName()|| "XYSPOI"==
```

```
currentComponent->GetName() || "COLX" == currentComponent
->GetName()|| "COLY"== currentComponent->GetName() )
{
   for (PSvectorArray::iterator p = currentBunch->begin(); p!=
   currentBunch->end();p++)
   {
   if(!ap -> PointInside( p->x(),p->y(),s ))
      {
      const double n1 = 0.288; // 1/sqrt(12)
      const double n2 = 0.5; // 1/2
      double z1x = RandomNG::normal(0.0,1.0);
      double z2x = RandomNG::normal(0.0,1.0);
      p->x() += z1x*width*theta*n1 + z2x*width*theta*n2;
      p->xp()+= z2x*theta;
      double z1y = RandomNG::normal(0.0,1.0);
      double z2y = RandomNG::normal(0.0,1.0);
      p->y() += z1y*width*theta*n1 + z2y*width*theta*n2;
      p->yp()+= z2y*theta;
      double deltaN = p->dp();
      double deltaG = EnergyLoss();
      p->dp() = deltaN*( 1-deltaG) - deltaG;
      }
   }
}

   else
      DoCollimation();
}
```

Bibliography

[1] G.Kane, "Supersymmetry", Perseus Publishing, Cambridge, Massachusetts, February 2000.

[2] W.N.Cottingham, D.A.Greenwood, "An Introduction to the Standard Model of Particle Physics", Cambridge University Press, 1998.

[3] R.Brinkmann *et al.*(eds), "The TESLA Technical Design Report", part 3 - Physics at an e^+e^- Linear Collider, DESY 2001-011, ECFA 2001-209 (March 2001).

[4] Stanford Linear Collider, *http* : *//www2.slac.stanford.edu/vvc/experiments/slc.html*, accessed Sept 2003.

[5] W.Decking, "The TESLA Linear Collider", DESY Summer Student Lecture, 16th July 2003, *http* : *//www.desy.de/f/students/lectures*2003/*decking.pdf*, accessed Sept 2003.

[6] A. Hellemans, "Linear Colliders", Europhysics News (2000), Vol. 31, No 6.

[7] S.Chattopadhyay, K.Yokoya, "Challenges in Future Linear Colliders", Jefferson Lab, Newport News, VA 23606, USA and KEK, Tsukuba, Ibaraki 305-0801 Japan.

[8] SLAC Linear Collider, *http* : *//www − sld.slac.stanford.edu/sldwww/slc/SLAC_Aerial.gif*, accessed Sept 2003.

[9] M.Tigner, "A Possible Apparatus for Electron Clashing Experiments", Nuovo Cimento, 37 (1965) 1228.

[10] A.W.Chao, M.Tigner, "Handbook of Accelerator Physics and Engineering", World Scientific (1999).

[11] H.Wiedemann, "Particle Accelerator Physics I", Second Edition, Springer-Verlag, Berlin, Heidelberg, 1993,1999.

[12] N.Walker *et al.*, "An Introduction to the Physics and Technology of e^+e^- Linear Colliders", USPAS, Santa Barbara, June 2003.

[13] The NLC Design Group, "Zeroth-Order Design Report for the Next Linear Collider", LBNL-5424, SLAC-474, UCRL-ID-124161, UC-414 May 1996.

[14] K.Abe *et al.*, "GLC Project - Linear Collider for TeV Physics", GLC Project Report, 2003.

[15] R.W.Assmann *et al.* "A 3 TeV e^+e^- Linear Collider Based on CLIC Technology", Geneva 2000.

[16] T. Raubenheimer *et al.*, "Parameters of the SLAC Next Linear Collider", Stanford Linear Accelerator Center, Stanford University, Stanford, CA, 94309.

[17] Tor Raubenheimer, "JLC/NLC Technology Update", Arlington Linear Collider Workshop, Arlington, Texas, January, 2003.

[18] H.Weise, "The TESLA Test Facility (TTF) Linac - A Status Report", DESY, 22603 Hamburg, Germany.

[19] R.Brinkmann *et al.*(eds), "The TESLA Technical Design Report", part 2 - The Accelerator, DESY 2001-011, ECFA 2001-209 (March 2001).

[20] P.Sievers, M.Höffert, "A Megawatt Electron Positron Conversion Target - A Conceptual Design", Proc. 1 EPAC, Rome 1988.

[21] W.Benecke, "TTF-The Way to TESLA", Deutsches Electronen-Synchrotron DESY, Hamburg, Germany.

[22] T.O.Raubenheimer, F.Zimmermann, "A Fast Beam-Ion Instability in Linear Accelerators and Storage Rings", SLAC-PUB-95-6740 and Phys.Rev. E52 (1995) 5487.

[23] K.Ohmi, "Beam-Photoelectron Interactions in Positron Storage Rings", Phys.Rev. Lett 75:8 (1995) 1526.

[24] K.Ohmi, F.Zimmermann, "Head-Tail Instability Caused by Electron Clouds in Positron Storage Rings", Phys.Rev.Lett 85:18 (2000) 3821.

[25] V.D.Shiltsev, "TESLA Damping Ring Impedances: Preliminary Design Considerations", DESY TESLA-96-02, 1996.

[26] K.Flöttmann, J.Rossbach, "Emittance Damping Considerations for TESLA", DESY 93-023, 1993.

[27] A.Wolski, private communication.

[28] K.Wille, "The Physics of Particle Accelerators", Oxford University Press, 2000.

[29] W.Decking, G.Hoffstaetter, T.Limberg, "Bunch Compressor for the TESLA Linear Collider", DESY, Notkestraße 85, 22603 Hamburg, Germany.

[30] "Basic Properties of Superconducting Cavities", $http://tesla.desy.de/new\_pages/wr\_poster/181001/WR\_cavity\_basics.pdf$, accessed Sept 2003.

[31] C. Reece *et al.*, "Performance Experience with the CEBAF SRF Cavities", Proc. Particle Accelerator Conference and International Conference on High Energy Accelerators, Dallas 1995, p.1512.

[32] H.Padamsee, J.Knobloch, T.Hays, "RF Superconductivity for Accelerators", John Wiley, New York, 1998.

[33] R.Brinkmann *et al.*(edt), "TESLA-CDR", DESY 1997, ECFA 1997.

[34] R.Brinkmann, N.Walker, O.Napoly, J.Payet, "A New Beam Delivery System (BDS) for the TESLA Linear Collider", CEA/saclay, Gif-sut-Yvette, France.

[35] R.Brinkmann, N.Walker, G.Blair, "The TESLA Post-linac Collimation System", DESY TESLA-01-12 (2001).

[36] J.Payet, O.Napoly, "A Proposal for the TESLA High Energy Beam Switchyard", CEA/Saclay, DAPNIA-SEA, 91191 Gif-sur-Yvette CEDEX, 2000.

[37] M.D.Woodley, P.E.Emma, "Measurement and Correction of Cross Plane Coupling in Transport Lines", Proc. 20th Int. Linac Conference, Monteray, CA, Aug. 2000, LINAC2000-MOC19, SLAC-PUB 8581, 2000.

[38] M.Berz, "Introductory Beam Physics", USPAS course.

[39] "CAS CERN Accelerator School", Proceedings, vol.I Gif-sur-Yvette, Paris, 1984.

[40] M.Conte, W.W.MacKay, "An Introduction to the Physics of Particle Accelerators", World Scientific, 1991.

[41] K-J.Kim, "Accelerator Physics and Technologies for Linear Colliders", University of Chicago, Lecture Notes, Winter 2002.

[42] S.Baird, "Accelerator Physics for Pedestrians", lecture notes given to PS accelerator division, CERN.

[43] H.Wiedemann, "Particle Accelerator Physics II", Second Edition, Springer-Verlag, Berlin, Heidelberg, 1993,1999.

[44] E.Wilson, "An Introduction to Particle Accelerators", Oxford University Press, 2001.

[45] S.Humphries, "Principles of Charged Particle Acceleration", John Wiley and Sons, July 1999.

[46] J.Rosenzweig, "Fundamentals of Beam Physics", Oxford University Press Inc., New York, 2003.

[47] B.Stroustrup, "The C++ Programming Language", Addison Wesley Longman, Reading, MA, 1997.

[48] R.Wiener, "An Introduction to Object-Oriented Programming and C++", Addison Wesley Publishing Company, 1988.

[49] L.Ammeraal, "C++ for Programmers", John Wiley and Sons, 1991.

[50] R.Lafore, "Object-Oriented Programming in C++", Sams Publishing, 1999.

[51] A C++ Class Library for Performing Charged Particle Accelerator Simulations, $http://www.desy.de/\sim merlin/$, accessed Sept 2003.

[52] N.Walker, BDS lattice version 8.05, private communication.

[53] H.Grote, F. Christoph Iselin, "Methodical Accelerator Design", version 8.19, User's Reference Manual, Geneva, Switzerland, 1996.

[54] K.L.Brown, F.Rothacker "TRANSPORT - A Computer Program for Designing Charged Particle Beam Transport Systems", SLAC, Stanford, California, 94305.

[55] K.L.Brown, "A First-and Second-Order Matrix Theory for the Design of Beam Transport Systems and Charged Particle Spectrometers", SLAC Report-75, June 1982.

[56] J. Frisch, E.Doyle, K.Skarpaas, "Advanced Collimator Engineering for the NLC", SLAC, Stanford CA, 94025.

[57] D.Walz, A.McFarlane, E.Lewandowski, J.Zabdyr, "Momentum Slits, Collimators and Masks in the SLC", SLAC-PUB-4965, Stanford, CA.

[58] R.Brinkmann, G.Materlik, J.Robach and A.Wagner (eds), "Conceptual Design of a 500 GeV e^+e^- Linear Collider with Integrated X-ray Laser Facility", DESY-97-048 and ECFA-97-182, chapter 3 (1997).

[59] R.Brinkmann *et al.*, "The TESLA Beam Collimation System", DESY TESLA-95-25 (1995).

[60] Periodical Table of Elements, Element Titanium - Ti, "http://environmentalchemistry.com/yogi/periodic/Ti.html" , accessed Sept 2003.

[61] R.Brinkmann, I.I.Degtyarev, A.E.Lokhovitskii, E.A.Merker, I.A.Yazynin, "Beam Collimators", SRC Institute for high Energy Physics, 142284 Protvino, Moscow.

[62] O.Napoly, "Collimation Depth Requirements for the TESLA IR", DESY TESLA-01-18 (2001).

[63] F.Zimmermann, "Lecture Notes for Accelerator Physics and Technologies for Linear Colliders", University of Chicago, Physics 575, 2002.

[64] T.Raubenheimer,"SLC Status and NLC Design and *R&D*", Stanford Linear Accelerator Center, Stanford University, Stanford, California, 94309.

[65] A.Adolphsen *et al.*, "The Next Linear Collider Machine Protection System", Stanford Linear Accelerator Center, Stanford, CA, 94309.

[66] M.C.Ross *et al.*, "Single Pulse Damage in Copper", Proc. 20^{th} Int.Linac Conf., Monteray, CA, August 2000 (LINAC2000-MOA06); SLAC-PUB-8605,2000.

[67] N.Walker - private communication.

[68] A.Novokhatski *et al.*, "Transition Dynamics of the Wakefields of Ultra Short Bunches", TU Darmstadt, TEMF, Schlossgartenstr. 8, D-64289 Darmstadt, Germany.

[69] N.Walker, A.Wolski, "Luminosity Stability Issues for the TESLA Beam Delivery System (BDS)", TESLA 2000-22, October 2000.

[70] K.Balewski, "Review of Feedback Systems", DESY, Hamburg, Germany.

[71] I.Reyzl, "Stabilization of Beam Interaction in the TESLA Linear Collider", DESY, Notkestr.85, 22603 Hamburg, Germany.

[72] R.D.Kohaupt, I.Reyzl, "Fast Feedback Systems for Orbit Correction in the TESLA Linear Collider", DESY, Notkestr.85, 22607 Hamburg, Germany.

[73] R.Lorenz, I.Reyzl, S.Sabah, "Study of Orbit Feedback Systems for the TESLA Linear Collider" TU Berlin, Einsteinufer 17, D - 10587 Berlin, Germany.

[74] J.Frisch, E.Doyle, K.Skarpaas, "Advanced Collimator Systems for the NLC", SLAC, Stanford CA, 94305.

[75] D.Perkins, "Introduction to High Energy Physics", Addison-Wesley Publishing Company, Reading, Massachusetts, 1972.

[76] "PDG booklet", K.Hagiwara *et al.*, Phys.Rev. D66, 010001, July 2002.

[77] G.Blair - private communication.

[78] "Handbook of Chemistry and Physics", 55^{th} Edition, CRC pres, 1974.

[79] J.P.Holman, " Heat Transfer", 8^{th} edition, McGraw-Hill, 1997.

[80] H.A.Bethe, "Moliere's Theory of Multiple Scattering", Laboratory of Nuclear Studies, Cornell University, Ithaca, New York, 1952.

[81] H.S.Snyder, W.T.Scott, "Multiple Scattering of Fast Charged Particles", Brookhaven National Laboratory, Upton, New York, 1949.

[82] W.T.Scott, "Mean-Value Calculations for Projected Multiple Scattering", Brookhaven National Laboratory, Upton, New York and Smith College, Northampton, Massachusetts, 1951.

[83] H.M.Deitel, P.J.Deitel, "C++ How to Program", Prentice Hall, Upper Saddle River, New Jersey 07458, 2001.

[84] E.Segre, "Nuclei and Particles - An Introduction to Nuclear and Subnuclear Physics", W.A.Benjamin, Inc, Reading, Massachusetts, 1977.

[85] B.Rossi, "High-Energy Particles", Prentice-Hall, Inc., 1952.

[86] "The European Physical Journal C", Volume 15, Number 1-4, 2000.